Neural Networks for Accurate, Scalable and General Core Loss Modeling in Magnetic Components

QIUJIE HUANG

THE UNIVERSITY OF SYDNEY

Supervisor: Sinan Li
Associate Supervisor: Jianguo Zhu

A thesis submitted in fulfilment of the requirements for the degree of Doctor of Philosophy

School of Electrical and Computer Engineering
Faculty of Engineering
The University of Sydney
Australia

This research reported in this thesis was supported by the award of a Research Training Program scholarship to the PhD Candidate.

27 February 2026

Statement of Originality

I hereby declare that this submission is my own work and to the best of my knowledge it contains no materials previously published or written by another person, nor material which has been accepted for the award of any other degree or diploma at any university or other institution, except where due acknowledgment has been made in the text.

Any contribution made to the research by others, with whom I have worked at the University of Sydney or elsewhere, is explicitly acknowledged in the thesis.

I also declare that the intellectual content of this thesis is the product of my own work, except to the extent that assistance from others in the project's design and conception or in style, presentation and linguistic expression is acknowledged.

Date: February 2026

Name: Qiujie Huang

Signed: _____

Research Outputs

The thesis may contain some of the research outputs below:

Journal Articles (JA.)

[JA1] **Q. Huang**, Y. Li, J. Zhu and S. Li, "Magnetization Mechanism-Inspired Neural Networks for Core Loss Estimation," in *IEEE Transactions on Power Electronics*, vol. 39, no. 12, pp. 16382-16390, Dec. 2024.

[JA2] **Q. Huang**, Y. Li, Y. Dou, Y. Li, J. Zhu and S. Li, "History-Dependent Prandtl–Ishlinskii Neural Network for Quasi-Static Core Loss Prediction Under Arbitrary Excitation Waveforms," in *IEEE Transactions on Power Electronics*, vol. 40, no. 7, pp. 9625-9637, July 2025.

[JA3] M. Chen et al., "MagNet Challenge for Data-Driven Power Magnetics Modeling," in *IEEE Open Journal of Power Electronics*, vol. 6, pp. 883-898, 2025.

[JA4] **Q. Huang** et al., "Neural-Enhanced Physics: A New Paradigm for Accurate and Dimension-Aware Magnetic Core Loss Modeling," in *IEEE Transactions on Power Electronics*, doi: 10.1109/TPEL.2026.3659820.

Conference Articles (CA.)

[CA1] J. Li, S. Li, W. Li and **Q. Huang**, "A Soft-Switched Microinverter with Continuous-Conduction-Mode Grid-Side Inductor Current," *2023 IEEE Energy Conversion Congress and Exposition (ECCE)*, Nashville, TN, USA, 2023, pp. 1052-1058.

[CA2] Q. Huang, S. Li, Y. Li and J. Zhu, "Magnetization Mechanism-Inspired Neural Network for Core Loss Estimation," *2024 IEEE Energy Conversion Congress and Exposition (ECCE)*, Phoenix, AZ, USA, 2024, pp. 7137-7144.

Awards and Recognitions (A.)

[A1] "Design of high-frequency, high-efficiency and high-density power converter", entry to the final of the 3rd Huawei Power Electronics Innovation Contest for University Students.

[A2] *Excellent Innovation Award, 1st Place*, IEEE PELS-Google-Enphase 2023 MagNet Challenge, organized by IEEE PELS TC10 - Design Methodologies, for the work titled "Magnetization Mechanism-Inspired Neural Networks."

[A3] *Best Software Engineering Award*, IEEE PELS-Google-Enphase 2023 MagNet Challenge, organized by IEEE PELS TC10 - Design Methodologies, for the work titled "Magnetization Mechanism-Inspired Neural Networks."

Acknowledgements

This research could not have been accomplished without the significant assistance, support, and advice from my collaborators, supervisors, colleagues, friends, and family. While it is not possible to name everyone who has played a role in this endeavor, I wish to express my sincere appreciation to those who have most significantly influenced the progression of this work.

First and foremost, I want to give my deepest thanks to my supervisor, **Dr. Sinan Li**. It was his passion and sense of responsibility that first attracted me to start this PhD journey. Throughout these years, his creative way of thinking opened up new possibilities for me, and his careful and steady guidance helped me find my way through the research. His insightful feedback always pushed me to improve my work. Dr. Li's enthusiasm for research and his high standards for academic work constantly inspired me to keep going, especially during difficult times. I am deeply grateful for his mentorship, which has been instrumental in my growth as a independent researcher.

I am also very grateful to my co-supervisor, **Prof. Jianguo Zhu**, for his insightful comments and the wealth of experience he shared, which were invaluable in shaping the direction of this research. My heartfelt thanks also go to **Dr. Yang Li** and **Dr. Yu Dou**. They have been my mentors and partners-in-research, patiently guiding me through the intricacies of materials science and modeling. Their constant encouragement, timely assistance, and crucial technical support were indispensable. I will always be grateful for their camaraderie; they were truly allies on the front lines of research, and their help was instrumental to my progress.

I would like to extend my gratitude to all the members of our Power Electronics Research Group, especially **Dr. Wanrong Li**, **Dr. Lei Wang**, **Ms. Shuang Jiao**, **Mr. Jinghang Li**, **Mr. Yuhan Zhang**, **Mr. Xuanting Shen**. I am so thankful for their constant encouragement and help. They patiently answered my countless questions, helped me troubleshoot research problems, and offered clarity when I felt lost. More than just colleagues, they have been like brothers to me, providing a constant source of strength and support. Their camaraderie made the challenging moments of this PhD journey much more manageable, and for that, I am profoundly grateful. I am also incredibly thankful for my dear friends who made Sydney feel like a second home. To **Mr. Xiaoming Song**, **Mr. Chengjian Song**, **Mr. Chenghang Yuan**, **Mr. Songhui Bi**, **Mr. Senyao Wang**, **Mr. Hangdong An**, **Mr. Fujian Li**, **Mr. Xiaodong Zhao**, **Mr. Siyuan Guo**, **Mr. Yihao Dong**, **Mr. Yuzhi Zhong**, **Mr. Xiao Liu**, **Mr. Cheng**

Peng, **Mr. Huan Li**, **Mr. Yixiong Feng**, **Mr. Yachao Zhu**, **Mr. Bingkuan Wan**, **Ms. Yunwan Liu**, **Ms. Letong Li**, **Ms. Mingxuan Chen**, **Ms. Yiyan Zhang**, **Ms. Xiaoheng Zhou**, and so many others, thank you for making my time here so vibrant and memorable, and for filling my life outside the lab with joy, laughter, and unwavering support. I will cherish these memories forever.

This research was supported by funding from University of Sydney International Stipend Scholarship (USYDIS), Postgraduate Research Support Scheme (PRSS) provided by the Faculty of Engineering, HDR Education Support Scheme from the School of Electrical and Computer Engineering. I am grateful for this financial support, which made this study possible.

Finally, and most importantly, I reserve my deepest love and gratitude for my family. To my beloved parents, your unconditional love, unwavering belief in me, and endless encouragement have been my bedrock throughout this long journey. Your sacrifices and support, even from thousands of miles away, gave me the strength to persevere through the most challenging times. This dissertation is as much a testament to your love as it is to my work.

Author Attribution Statement

This thesis is submitted in fulfilment of the requirements for the degree of Doctor of Philosophy at the University of Sydney.

To the best of my knowledge, the work presented here is my own, except where appropriate acknowledgment is made. This includes all text, figures, models, and analysis.

Some chapters are based on co-authored publications or collaborative work. In each case, the contribution of all authors is clearly indicated, and I confirm that I was the primary contributor to the research, coding, data analysis, and writing. Specifically:

- Chapter 3 is based on: "Magnetization Mechanism-Inspired Neural Networks for Core Loss Estimation."

  My contribution: Designed the core modeling strategy, implemented the Magnetization Mechanism-Inspired Neural Network (MMINN) architecture, conducted simulations, and drafted the manuscript.
- Chapter 4 is based on: "History-Dependent Prandtl–Ishlinskii Neural Network for Quasi-Static Core Loss Prediction Under Arbitrary Excitation Waveforms."

  My contribution: Developed the History-Dependent Prandtl–Ishlinskii Neural Network (HDPI-NN), implemented it in Python, performed evaluations, and prepared the manuscript draft.
- Chapter 5 is based on: "Neural-Enhanced Physics: A New Paradigm for Accurate and Dimension-Aware Magnetic Core Loss Modeling"

  My contribution: Led the Neural-Enhanced Dynamic Circuit Model (NE-DCM) development and integration, performed data processing and validation, and wrote the manuscript.

All other chapters and content are solely my own work and have not been submitted for any other degree or award.

Name: Qiujie Huang Signature: _____ Date: February 2026

As the supervisor for the candidature upon which this thesis is based, I can confirm that the authorship attribution statements above are correct.

Name: Sinan Li Signature: _____ Date: February 2026

Use of Artificial Intelligence Statement

During the preparation of this thesis, the author used ChatGPT and Gemini solely for text enhancement (minimal copyediting), including limited refinement of grammar, spelling, punctuation, sentence structure, and language clarity in draft chapters. No generative AI outputs were accepted as substantive scholarly content, analysis, data interpretation, argument development, or original research findings. All intellectual content remains the author's own work.

Where text was modified following AI-assisted suggestions, all changes were reviewed by the author for accuracy, potential bias, appropriateness of academic tone, and alignment with disciplinary conventions before inclusion in the thesis. The author confirms that AI use remained within University parameters for responsible use (editorial-level assistance only) and that no confidential, personal, or copyrighted third-party data were uploaded beyond what is permitted.

The author takes full responsibility for the submitted thesis and affirms that its content is their own, with all AI use conducted strictly in accordance with the University of Sydney's guidelines.

Abstract

Accurate and scalable prediction of core losses in magnetic components is a paramount yet challenging task in modern power electronics design. While traditional physics-based models (e.g., Jiles–Atherton, dynamic circuit formulations) inherently offer geometric scalability and interpretability, they often struggle to maintain accuracy when confronted with complex waveforms. Conversely, purely data-driven neural networks can achieve impressive accuracy within their training domain, but they demand large datasets and require extensive retraining for each new core size, severely limiting their practical scalability. Bridging this fundamental trade-off between accuracy, generality, scalability, and data efficiency is therefore pivotal for the advancement of automated magnetic-component design.

This thesis systematically investigates hybrid strategies that synergistically fuse neural networks with physical insights, by progressively decomposing this grand challenge into a series of interconnected sub-problems of increasing complexity. For each sub-challenge, a novel, complementary hybrid modeling approach is proposed and rigorously validated in its specific application setting:

1. **Addressing Core Loss Prediction for Steady-State, High-Frequency, Symmetric Waveforms:**

   As an initial step, the Magnetization-Mechanism-Inspired Neural Network (MMINN) is introduced. MMINN decomposes core loss into hysteresis and dynamic components, assigning a compact neural sub-network to each. This method targets routine factory tests where ferrite cores are driven by continuous, symmetric high-frequency waveforms. Validation on N87 and N49 ferrite data from the MagNet database demonstrates that MMINN accurately predicts the magnetic field response and associated steady-state core loss with a minimal memory footprint and minimal training data.

2. **Extending Generality to Transient, Quasi-Static, Arbitrary Waveforms:**

   Building upon this foundation, to tackle the complexities of transient and quasi-static conditions involving arbitrary waveforms, including DC bias and minor loops, the History-Dependent Prandtl-Ishlinskii Neural Network (HDPI-NN) is developed. HDPI-NN extends the classical Prandtl-Ishlinskii operator by integrating neural pathways to capture reversible magnetization and critical memory effects. Experimental validation on silicon-steel B35A270 and ferrite N87 under user-defined low-rate

excitations shows that HDPI-NN significantly improves the prediction accuracy of time-varying magnetic fields and associated core losses, demonstrating superior generalization to arbitrary excitations compared to earlier physics-guided neural networks.

3. **Achieving Scalable Prediction Across Different Core Sizes for Transient, High-Frequency, Arbitrary, Asymmetric Waveforms:**
   Culminating in the ultimate objective of scalable core loss prediction across diverse core dimensions under transient, high-frequency, arbitrary, and asymmetric waveforms, the Neural-Enhanced Dynamic Circuit Model (NE-DCM) is proposed. NE-DCM seamlessly embeds the HDPI-NN material block within a physics-based, mesh-based dynamic circuit solver. This principled decomposition allows the solver to handle scalable electromagnetic dynamics and geometric effects, while the neural block accurately captures the complex non-linear material hysteresis. Extensive validation on three TDK N87 toroidal cores of significantly different cross-sections, driven by arbitrary excitations up to hundreds of kilohertz, confirms NE-DCM's superior accuracy, generality, scalability, and data-efficiency in predicting terminal current waveforms and core losses, requiring only minimal calibration for each new core.

In summary, this thesis presents a systematic and progressive hybrid modeling strategy, with each step addressing a specific, increasingly complex challenge in core loss prediction. Collectively, these strategies demonstrate that the synergistic combination of physical models with neural networks can lead to accurate, general, scalable, and data-efficient solutions, forming a robust and extensible foundation for next-generation magnetic component design tools. Moreover, this research actively contributes to the broader scientific community by developing and making available open-source tools and datasets, thereby promoting further research and practical adoption of these models.

Contents

List of Figures

List of Tables

List of Abbreviations

MMINN:	Magnetization Mechanism-Inspired Neural Network
HDPI-NN:	History-Dependent Prandtl-Ishlinskii Neural Network
NE-DCM:	Neural-Enhanced Dynamic Circuit Model
NEP:	Neural-Enhanced Physics
B-H:	Magnetic Flux Density (B) – Magnetic Field Strength (H)
GDCM:	Generalized Dynamic Circuit Model
iGSE:	Improved Generalized Steinmetz Equation
J-A:	Jiles-Atherton (Model)
PI:	Prandtl-Ishlinskii (Model/Operator)
FNN:	Feedforward Neural Network
RNN:	Recurrent Neural Network
CNN:	Convolutional Neural Network
LSTM:	Long Short-Term Memory
PINN:	Physics-Informed Neural Network
DAB:	Dual Active Bridge
PWM:	Pulse-Width Modulation
DC:	Direct Current
AC:	Alternating Current
MAPE:	Mean Absolute Percentile Error
MSE:	Mean Squared Error
NRMSE:	Normalized Root Mean Squared Error
SST:	Single Sheet Tester
DUT:	Device Under Test
IEEE:	Institute of Electrical and Electronics Engineers
MagNet:	Open-source magnetic core loss database

CHAPTER 1

Introduction: Towards Accurate, Scalable, and General Core Loss Modeling for Power Electronics

---

The rapid advancement of power electronic systems is a key enabler for numerous modern technologies, including renewable energy integration, electric mobility, and efficient power delivery. Achieving higher power density and efficiency is a constant driving force in this field. Magnetic components, such such as inductors and transformers, are indispensable building blocks in nearly all power converters, performing vital functions like energy storage, transfer, filtering, and isolation. Figure 1.1 illustrates a simplified schematic of a Dual Active Bridge (DAB) converter, a representative topology in high-power density applications, highlighting key magnetic components like the input filter inductor (L_f) and the high-frequency transformer (T_r, including its magnetizing inductance L_m). The performance, size, and cost of these magnetic components often represent significant limitations in the overall power converter design.

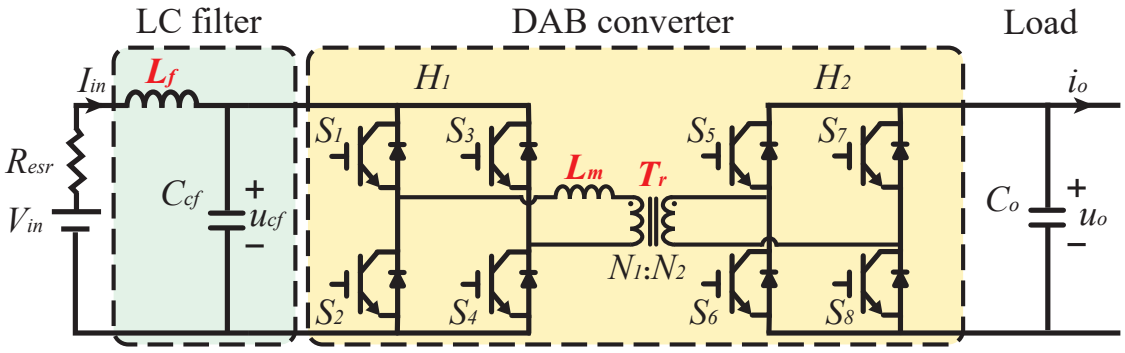

FIGURE 1.1: Simplified schematic of a Dual Active Bridge (DAB) converter, highlighting key magnetic components (L_f, T_r).

The industrial significance of these components is underscored by the substantial and expanding market for magnetic materials. As illustrated in Figure 1.2, the global magnetic materials market, including the crucial segment of soft magnetic materials used extensively in power electronics, is projected to reach $48.2 billion by 2030. This large and growing market highlights the economic imperative and industrial relevance of research focused on improving the design and optimization of magnetic components.

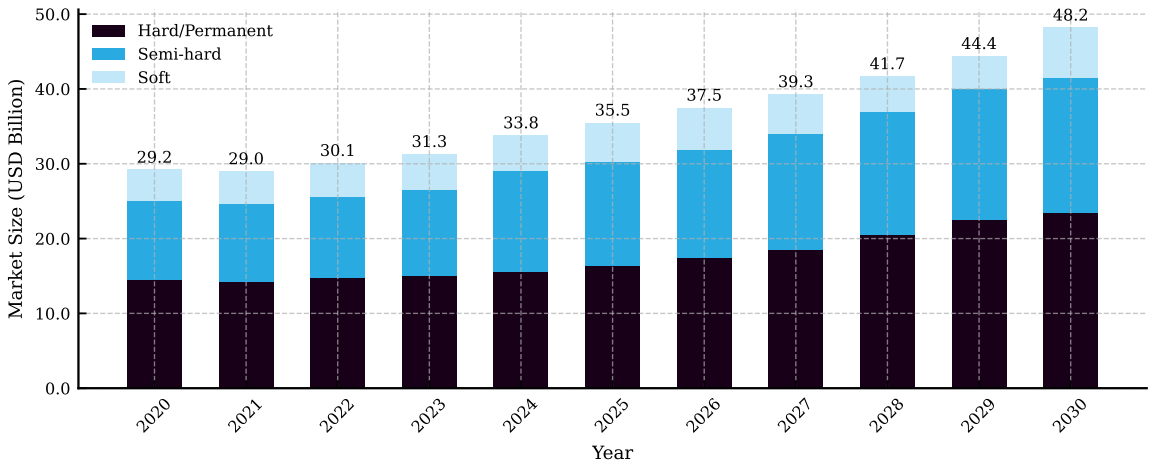

FIGURE 1.2: Magnetic Materials Market Size by Type, 2020-2030 (USD Billion) [1].

1.1 The Grand Challenge: Accurate, Scalable, and General Core Loss Modeling

A primary obstacle to improving the performance and reducing the size of the crucial magnetic components discussed above is accurately predicting and minimizing core loss – the energy dissipated within the magnetic material under time-varying magnetic fields. Core loss is a major contributor to overall component losses, impacting efficiency, thermal management, and ultimately limiting power density.

Accurately modeling core loss is inherently challenging due to the complex, non-linear behavior of magnetic materials, which arises from intricate microscopic domain dynamics (domain wall motion, rotation, interactions with microstructure) and macroscopic dynamic effects (eddy currents, anomalous losses). Furthermore, magnetic components in modern power electronics are often subjected to a wide variety of complex excitation waveforms that deviate significantly from simple sinusoids. These include waveforms with high-order harmonics arising from pulse-width modulation (PWM), transient conditions during startup or load changes, and the presence of DC bias. Figure 1.3 visually demonstrates examples of these complex field strength excitation waveforms and the resulting intricate, non-linear, and history-dependent $\mathbf{B}$–$\mathbf{H}$ loops exhibited by magnetic materials. As shown, these complex

waveforms, such as those with superimposed harmonics (Figure 1.3b) or a significant DC bias (Figure 1.3c), introduce phenomena like distorted magnetic field responses and work point shifts. Moreover, transient operation and irregular control signals frequently result in complex minor loops (Figure 1.3d), which are highly dependent on the material's magnetic history. These behaviors, arising from the underlying domain dynamics and material memory, pose significant challenges for accurate modeling across diverse operating conditions and excitation types.

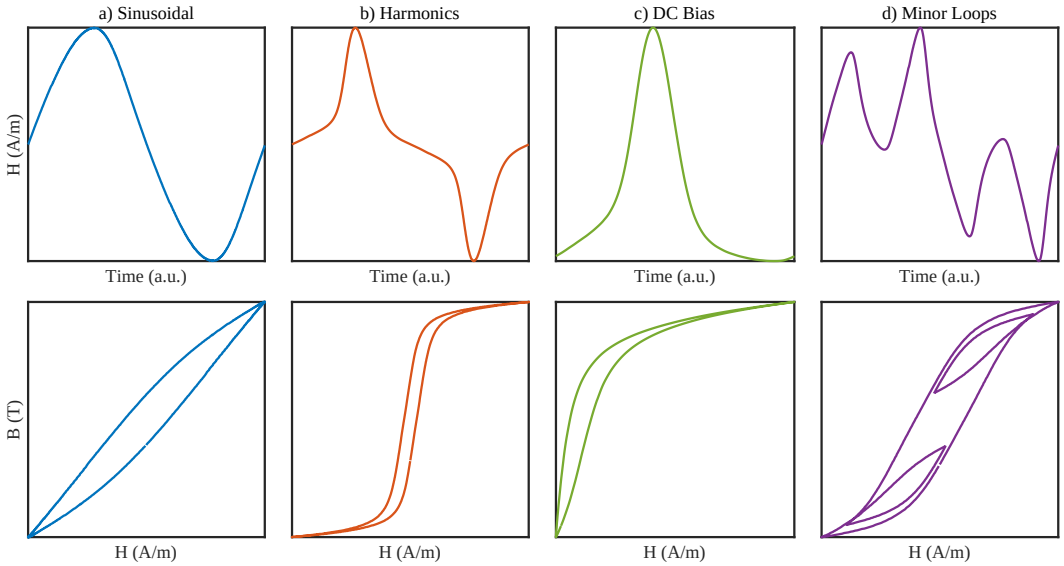

FIGURE 1.3: Examples of complex magnetic excitation waveforms (top row) and their corresponding $\mathbf{B}$–$\mathbf{H}$ loops (bottom row), illustrating the challenges of modeling non-linear and history-dependent behavior under diverse operating conditions (e.g., a) sinusoidal, b) harmonics, c) DC bias, d) minor loops).

To effectively address this complex problem within the context of power electronic design, a core loss model must satisfy three essential requirements:

- **Accuracy:** The model must precisely predict the magnetic field response and resulting core loss under the wide range of complex and arbitrary excitation waveforms encountered in power electronic circuits.
- **Scalability:** The model must be capable of accurately predicting core loss for components of different physical dimensions using the same material, ideally without requiring extensive re-characterization or retraining for each new component size.

- **Generality:** The model should maintain high accuracy across diverse operating conditions (frequency, temperature, excitation waveform shapes) and potentially different magnetic materials, demonstrating broad applicability.

Achieving these three requirements simultaneously is profoundly challenging, and existing modeling approaches face significant limitations in this regard.

1.2 Limitations of Existing Models: The Inherent Trade-Off

As discussed in Section 1.1, achieving accurate, scalable, and generalizable core loss modeling is essential for modern power electronics design. However, existing modeling approaches face significant limitations in simultaneously meeting these requirements, often exhibiting inherent trade-offs. Existing core loss modeling approaches broadly fall into two main paradigms: Model-Driven Models and Data-Driven Models.

Model-Driven Models, including empirical methods [2]–[10], analytical methods [11]–[22] and traditional physics-based [12], [13], [23]–[33], rely on pre-defined model structures and physical principles. Despite their interpretability and potential scalability, these models often rely on simplified magnetization assumptions, limiting their ability to generalize across arbitrary, nonlinear, and history-dependent excitations [24], [25], [34].

Data-Driven Models, primarily utilizing general-purpose neural networks [35]–[44], excel at fitting complex relationships directly from large experimental datasets. They can achieve high accuracy within their training domain. However, they are typically data-hungry, requiring extensive data spanning various conditions and geometries. Crucially, they often lack explicit awareness of component dimensions and struggle to generalize or scale predictions effectively to new component sizes without substantial, costly retraining [38], [45].

To provide a clear and intuitive visualization of the fundamental performance trade-offs inherent in existing core loss modeling paradigms, Figure 1.4 visually summarizes the performance of two typical subtypes. It should be noted that the performance levels (scale 1-5) depicted in this radar chart are qualitative and indicative, based on the comprehensive literature

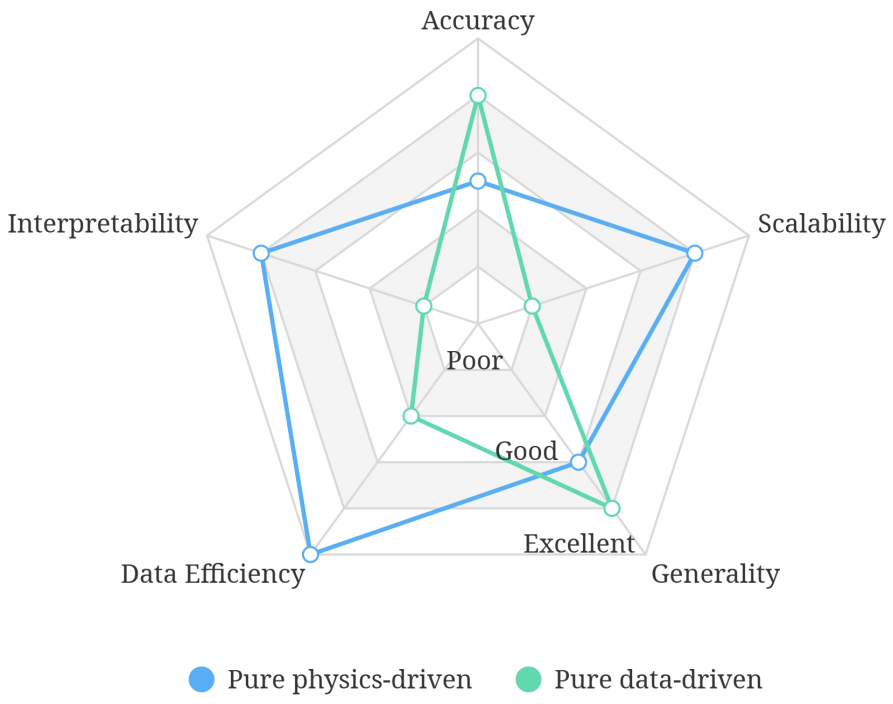

FIGURE 1.4: Performance trade-offs of Model-Driven and purely Data-Driven core loss modeling paradigms across five key aspects.

Note: The levels presented in this chart are qualitative estimates derived from a synthesis of existing literature. They are intended to visualize the relative strengths and weaknesses of each paradigm rather than representing absolute experimental metrics.

review presented in Chapter 2. These levels serve to highlight the relative trade-offs between pure physics-driven models and pure data-driven models, concerning accuracy, scalability, generality, data efficiency, and interpretability. Pure physics-driven models, representing approaches primarily based on fundamental physical principles (like some Physics-Based Hysteresis or Dynamic models), generally score higher on aspects like scalability (due to their geometric foundation) and interpretability. Conversely, pure data-driven models, relying solely on learning from data, can achieve high accuracy (within the domain of trained data) and flexibility. However, as illustrated, these two fundamental approaches exhibit contrasting weaknesses: pure physics-driven models often fall short in accuracy and generality when faced with complex and arbitrary excitation waveforms (due to simplified physics or parameter identification challenges), while pure data-driven models perform poorly

in scalability (requiring retraining for new geometries) and data efficiency (demanding large datasets). It is important to note that this figure focuses on these two extremes to highlight the core trade-off and does not explicitly include hybrid approaches, which attempt to find a balance but also face their own limitations. This inherent trade-off between relying primarily on physics versus relying primarily on data prevents either fundamental paradigm from fully meeting all essential requirements simultaneously. Bridging the gap imposed by these conflicting demands represents a key challenge in the field that is not adequately addressed by current methods. A detailed analysis of the strengths and limitations of various existing core loss modeling approaches, including a discussion of existing hybrid attempts, is presented in Chapter 2.

1.3 Research Objectives: Decomposing the Grand Challenge

Based on the challenges and limitations identified in Section 1.2, the overarching objective of this thesis is to develop a novel and effective core loss modeling framework that simultaneously achieves high accuracy, robust scalability, and broad generality, while maintaining data efficiency. To systematically address this multifaceted grand challenge, the research is structured around the following key objectives:

1. **To Develop a Data-Efficient Modeling Strategy for Common Operating Conditions:** The first objective is to establish the fundamental viability of physics-guided neural network architectures by creating a model that accurately predicts core loss for steady-state, symmetric excitations with significantly reduced data and computational requirements compared to purely data-driven approaches.
2. **To Formulate a High-Fidelity Material Model for Arbitrary Quasi-Static Excitations:** The second objective is to overcome the limitations of traditional hysteresis models by developing a neural network-based material model capable of accurately capturing complex, history-dependent magnetization behavior under arbitrary quasi-static conditions, including DC bias and minor loops.

3. **To Construct a Comprehensive, Scalable, and Generalizable Framework for Component-Level Prediction:** The ultimate objective is to integrate the high-fidelity material model into a scalable, physics-based dynamic solver. This framework must be capable of accurately predicting core loss for components of varying physical dimensions under arbitrary high-frequency excitations, thereby resolving the core accuracy-scalability trade-off.

1.4 Proposed Approach: A Multi-Strategy Exploration of Hybrid Physics-Neural Network Models

To achieve the comprehensive research objective outlined in Section 1.3, this thesis adopts an approach centered on exploring and developing complementary hybrid modeling strategies that fuse neural networks with physical insights at different levels. This research investigates how different hybrid architectures can effectively contribute to the ultimate goal of an accurate, scalable, general, and data-efficient model by tackling specific aspects of the core loss modeling challenge in a progressive manner. This exploration leads to the development and validation of three distinct yet interconnected hybrid models, each representing a unique strategy for combining physics and neural networks to tackle specific aspects of the core loss modeling challenge:

1. **Initial Step - The Magnetization Mechanism-Inspired Neural Network (MMINN):** To address the first objective, we introduce the MMINN. This model explores a mechanism-inspired hybrid structure where neural networks are designed to directly represent separated physical components of core loss (hysteresis and dynamics). It serves as an initial proof-of-concept for leveraging physical intuition to enhance data efficiency.
2. **Next Step - The History-Dependent Prandtl-Ishlinskii Neural Network (HDPI-NN):**
   To fulfill the second objective, we develop the HDPI-NN. This high-fidelity model is deeply informed by physical principles governing hysteresis, integrating concepts of

reversible magnetization and memory effects within a generalized operator framework learned by a neural network. It provides the crucial, accurate material-level building block for the final framework.

3. **Final Step - The Neural-Enhanced Physics (NEP) Paradigm and the NE-DCM:** To achieve the ultimate objective, this thesis culminates in the proposal of NEP paradigm. This paradigm is implemented through the Neural-Enhanced Dynamic Circuit Model (NE-DCM), which embeds the high-fidelity HDPI-NN material model within a scalable, physics-based dynamic solver. This final integrated framework is designed to explicitly resolve the accuracy-scalability trade-off, representing the comprehensive solution to the grand challenge.

Each of these models is developed and validated in its specific application setting to demonstrate its effectiveness in addressing particular aspects of the core loss modeling challenge and to highlight its advantages over existing methods, thereby contributing to the overall objective of developing a comprehensive core loss modeling approach.

1.5 Key Contributions

This thesis makes the following key contributions to the field of magnetic core loss modeling, directly addressing the research objective through the developed hybrid strategies and their validation:

1. **Development and Validation of the MMINN:** A novel hybrid model demonstrating effective core loss estimation for steady-state, high-frequency, symmetric excitations with modest data and memory requirements, representing an early exploration into mechanism-inspired neural structures and their potential benefits for data efficiency.
2. **Development and Validation of the HDPI-NN:** A high-fidelity physics-informed neural network capable of accurately modeling the complex, history-dependent magnetic material behavior under transient, quasi-static, and arbitrary excitation waveforms (including DC bias and minor loops) using limited data, providing

a crucial component for achieving high accuracy and generality under complex excitations.

3. **Proposal and Validation of the NEP Paradigm and the NE-DCM:** A novel integrated framework that successfully combines a scalable physics solver with a high-fidelity neural material model to achieve accurate core loss prediction for transient, high-frequency, arbitrary, and asymmetric waveforms across components of significantly different dimensions, requiring only minimal dimension-specific calibration. The portability of the workflow was successfully demonstrated across two distinct ferrite materials (TDK N87 and T65), proving its general applicability.
4. **Development of Advanced Visualization and Accessibility Tools for Research Dissemination and Practical Adoption:** Recognizing the critical importance of translating complex models into practical and accessible solutions, this thesis develops scalable and interactive visualization tools. These tools are not merely supplementary; they are a significant contribution designed to enhance the interpretability, facilitate the validation, and promote the wider adoption of our proposed models. By providing intuitive interfaces for demonstrating model performance and insights, these tools serve as a vital bridge between theoretical research and practical engineering application, significantly improving the accessibility and impact of this work for the broader research and industrial community. While currently primarily implemented and demonstrated with the MMINN model, its architecture is designed for future extension to incorporate other models developed in this thesis, ensuring a comprehensive platform for model exploration and verification.

1.6 Research Framework and Technical Routes

To provide a cohesive overview of the research journey and illustrate the logical progression between the various modeling strategies developed in this thesis, a comprehensive research framework is presented in Figure 1.5. This diagram clarifies the interrelationships among the core chapters, mapping the technical route from the initial investigation of mechanism-inspired structures (MMINN) to the high-fidelity material modeling (HDPI-NN), and finally

to the integrated system-level solution (NE-DCM). By visualizing the synergy between these progressive stages, the diagram serves as a roadmap to help the reader navigate the transition from material-level physics to scalable component-level design optimization.

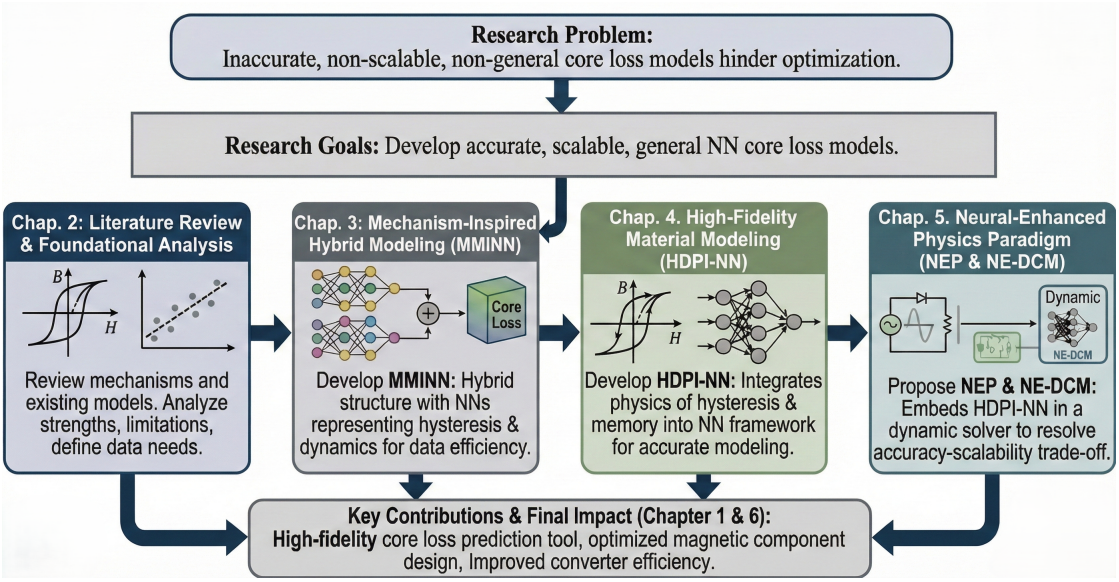

FIGURE 1.5: Research framework and technical routes, illustrating the interrelationships between the developed models and the progressive decomposition strategy adopted in this thesis.

1.7 Thesis Structure

The remainder of this thesis is organized to present the research journey, developed models, and key findings in a logical and comprehensive manner.

- Chapter 2 provides a comprehensive literature review, detailing the fundamental magnetization mechanisms and core loss generation, and critically analyzing existing modeling approaches, including empirical, physics-based, and data-driven methods, highlighting their strengths and limitations in meeting the requirements of accuracy, scalability, and generality.
- Chapter 3 details the development, implementation, and experimental validation of the MMINN, focusing on its mechanism-inspired architecture and application in steady-state, high-frequency scenarios.

- Chapter 4 presents the HDPI-NN, describing its architecture, training methodology, and experimental validation for modeling transient, quasi-static, and arbitrary material behavior.
- Chapter 5 introduces the NEP paradigm and its implementation in the NE-DCM, explaining the integrated architecture, data-efficient modeling workflow, and comprehensive experimental validation for accurate and scalable prediction across dimensions and arbitrary high-frequency excitations.
- Chapter 6 provides a detailed discussion and analysis of the results obtained from the three models, comparing their performance, highlighting their complementary nature, and synthesizing the advantages of the proposed hybrid strategies in addressing the core loss modeling challenges.
- Chapter 7 concludes the thesis by summarizing the key findings and contributions, discussing the limitations of the current work, and outlining directions for future research.

CHAPTER 2

Literature Review and Background

This chapter provides a comprehensive review of the fundamental physical mechanisms underlying core loss in soft magnetic materials and surveys the state-of-the-art in core loss modeling techniques. It critically analyzes the strengths and limitations of existing approaches in meeting the requirements of accuracy, scalability, and generality under diverse operating conditions and across varying component dimensions, thereby establishing the context and motivation for the hybrid modeling strategies explored in this thesis.

2.1 Magnetization Mechanisms and Core Loss

Understanding core loss in soft magnetic materials requires delving into the physical processes that occur when these materials are subjected to time-varying magnetic fields. These processes involve the complex dynamics of magnetic domains and their interaction with induced electromagnetic phenomena. To analyze and model core loss effectively, it is commonly decomposed into distinct physical components. The most widely accepted theoretical framework for this decomposition is Bertotti's Loss Separation Theory [46], [47].

Bertotti's theory posits that the total power loss (P_{total}) per unit volume in a soft magnetic material can be separated into three main components, each arising from different physical mechanisms: a static hysteresis loss (P_{hyst}), a classical eddy current loss (P_{eddy}), and an anomalous loss (P_{anom}). Mathematically, this is often expressed as:

$$P_{total} = P_{hyst} + P_{eddy} + P_{anom}. \tag{2.1}$$

Each component arises from different physical phenomena and exhibits distinct dependencies on frequency, flux density, and material properties [12], [24], [46]–[48]. The static hysteresis loss (P_{hyst}) represents the energy dissipated during irreversible magnetic processes, primarily associated with the movement of domain walls hindered by pinning sites. The classical eddy current loss (P_{eddy}) results from macroscopic, global eddy currents induced by the time-varying magnetic flux according to Faraday's Law. The anomalous loss (P_{anom}) is a

dynamic component attributed to microscopic effects, particularly localized eddy currents circulating around moving domain walls and other non-uniform magnetization processes. The losses caused by both classical eddy currents and anomalous effects are collectively referred to as dynamic losses.

Figure 2.1 visually illustrates some of the fundamental mechanisms contributing to these loss components. The left side depicts a domain wall interacting with pinning sites under an applied field, a process central to hysteresis. The right side highlights the generation of both macroscopic classical eddy currents and localized anomalous eddy currents in the presence of a moving domain wall under an applied field, demonstrating the origins of dynamic losses. Understanding these individual contributions is key to developing accurate models. The following subsections detail the physical origins of each of Bertotti's three loss components.

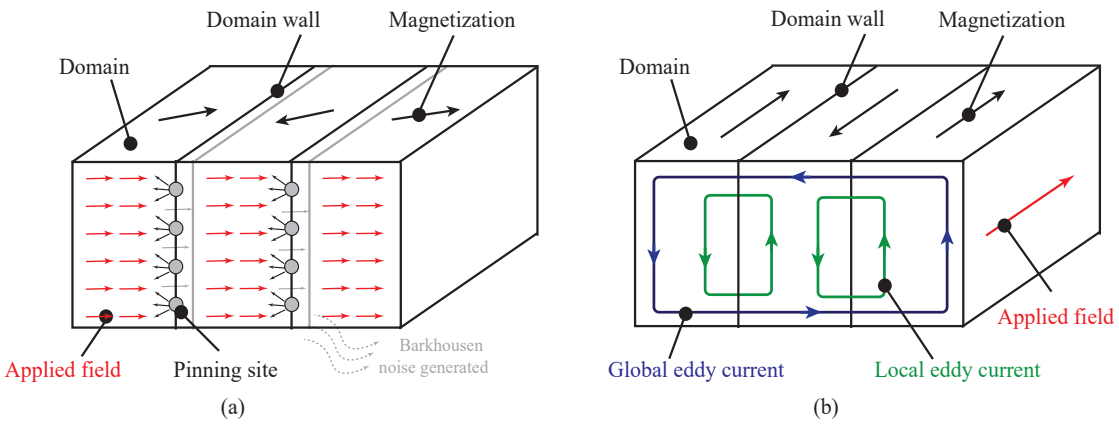

FIGURE 2.1: Illustration of fundamental magnetic mechanisms contributing to core loss, based on Bertotti's Loss Separation Theory: (a) hysteresis loss, and (b) eddy current losses.

2.1.1 Hysteresis Loss

The hysteresis loss (P_{hyst}), identified as the static component in Bertotti's theory, arises from the irreversible nature of the magnetization process in soft magnetic materials. This irreversibility is governed by microscopic magnetic domain processes that dissipate energy during a magnetization cycle.

The foundational understanding of magnetization in ferromagnetic materials stems from the magnetic domain hypothesis, first proposed by Weiss in 1906 [49], [50]. Weiss postulated that ferromagnetic materials are composed of spontaneously magnetized regions called magnetic domains, even in the absence of an external field. The direction of magnetization within these domains is determined by factors such as crystal anisotropy and internal stresses, leading to preferred "easy" axes of magnetization. These domains are separated by domain walls. While often conceptually viewed as sharp boundaries, it is a narrow and finite region where the direction of magnetization gradually rotates from the orientation of one domain to that of an adjacent one. Figure 2.2 provides a schematic illustration of a domain wall, showing the continuous rotation of magnetization vectors across this transition zone between two adjacent domains. The structure and width of a domain wall are determined by a balance between exchange energy (favoring parallel alignment) and magnetic anisotropy energy (favoring alignment along easy axes). The physical existence of these domains and domain walls was later experimentally verified, notably by H.J. Williams and others in 1949 using techniques like the Bitter pattern method [51]. With this experimental confirmation, domain theory became the cornerstone for explaining macroscopic magnetic phenomena and characterizing the magnetization properties of materials.

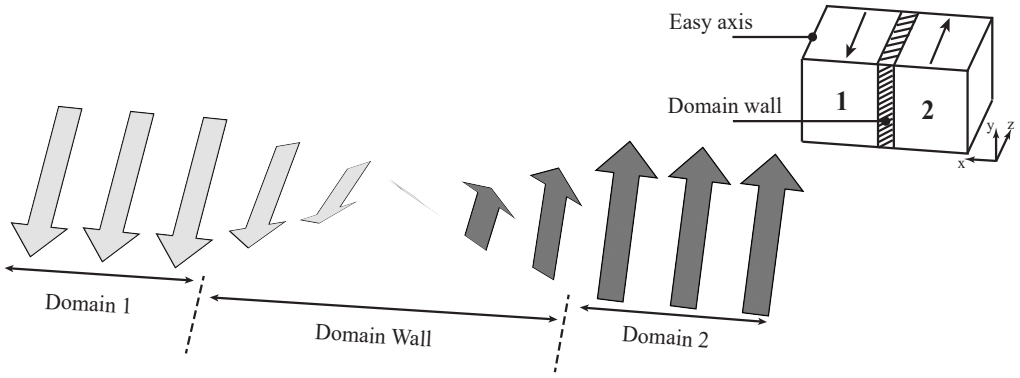

FIGURE 2.2: Schematic illustration of a magnetic domain wall.

When an external magnetic field is applied to a soft magnetic material, the macroscopic magnetization changes through the rearrangement of these magnetic domains. This rearrangement

primarily involves two processes: domain wall motion and domain rotation. The magnetization process can be roughly divided into three stages based on the applied magnetic field strength, as illustrated in Figure 2.3.

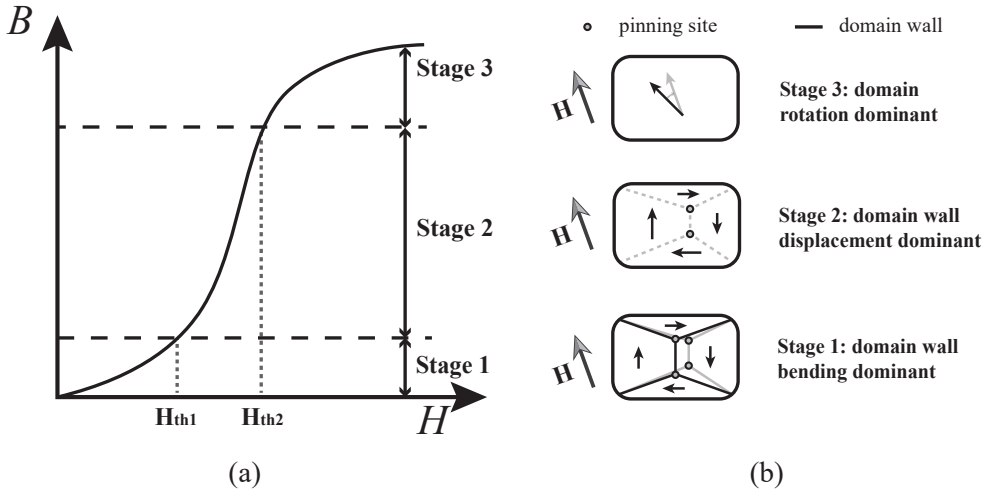

FIGURE 2.3: Magnetization process: (a) **B–H** normal magnetization curve of soft magnetic materials (b) Cubic soft magnetic material magnetization schematic.

In Stage 1, at very low field strengths ($H \leq H_{th_1}$), magnetization changes are dominated by reversible domain wall bending. Domain walls slightly deform or "bow out" under the influence of the applied field. This stage is largely reversible, and the energy dissipation is minimal.

As the field increases to Stage 2 ($H_{th_1} < H \leq H_{th_2}$), irreversible domain wall displacement becomes the dominant process. Domain walls move to expand favorably oriented domains by overcoming energy barriers imposed by pinning sites (microstructural imperfections like impurities, defects, grain boundaries, and internal stresses). As the field is strong enough, the domain wall suddenly breaks free from the pinning site, resulting in abrupt, irreversible jumps in magnetization known as Barkhausen jumps [52]. The energy required to overcome these pinning forces is dissipated as heat, constituting the primary source of hysteresis loss in this stage. Figure 2.1(a) (introduced in Section 2.1's introduction) visually illustrates a domain wall interacting with pinning sites under an applied field, further highlighting this mechanism.

In Stage 3, at higher field strengths ($H > H_{th_2}$), particularly as domain wall motion becomes saturated, domain rotation becomes the dominant magnetization process. Magnetic moments within domains rotate towards alignment with the applied field direction, often against the forces imposed by magnetic anisotropy and internal stresses. While domain rotation can have a reversible component, irreversible rotation can also occur, contributing to the total hysteresis loss, especially as the material approaches saturation.

The cumulative effect of these irreversible domain processes, particularly the Barkhausen jumps in Stage 2 and irreversible rotation in Stage 3, is directly reflected in the shape and width of the $\mathbf{B}$–$\mathbf{H}$ loop. The area enclosed by the $\mathbf{B}$–$\mathbf{H}$ loop during a full magnetization cycle quantifies the total energy dissipated as hysteresis loss per unit volume. This loss is primarily determined by the material's intrinsic properties (microstructure, stress, anisotropy) and the amplitude of the excitation field. At low frequencies, it is generally considered independent of the rate of change of the field, as it represents the energy cost per cycle.

2.1.2 Classical Eddy Current Loss

The classical eddy current loss (P_{eddy}) is a dynamic component of core loss in Bertotti's theory, arising from the macroscopic, global eddy currents induced within the conductive magnetic material by the time-varying magnetic flux.

The generation of classical eddy currents is a direct consequence of Faraday's Law of Induction in conductive materials. When a time-varying magnetic field is applied to a conductive magnetic core, a time-varying magnetic flux density is established within the material. This changing flux density induces an electric field, which in turn drives macroscopic eddy currents to circulate within the bulk of the core material. These currents typically follow closed paths perpendicular to the direction of the magnetic flux. Figure 2.4(a) provides a canonical illustration using a wound rod, showing the applied field (H_a) generated by the winding current (i_w) inducing circulating eddy currents (i_{ec}) within the rod. According to Lenz's Law, these induced currents generate a magnetic field (H_{ec}) that opposes the change in H_a.

These global eddy currents flow throughout the core cross-section, dissipating energy as heat according to $P = I^2R$. The distribution and magnitude of these currents, as well as the resulting total magnetic field ($H = H_a + H_{ec}$) within the material, are governed by Maxwell's equations. At low frequencies, the induced currents are relatively small, and the magnetic flux distribution is nearly uniform across the core cross-section. However, as frequency increases, the magnitude of the induced eddy currents and their opposing field (H_{ec}) become more significant. This leads to a non-uniform flux distribution where the magnetic flux is increasingly concentrated near the surface of the core, and the current density is highest at the surface and decays towards the interior – a phenomenon known as the skin effect. Figure 2.4(b) conceptually illustrates this effect, showing how H_{ec} opposes H_a, resulting in a reduced total magnetic field in the interior compared to the surface. This skin effect increases the effective resistance encountered by the eddy currents and complicates the calculation of classical loss.

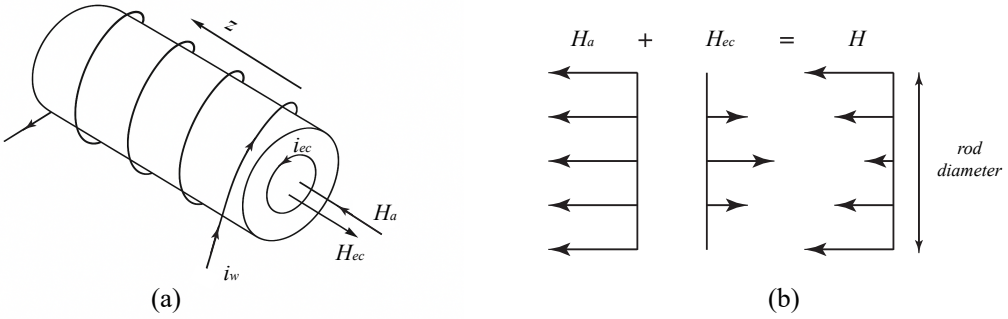

FIGURE 2.4: Illustration of classical eddy current generation and skin effect [25]: (a) Circulating eddy currents; (b) Conceptual illustration of skin effect.

The classical eddy current loss is primarily influenced by the frequency and amplitude of the magnetic excitation, the material's electrical conductivity, and the geometry and dimensions of the core, including lamination thickness for laminated materials. Its dependence on these factors, particularly its approximate proportionality to the square of frequency (f^2) and flux density amplitude in simplified scenarios (where skin effect is negligible), is a key characteristic that distinguishes it from hysteresis loss. Unlike hysteresis loss, which is primarily related to the energy cost per cycle of irreversible domain changes, classical eddy current loss is directly proportional to the rate at which magnetic flux changes $\frac{dB}{dt}$, making it a

key dynamic loss component. It is distinct from anomalous loss, which is attributed to more localized, microscopic current effects (as depicted conceptually on Figure 2.1(b)).

2.1.3 Anomalous Loss

The anomalous loss (P_{anom}) is the third component in Bertotti's theory, representing the portion of dynamic loss that is not accounted for by the classical eddy current calculation. It arises from dynamic energy dissipation mechanisms that are more complex and often microscopic compared to the macroscopic classical eddy currents.

While the classical eddy current model (Section 2.1.2) assumes a uniform material and a relatively smooth, macroscopic change in flux density, the actual dynamic magnetization process, particularly domain wall motion, is non-uniform and often discontinuous at the microscopic level. This deviation from the idealized classical model is the primary source of anomalous loss.

A key proposed mechanism for anomalous loss is the generation of localized eddy currents circulating specifically in the vicinity of moving domain walls. Unlike the macroscopic, global eddy currents that span the entire core cross-section (responsible for classical loss and skin effect), these localized currents are induced by the rapid, non-uniform motion of individual domain walls. As a domain wall sweeps through the material, the magnetic flux changes very rapidly locally, inducing intense eddy currents confined to the region immediately surrounding the moving wall. These localized currents dissipate energy as heat due to the material's resistivity, contributing to the anomalous loss.

Other mechanisms can also contribute to anomalous loss, particularly at high frequencies, including magnetic resonances. These resonances can occur when the frequency of the applied field matches the natural precession frequencies of magnetic moments at the atomic or nuclear level, leading to energy absorption. Such phenomena involve complex interactions between the applied field and the net magnetic moment of the atom or even the nuclear magnetic moment, and their detailed analysis is beyond the scope of this thesis. For a more

in-depth understanding of these mechanisms, readers are referred to specialized literature [25], [53]–[55].

The anomalous loss is also frequency-dependent, it shows a dependence on frequency that is proportional to frequency raised to the power of 1.5 ($f^{\frac{3}{2}}$), reflecting a fractional order dependence, contrasting with the f^2 dependence of classical loss. To illustrate how these different loss components contribute across the frequency spectrum, Figure 2.5 provides a visual summary of their characteristic dependencies and how they sum to the total loss, plotted as power per unit frequency (P/f) against frequency (f). As shown, the different loss components exhibit distinct behaviors in the P/f plot, reflecting their varying proportionality to frequency (as discussed in Section 2.1). The total core loss (solid line) is the sum of these three components, demonstrating how different mechanisms dominate at different frequency ranges. This distinct frequency behavior is a key aspect that core loss models must capture.

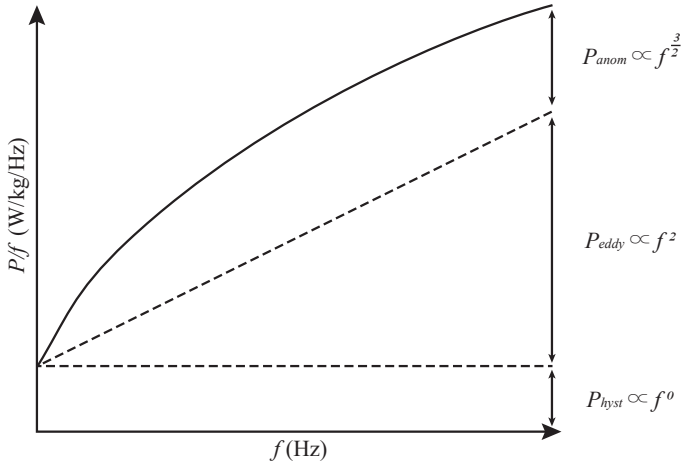

FIGURE 2.5: Frequency dependence of core loss components.

2.2 Review of Model-Driven Approaches Core Loss Modeling Approaches

Model-driven approaches represent a significant category of core loss modeling techniques that rely on pre-defined mathematical structures derived from either empirical observations or fundamental physical principles. These models typically involve fitting parameters to

experimental data or calculating them based on material properties and geometry. While offering potential advantages in interpretability and, in some cases, scalability, these traditional methods often struggle to achieve the required accuracy and generality under the complex operating conditions encountered in modern power electronics. This section reviews the evolution of model-driven approaches, highlighting their principles, strengths, and, crucially, their limitations, particularly concerning accuracy under arbitrary excitations and generality across diverse conditions.

2.2.1 Empirical Core Loss Models (Steinmetz and Variants)

Among the earliest and most widely used model-driven approaches are empirical models that directly calculate core loss based on excitation parameters. These methods are primarily phenomenological, relying on fitting mathematical formulas to experimental data rather than explicitly modeling the underlying physical mechanisms.

The foundational approach is the Original Steinmetz Equation (OSE), proposed in 1892 [2], which describes core loss per unit volume (P_v) for sinusoidal excitation as:

$$P_v = k f^{\alpha} B_m^{\beta}, \tag{2.2}$$

where f is frequency, B_m is peak flux density, and k, α, β are fitting parameters. While simple and computationally efficient, OSE is strictly valid only for sinusoidal waveforms and struggles to accurately predict losses under the non-sinusoidal excitations prevalent in modern power electronics [56].

Recognizing this limitation, a family of empirical variants has been proposed over time with the primary purpose of extending the Steinmetz approach to non-sinusoidal waveforms. These variants attempt to incorporate the influence of waveform shape by relating core loss to instantaneous values or derivatives of the magnetic flux density ($\frac{dB}{dt}$). Examples include the Modified Steinmetz Equation (MSE) [3], which relates loss to the integral of a power of the instantaneous rate of change of flux density ($\int (\frac{dB}{dt})^2 dt$). the Generalized

Steinmetz Equation (GSE) [4], which integration considers not only $\frac{dB}{dt}$ but also instantaneous B ($\int |\frac{dB}{dt}|^{\alpha}|B|^{\beta-\alpha}dt$).

A significant advancement and one of the most general and widely used empirical models for non-sinusoidal waveforms is the Improved Generalized Steinmetz Equation (iGSE) [5]–[7]. The iGSE addresses non-sinusoidal waveforms by dividing the magnetic flux waveform into the major loop and the minor loop and calculating the loss of the major loop and each minor loop separately. This method attempts to account for the history-dependent nature of core loss introduced by minor loops. The total core loss per unit volume in iGSE is typically expressed as the average of an instantaneous power loss function over a cycle:

$$P_v = \frac{1}{T}\int_0^T k_i \left|\frac{dB(t)}{dt}\right|^{\alpha} (B_m^{\beta-\alpha})dt, \tag{2.3}$$

where k_i, α, β are fitting parameters, B_m is the peak flux density of the waveform, and the integral is taken over one period T.

Following the development of iGSE, a similar variant, the Natural Steinmetz Equation (NSE) [8] was proposed, which focuses on the impact of rectangular switching waveforms like those produced by PWM converters. Building upon the iGSE concept, subsequent refinements have been proposed, such as the Improved iGSE (I²GSE) [9], [10]. The I²GSE attempts to add a loss component caused by the magnetic relaxation effect, aiming for better accuracy under dynamic conditions.

In summary, the family of Steinmetz-based empirical models provides a computationally simple and efficient approach to core loss estimation by fitting parameters to experimental data. Their primary strength lies in their ease of implementation and speed for routine calculations. However, their fundamental limitation is their phenomenological nature and lack of explicit physical basis. While variants like iGSE and I²GSE improve accuracy for some non-sinusoidal waveforms by considering waveform dynamics and relaxation effects, they still struggle with truly arbitrary or complex excitations, fail to capture history-dependent effects or DC bias accurately, and their parameters are typically only valid for limited operating ranges and specific materials. They offer no inherent scalability to different component geometries or

TABLE 2.1: Summary of Prominent Empirical Core Loss Models (Steinmetz Variants)

Model	Principles	Strengths	Limitations
OSE	Direct power law fit	Simple, fast estimation	Only valid for sinusoidal input
MSE	Relates loss to integral of dB/dt	Supports PWM waveforms	Accuracy degrades with harmonics
GSE	Relates loss to integral of dB/dt and B	DC-bias sensitivity	Not ideal for asymmetric loops
IGSE	Major/minor loop decomposition	Handles DC bias and asymmetry	Less accurate for complex minor loops
NSE	Equivalent to IGSE	Suitable for rectangular signals	Less accurate for complex minor loops
I^2GSE	Material relaxation effect	Most accurate; physics-based	Requires non-standard parameters

Note: **OSE**: Original Steinmetz Equation; **MSE**: Modified Steinmetz Equation; **GSE**: Generalized Steinmetz Equation; **IGSE**: Improved Generalized Steinmetz Equation; **NSE**: Natural Steinmetz Equation; **I^2GSE**: Improved iGSE.

direct insight into the underlying physics. Table 2.1 summarizes the key characteristics and differences among the prominent Steinmetz variants discussed.

2.2.2 Analytical Hysteresis Models

Parallel to the development of empirical core loss formulas, other early attempts to model magnetic behavior focused on finding mathematical expressions to describe the relationship between magnetic field (H) and magnetic flux density (B) – the $\mathbf{B}$–$\mathbf{H}$ loop. These methods aimed to capture the non-linear magnetization characteristic through fitting mathematical functions to experimental data, from which core loss could then be calculated by integrating the loop area ($\oint HdB$).

Early attempts to model hysteresis started from fitting analytical equations directly to actual magnetization data. However, developing a single satisfactory equation capable of accurately describing the complex, history-dependent processes involved across various conditions proved challenging [11]–[14]. Various analytical expressions have been used as approaches

to the empirical curve fitting method for $\mathbf{B}$–$\mathbf{H}$ loops. These include power series [15]–[17], rational polynomial [18]–[20], and some other analytical expressions [21], [22]. While these methods provide a mathematical representation of the $\mathbf{B}$–$\mathbf{H}$ curve and can approximate specific loops, they generally struggle to accurately represent complex hysteresis phenomena, particularly history dependence and intricate minor loops. Their accuracy is often limited to the specific loop shapes and conditions of the fitted data, and they lack a physical basis, limiting their predictive capability and insight. They also do not inherently account for dynamic effects or component geometry.

These Analytical hysteresis models differ from the Physics-Based hysteresis models discussed next, which attempt to build the $\mathbf{B}$–$\mathbf{H}$ relationship from more fundamental physical principles like domain behavior or operator theory, aiming for greater physical interpretability and predictive power across conditions.

2.2.3 Physics-Based Hysteresis Models (Material Level)

Moving beyond purely empirical fitting, Physics-Based Hysteresis Models aim to describe the intrinsic magnetic material behavior, based on more fundamental physical principles underlying the magnetization process, such as magnetic domain behavior or operator theory.

It is worth noting that while some literature classifies operator-based models, such as the Preisach and Prandtl-Ishlinskii models, as phenomenological or mathematical models due to their input-output description rather than direct derivation from microscopic physics [57]–[59], they inherently capture key magnetic phenomena such as irreversibility and memory through constructs like hysterons and operators. These structural features, inspired by physical behavior, offer deeper physical insight than purely empirical or curve-fitting approaches. For clarity in this thesis, and to reflect their relative physical interpretability, these models are grouped under the broader category of Physics-Based Hysteresis Models.

Numerous physics-based hysteresis models have been developed over time [13], [23]–[25]. Among these, the Jiles-Atherton (J-A) model [12], [24], [26] and the Preisach model [27] are arguably the most well-known and widely studied.

The Jiles-Atherton (J-A) model [26] is based on the physical concepts of domain wall motion and rotation, influenced by an effective magnetic field (H_{eff}). It formulates the magnetization process through a set of differential equations, separating the magnetization into reversible (M_{rev}) and irreversible components (M_{irr}) components, where the total magnetization is

$$M = M_{rev} + M_{irr}. \tag{2.4}$$

To calculate the two components, Jiles and Atherton introduced the concept of anhysteretic magnetization (M_{an}). Representing the ideal reversible magnetization in the absence of hysteresis, M_{an} is often described by the Langevin function for isotropic materials [12], [24]. Ultimately, the J-A model can be written as:

$$\frac{dM}{dH} = \frac{(1-c)(M_{an}-M) + ck\delta\frac{dM_{an}}{dH}}{k\delta - \alpha(1-c)(M_{an}-M)}, \tag{2.5}$$

where c is a parameter related to reversible susceptibility, k is a parameter linked to the hysteresis losses, and δ takes the value +1 when $\frac{dH}{dt} > 0$ and -1 when $\frac{dH}{dt} < 0$. The model's strength lies in its connection to physical parameters that can, in principle, be related to material properties. However, accurately capturing complex hysteresis phenomena, particularly intricate minor loops and the precise interaction between reversible and irreversible components under arbitrary excitations, can be challenging in practice [60]. Furthermore, the accuracy of the J-A model is significantly influenced by the definition used for the anhysteretic magnetization; simple models like the Langevin equation may not be applicable to all material types or complex behaviors [61]. Parameter identification for the J-A model can also be a non-trivial task [62].

The Preisach model [27], on the other hand, is based on the concept of representing the magnetic material as an aggregation of independent elementary hysterons, each exhibiting a simple rectangular hysteresis loop with specific switching thresholds (α and β). The fundamental building block of the Preisach model is this elementary hysteron, often represented as a simple relay operator. Figure 2.6(a) illustrates this Preisach elementary hysteron, which exhibits a rectangular hysteresis loop defined by α and β. The macroscopic behavior is obtained by summing the responses of a distribution of these hysterons. The total magnetization (M) at

a given field history is calculated by integrating the contribution of each hysteron over the Preisach plane:

$$M(t) = \iint_{\alpha \geq \beta} \mu(\alpha, \beta) \gamma_{\alpha\beta}(H(t)) d\alpha d\beta, \tag{2.6}$$

where $\gamma_{\alpha\beta}(H(t))$ is the output of the elementary hysteron with thresholds α and β for the input field $H(t)$, and $\mu(\alpha, \beta)$ is the distribution function on the Preisach plane. A key strength of the Preisach model is its inherent ability to capture history dependence and model complex minor loops accurately, provided the distribution function $\mu(\alpha, \beta)$ is correctly identified. However, identifying this distribution from experimental data is often a complex process [63], [64], and the classical Preisach model is typically a scalar model that does not explicitly account for reversible magnetization or vector effects [65], [66].

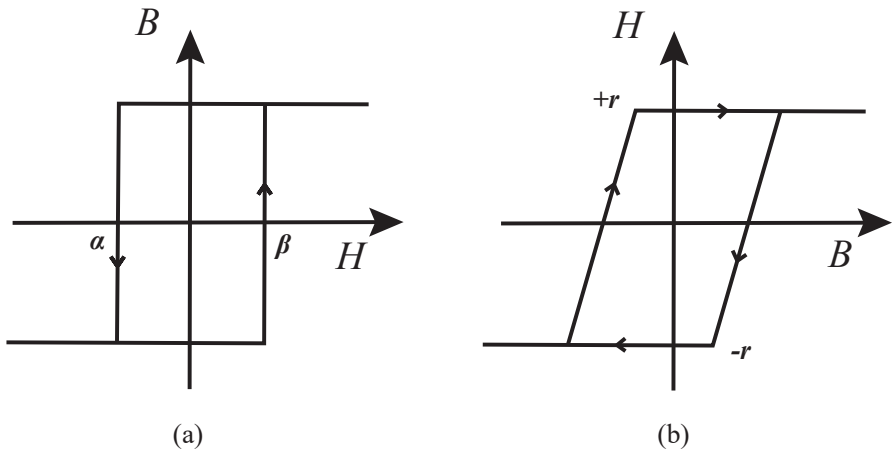

FIGURE 2.6: Schematic diagrams illustrating the core idea of (a) Preisach hysterons or (b) PI operators.

Another significant physics-based model is the Prandtl-Ishlinskii (PI) model [28]. Mathematically related to the Preisach model, the PI model represents hysteresis as a superposition of simple operators with varying thresholds. The PI stop operator, characteristic of many PI model implementations, can be conceptually understood as a combination of a positive linear slope and a superposition of some Preisach operators [66], [67]. Figure 2.6(b) shows the characteristic behavior of the PI stop operator, defined by threshold r. Its strength lies in its mathematical tractability and the continuity of its operators, which can be advantageous for implementation. However, similar to the classical Preisach model, accurately capturing all aspects of complex hysteresis, including the precise nature of reversible components

and intricate history dependence, can depend heavily on the specific implementation and parameterization of the operators [65], [66].

While these physics-based hysteresis models provide valuable physical insights and can model hysteresis loops, they primarily describe the material's magnetic characteristics at a fundamental level. They do not inherently include dynamic effects like eddy currents or explicitly account for component geometry and dimensions. For full core loss prediction, especially at higher frequencies, they need to be coupled with models that incorporate these dynamic and geometric effects. Furthermore, achieving high accuracy under truly arbitrary excitations and consistently identifying robust parameters remain challenges for many implementations.

2.2.4 Physics-Based Dynamic Models (Component Level)

While the Physics-Based Hysteresis Models discussed in Section 2.2.3 provide valuable insights into the intrinsic material behavior (the $\mathbf{B}$–$\mathbf{H}$ loop), they primarily operate at the material level and do not inherently account for dynamic effects like eddy currents or the influence of component geometry and dimensions. For accurate core loss prediction, particularly at higher frequencies where dynamic losses become significant, models that incorporate these aspects are necessary. Physics-Based Dynamic Models aim to address this by building upon material models and integrating them within a framework that considers the electromagnetic field distribution and current induction within the physical component.

A common and rigorous approach in developing Physics-Based Dynamic Models is the use of equivalent circuit or magnetic circuit analogies derived from Maxwell's equations to represent the magnetic component and the spatial distribution of electromagnetic fields and currents within it. This approach, which seeks to represent the complex field phenomena through interconnected circuit elements, has roots in earlier work. For instance, Chua's work in the 1970s [29], [30] explored lumped-circuit models for nonlinear inductors exhibiting hysteresis loops, demonstrating the potential of circuit analogies for magnetic components, although these early models were often limited to low-frequency applications or simplified geometries.

Building upon this foundation, a significant development utilizing this approach is the Generalized Dynamic Circuit Model (GDCM) [31]–[33], introduced in the mid-1990s. Derived from Maxwell's equations and circuit analogies, the GDCM conceptually represents the magnetic core's cross-section as a network of coupled electrical circuits. Figure 2.7 illustrates the core idea of the GDCM. Figure 2.7(a) shows how the core cross-section is conceptually discretized into multiple concentric segments, each with an induced current loop. Figure 2.7(b) then presents the equivalent electrical circuit analogy for these segments, represented as a network of coupled RL meshes. The dynamic interaction between the applied magnetic field (driven by the coil voltage V_s), the material's response (represented by a material model within each inductive element), and the induced eddy currents within each segment is captured by the circuit equations, which are often formulated as a system of differential equations. The GDCM's strength lies in its ability to explicitly model dynamic effects such as eddy currents and skin effect, and its inherent scalability based on core geometry and material conductivity [32], [68].

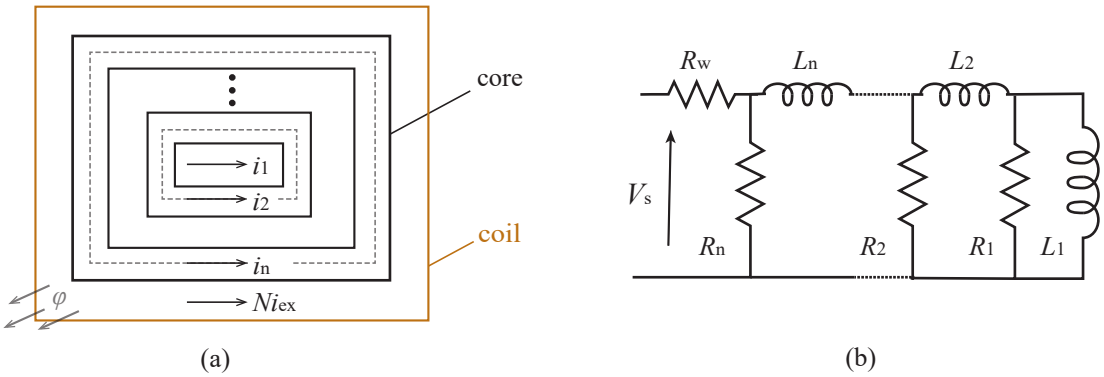

FIGURE 2.7: The Generalized Dynamic Circuit Model: (a) Conceptual discretization of the core cross-section; (b) Equivalent circuit analogy.

The concept of representing dynamic magnetic components using equivalent circuits or magnetic circuits has been extended and applied in various ways beyond the GDCM, demonstrating the versatility of this approach in addressing different complexities and application needs. For example, these component-level circuit models can be integrated into larger electrical circuit simulations to analyze the dynamic behavior of magnetic components within a power electronic system, sometimes including coupled physics like dynamic thermal effects [62]. Dynamic magnetic circuit models have also been proposed to explicitly account for

nonlinear effects such as iron saturation and core losses within the circuit formulation itself [69]. Furthermore, systematic circuit analogies have been applied to model impedances and current distribution in specific geometries such as planar magnetics [70], addressing the unique dynamic challenges of those structures.

The primary strength of Physics-Based Dynamic Models, particularly those based on equivalent circuit/magnetic circuit analogies like the GDCM, lies in their ability to explicitly model dynamic effects such as eddy currents and skin effect, and their inherent scalability based on core geometry and material conductivity [32], [68]. By calculating fields and currents within different segments or circuit elements, they can also provide insight into the spatial distribution of electromagnetic phenomena within the core. However, a fundamental limitation shared by most Physics-Based Dynamic Models, including those based on equivalent circuits, is that their overall accuracy is fundamentally limited by the fidelity of the material model used to describe the non-linear magnetic behavior (the $\mathbf{B}$–$\mathbf{H}$ relationship) within each segment or circuit element. If a simplified hysteresis model (e.g., a basic Preisach or J-A implementation that struggles with complex excitations) is used as the material law within the circuit framework, the overall dynamic model will still struggle to accurately predict core loss and magnetic behavior under complex and arbitrary excitation waveforms. Furthermore, parameter identification for dynamic coefficients and the computational cost of solving the system of differential equations, especially for complex geometries or high levels of discretization, can also be limitations.

2.3 Review of Data-Driven Approaches for Magnetic Modeling

With the rapid advancements in machine learning (ML) and computational capabilities, data-driven approaches have emerged as a powerful alternative paradigm for modeling complex nonlinear systems, including magnetic materials and components. Unlike model-driven methods that rely on pre-defined mathematical structures, data-driven models learn relationships directly from experimental data. This section reviews the application of data-driven techniques,

particularly neural networks, in magnetic modeling, covering both pure data-driven methods and existing hybrid approaches that combine data with physics.

2.3.1 Pure Data-Driven Models (Neural Networks)

Pure data-driven models in magnetic modeling represent a paradigm shift from traditional model-driven approaches, relying entirely on experimental data to learn the complex relationships between excitation signals and magnetic responses or core loss. These models do not explicitly incorporate physical equations or structures derived from fundamental principles, instead leveraging the pattern recognition capabilities of machine learning algorithms, primarily neural networks (NNs). Various NN architectures have been explored for this purpose, including Feedforward Neural Networks (FNNs) [35]–[38], Recurrent Neural Networks (RNNs) like Long Short-Term Memory (LSTM) networks [39]–[41], Convolutional Neural Networks (CNNs) [42], [43], and Neural Operators [44].

The core principle of pure data-driven models is to train a neural network to minimize the discrepancy between its predictions and measured experimental data. This is achieved by optimizing the network's internal parameters through algorithms like backpropagation, based on a given set of input-output pairs (e.g., magnetic flux density $B(t)$ as input, magnetic field $H(t)$ or core loss P_v as output). When trained on sufficient and representative data, pure data-driven models, particularly deep neural networks, demonstrate a strong ability to capture complex, non-linear relationships and intricate patterns directly from data. They can achieve impressive accuracy for predicting magnetic behavior or core loss within the domain of the training data, offering flexibility in modeling complex phenomena without requiring explicit physical formulation.

However, despite their accuracy on trained data, pure data-driven models face significant limitations in the context of core loss modeling for power electronics. A primary challenge is their high data requirement. Training these models effectively to generalize across the wide range of operating conditions (excitation waveform, frequency, temperature) and component geometries encountered in power electronics typically necessitates large, comprehensive, and

well-labeled datasets [45], [71], [72]. Collecting such extensive experimental data, especially under diverse and controlled conditions, is often time-consuming and costly. Consequently, these models often exhibit limited generalization and struggle to accurately predict magnetic behavior or core loss for conditions or excitation types that are significantly different from the training data distribution.

Furthermore, a crucial limitation for practical design is the lack of explicit scalability to new component dimensions. Pure data-driven models lack inherent awareness of component geometry. While training on data from components of different sizes is possible if included in the training set, predicting the behavior of a new component size or geometry that was not included in the training set typically requires collecting new experimental data for that specific size and retraining the model from scratch or via fine-tuning. This process is inefficient and impractical for design cycles involving multiple component variations [38], [45]. Additionally, the "black box" nature of many pure data-driven models hinders physical interpretability, making it difficult to gain insights into the underlying magnetization process or guide material development based on physical principles [72], [73].

2.3.2 Existing Hybrid Physics-Data Models

To address some of the inherent limitations of both purely model-driven and pure data-driven approaches discussed in the preceding sections, hybrid physics-data models have been explored in magnetic modeling. These methods attempt to combine data-driven techniques with some level of physical information or constraints. Essentially, the integration of physical priors aims to reduce the complexity of the model architecture and training process, guiding the search subspace closer to the optimal solution. This concept is conceptually illustrated in Figure 2.8.

Physics-informed machine learning generally encompasses two main approaches to integrate physical knowledge into machine learning models [74]:

- **Physics-informed loss function:** This approach, famously proposed by the original Physics-Informed Neural Network (PINN) framework [75], incorporates physical

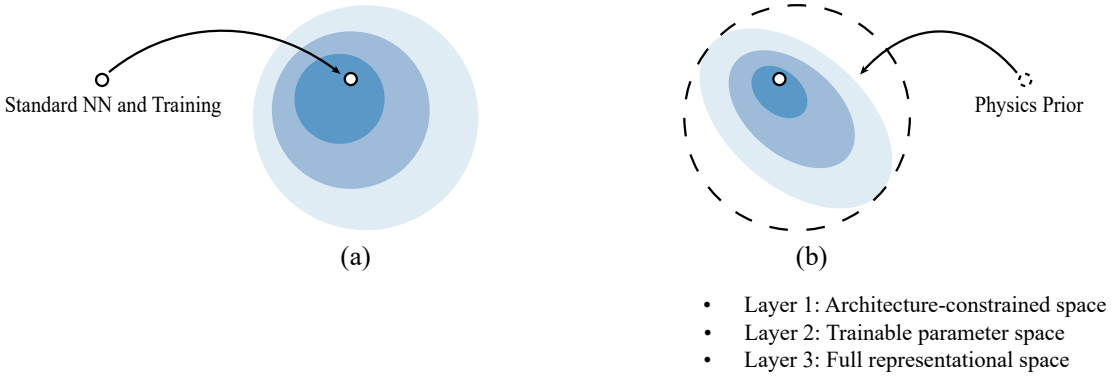

FIGURE 2.8: Conceptual illustration of how incorporating physical priors can reduce the search space for model parameters: (a) Pure data-driven model; (b) Hybrid-driven model.

laws or constraints directly into the model's loss function during training. The loss function typically follows a general form that includes both a data-driven term (minimizing the error between model predictions and measured data) and a physics-informed term (penalizing deviations from physical laws). For example, in magnetic modeling, the physics-informed term could penalize the model if its predicted magnetic fields or flux densities do not satisfy Maxwell's equations [76], [77] or if the predicted core loss deviates significantly from a physically derived constraint (e.g., based on simplified Steinmetz-like relationships [78], [79]). The general form of the loss function can be written as:

$$Loss = Loss_{data} + \lambda Loss_{Physics}, \tag{2.7}$$

where $Loss_{data}$ quantifies the fit to experimental data, $Loss_{Physics}$ quantifies the adherence to physical laws, and λ is a weighting parameter.

- **Physics-informed architecture:** This approach focuses on designing the neural network architecture itself to inherently integrate prior physics knowledge. This can involve structuring the network or its components to mimic physical processes or relationships. For example, this approach can be used to:
  - Develop neural networks that refine or predict parameters of traditional physics-based hysteresis models like the Preisach or Jiles-Atherton models [80]–[82].

Instead of fitting these parameters empirically, an NN is trained to predict them based on excitation conditions.

- Design network layers or subnetworks that represent physical operators or concepts from hysteresis models (e.g., a layer mimicking a physical operator from a hysteresis model, or assign certain neurons to represent specific physical quantities) [83]–[85]. This approach directly fuses some physical information into the network's structure.

Hybrid models offer several potential advantages. By incorporating physical knowledge, they can potentially reduce the data requirements compared to pure data-driven models, as the network doesn't have to learn the physics from scratch. They may also offer improved physical consistency or interpretability compared to black-box NNs, depending on the level of physical integration [86].

However, despite these potential benefits, existing hybrid approaches in magnetic core loss prediction have often focused on specific aspects and have not fully demonstrated a comprehensive solution that simultaneously achieves all the required properties for practical power electronics design. While some models improve accuracy for specific excitations or reduce data for parameter fitting, achieving consistently high accuracy under a wide range of arbitrary and complex excitations (including transients, DC bias, complex minor loops) can still be challenging if the physical formulation is simplified or the data-driven part struggles with generalization [87]. Crucially, robust scalability across different component dimensions with overall data efficiency for the entire design cycle remains a key challenge for many existing hybrid models. The physical information integrated might not explicitly handle geometry in a scalable way, or the data-driven part still requires significant data for generalization across dimensions and operating conditions simultaneously. Integrating different physical aspects (e.g., material behavior, dynamic effects, thermal effects) within a single, robust, and scalable hybrid framework is complex and an ongoing area of research.

2.4 Synthesis of Limitations and Research Gaps

Building upon the comprehensive review of existing core loss modeling approaches presented in Sections 2.2 (Model-Driven) and 2.3 (Data-Driven), this section synthesizes their respective strengths and limitations to identify the key research gaps. Table 2.2 provides a concise summary of the different model types within these two main paradigms, highlighting their respective strengths and limitations.

TABLE 2.2: Summary of Core Loss Modeling Schemes

Scheme	Model Type	Strengths	Limitations
Model-Driven	Empirical Models (OSE, MSE, iGSE, I²GSE, etc.)	Simple, low computation.	Lack physics, limited accuracy for complex waveforms and DC bias. No scalability.
	Analytical Hysteresis (Power Series, Rational Polynomial, etc.)	Simple, simulate specific $\mathbf{B}$–$\mathbf{H}$ loops.	Poor accuracy for complex loops, minor loops. Limited physical meaning.
	Physics-Based Hysteresis (Preisach, J-A, PI, etc.)	Interpretable, models hysteresis and minor loops.	Limited for arbitrary excitations. Complex parameter ID. No dynamics/geometry.
	Physics-Based Dynamic (GDCM, etc.)	Scalable, models dynamics and spatial effects.	Accuracy limited by material model. Complex identification, costly.
Data-Driven	Pure Data-Driven (FNN, RNN, LSTM, CNN, Transformer)	High accuracy on trained data, captures nonlinearities.	**High data need**, poor generalization, no scalability, no physics.
	Hybrid Physics-Data (PINNs, etc.)	Reduced data, better physical consistency.	**Partial focus**, hard to balance accuracy, scalability, and data efficiency. Complex integration.

As illustrated in Table 2.2, no single existing approach effectively achieves the critical requirements of high accuracy under arbitrary excitations, robust scalability across varying component dimensions, broad generality, and data efficiency that are essential for modern power electronics design automation.

Model-Driven Approaches, as reviewed in Section 2.2, are often rooted in physical principles or mathematical structures. Many of these models offer simplicity and computational efficiency. They also provide some degree of interpretability and, in the case of Physics-Based

Dynamic models like GDCM, inherent scalability based on geometry. However, as summarized in Table 2.2, they fundamentally struggle to achieve high accuracy and generality when faced with complex and arbitrary excitation waveforms (harmonics, DC bias, transients, minor loops). This limitation stems from the fact that these models often simplify the simulation of the true magnetization mechanisms (such as intricate domain wall dynamics), complex parameter identification processes, or rely on empirical formulations that do not fully capture the intricate behavior. This simplification leads to inaccuracies, particularly when dealing with complex, history-dependent magnetization.

Data-Driven Approaches, as reviewed in Section 2.3, leverage the power of machine learning to learn complex relationships directly from data. Pure data-driven models can achieve high accuracy within the domain of their training data. However, as highlighted in Table 2.2, they are severely limited by their high data requirement and lack of explicit scalability to new component dimensions or operating conditions not extensively covered in the training set. Generalization outside the training distribution is poor, and retraining for each new component size is impractical. While existing hybrid models attempt to mitigate some of these issues by incorporating physical information, they often focus on specific aspects (e.g., parameter fitting, physical constraints) and have not yet demonstrated a comprehensive solution that achieves simultaneous high accuracy under arbitrary excitations and robust scalability across dimensions with overall data efficiency.

Therefore, a significant research gap exists in the development of a core loss modeling approach that can effectively bridge these limitations and simultaneously deliver:

- **High Accuracy:** Precise prediction of core loss and magnetic behavior under a wide range of complex and arbitrary excitation waveforms.
- **Robust Scalability:** Accurate prediction for components of different physical dimensions and geometries using the same material, with minimal dimension-specific data.
- **Broad Generality:** Reliable performance across diverse operating conditions and potentially different materials.

- **Data Efficiency:** Reduced reliance on extensive experimental data for model development and deployment.

Addressing this multifaceted gap is crucial for enabling the next generation of magnetic component design tools and accelerating innovation in high-performance power electronics. Recognizing that no single existing approach fully addresses all these requirements, the research presented in this thesis is motivated by this identified gap and systematically explores novel hybrid physics-neural network strategies, each designed to tackle specific, progressively complex aspects of this grand challenge, laying the groundwork for a comprehensive solution.

CHAPTER 3

The Magnetization Mechanism-Inspired Neural Network (MMINN)

This chapter introduces the MMINN, the first hybrid modeling strategy explored in this thesis. It details the model's architecture, implementation, and experimental validation for core loss estimation under steady-state, high-frequency, symmetric waveforms, representing an initial exploration into leveraging physical intuition for neural network design.

The primary contribution of the MMINN lies not merely in the separate calculation of loss components, but in the architectural embedding of the physical magnetization principles. Unlike conventional black-box models, the MMINN is designed to mathematically mirror Bertotti's Loss Separation Theory through structural constraints. By constructing the network using Prandtl-Ishlinskii (PI) operators as intrinsic activation functions and implementing physics-based feature segregation, the model enforces physical consistency. This design shifts the learning task from discovering physical laws from scratch to parameterizing a pre-defined physical framework.

3.1 Introduction

The relentless drive towards higher power density and efficiency in modern power electronics systems necessitates accurate and scalable modeling of magnetic components. As power converters increasingly operate at higher frequencies, magnetic components are pushed to their limits, often experiencing saturation and operating within highly non-linear regions of their magnetic material characteristics. In many practical power electronic applications, these components operate in a steady-state regime where the magnetic flux density exhibits periodic and symmetrical waveforms. Under these steady-state, high-frequency conditions, the interplay of hysteresis and dynamic losses becomes critical, and the need for efficient and accurate prediction is paramount for design optimization.

Existing methods for modeling core losses present a significant dilemma. Conventional physics-driven models, while offering interpretability, often rely on simplified assumptions about material behavior that limit their accuracy under the complex, non-linear magnetic

responses encountered at high frequencies, particularly when these responses are not purely sinusoidal. Purely data-driven neural networks, on the other hand, can achieve impressive accuracy by learning directly from data, but they typically demand extensive datasets and can lack inherent physical insights.

To address the prevalent need for accurate core loss prediction in steady-state, high-frequency, symmetric excitation scenarios, this chapter introduces the MMINN, initially proposed in [88], [89]. the MMINN was conceived to leverage the strengths of both physics-based and data-driven approaches, aiming for data efficiency and competitive accuracy specifically for these common operating conditions. By incorporating fundamental physical mechanisms relevant to core loss, such as the separation of hysteresis and dynamic loss components, and leveraging neural networks to parameterize these mechanisms, the MMINN seeks to achieve a balance between accuracy and modest model complexity. This approach is particularly well-suited for routine factory testing scenarios where efficient and reliable core loss prediction is essential.

The core idea behind the MMINN is to draw inspiration from the fundamental physical magnetization process of magnetic materials at the macro-level and parameterize this process using neural networks. Specifically, inspired by the decomposition principle used in core loss separation theory (Section 2.1), the MMINN applies a similar approach to the overall magnetic field strength (H). The magnetic field H is decoupled into a hysteresis component (H_h) and a dynamic component (H_{dyn}):

$$H = H_h + H_{dyn}, \tag{3.1}$$

Figure 3.1 illustrates this conceptual physical decomposition. H_h accounts for the energy dissipation from domain processes, while H_{dyn} accounts for the impedance due to eddy currents (both global and local). This decomposition of the magnetic field response guides the design of the MMINN architecture. The design of each component model is specifically inspired by established physical modeling concepts for hysteresis and dynamic effects, as indicated in Figure 3.1. The Hysteresis component model adopts ideas from the Prandtl-Ishlinskii (PI) model (Section 2.2.3) to characterize the material's magnetic magnetization

changes related to hysteresis. The Dynamic component model, conversely, adopts the idea of segmentation (inspired by core loss ladder network concepts, Section 2.2.4) to account for the dynamic effects within the magnetic material. This approach aims to achieve not only high accuracy and computational efficiency but also potential advantages in simplicity (fewer parameters to tune) and generality (inheriting aspects from a physics-driven perspective) compared to purely empirical or fully data-driven models.

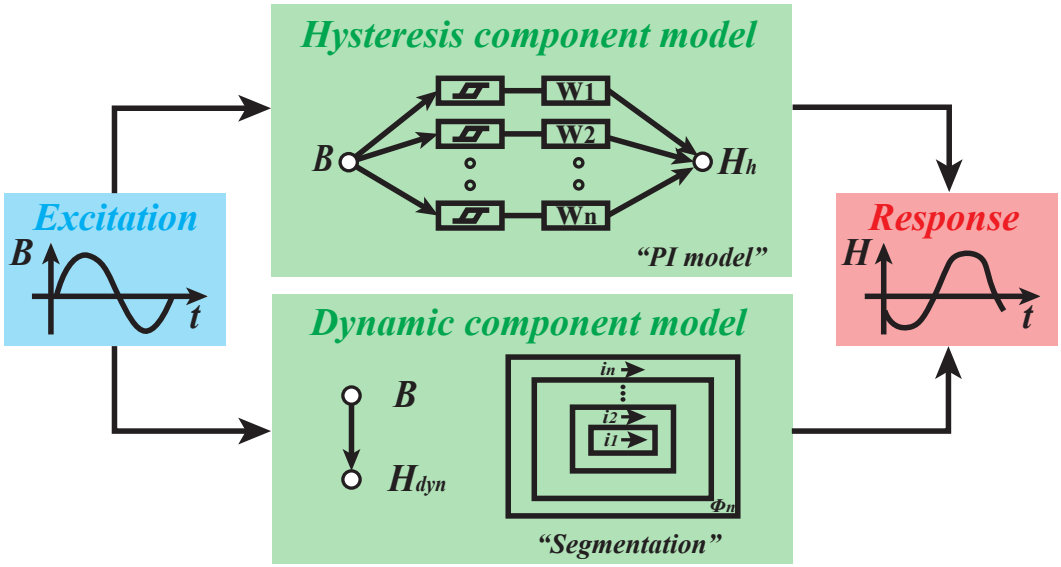

FIGURE 3.1: Conceptual decomposition of the magnetic field response into hysteresis and dynamic components.

The initial validation of the MMINN model, detailed in this chapter, focuses on its application for core loss estimation and dynamic hysteresis response prediction under steady-state, high-frequency, symmetric magnetic flux density excitation waveforms. The model training and testing are based on the open-source magnetic core loss database MagNet, which includes dynamic hysteresis responses under various excitations at high frequencies [40], [41], [45]. While the MMINN demonstrates promising results for its intended scope, its limitations in fully capturing history-dependent phenomena for arbitrary and transient waveforms motivate the subsequent development of HDPI-NN (Chapter 4) and the overarching NE-DCM framework (Chapter 5).

The remainder of this chapter details the MMINN model's architecture, its implementation and training methodology, and presents the experimental validation results, including a comparative analysis with other neural network models.

3.2 MMINN Model Architecture

The architecture of the MMINN model is directly structured to reflect this physical decomposition in (3.1). It consists of two main subnetworks: a Hysteresis Subnetwork responsible for modeling H_h, and a Dynamic Subnetwork responsible for modeling H_{dyn}. The final H is obtained by summing the outputs of these two subnetworks. Figure 3.2 illustrates the overall architecture of the MMINN model.

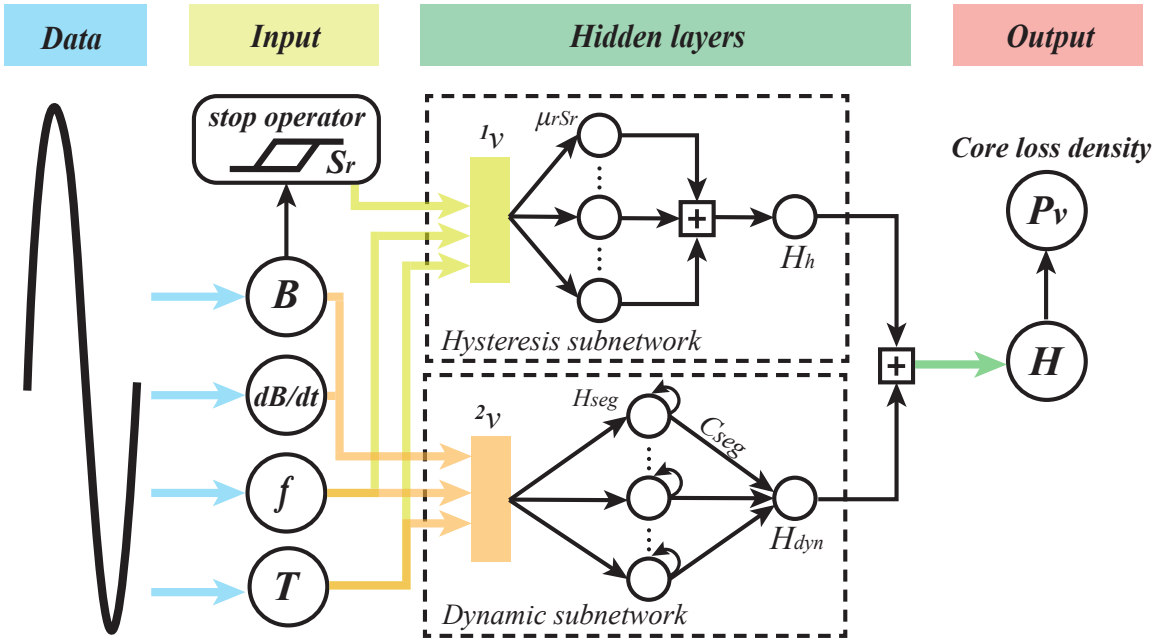

FIGURE 3.2: Architecture of the MMINN, consisting of a Hysteresis Subnetwork and a Dynamic Subnetwork.

3.2.1 Hysteresis Subnetwork

The Hysteresis Subnetwork focuses on simulating the magnetization behavior primarily caused by the movement of magnetic domains, which includes both domain wall motion

and domain rotation (Section 2.1.1). This process involves both reversible and irreversible energy changes. As mentioned in Section 3.1, this subnetwork is specifically inspired by the Prandtl-Ishlinskii (PI) model (Section 2.2.3), which represents hysteresis as a superposition of simple operators, such as the stop operator (Figure 2.6(b)), capable of describing these reversible and irreversible energy changes. The PI model for the hysteresis component H_h can be interpreted by:

$$H_h(B(t)) = \sum_{r \in \mathcal{R}} \mu_r(f, T)\, S_r(B(t)) \tag{3.2}$$

where S_r is the stop operator response and μ_r is the distribution proportion depending on frequency and temperature.

By adopting this formulation, the MMINN explicitly embeds physical mechanisms into its architecture. Instead of relying on standard activation functions (e.g., ReLU or Sigmoid) to approximate non-linearities from scratch, the subnetwork utilizes Stop Operators as intrinsic building blocks. This design imposes a structural constraint, ensuring that the network is mathematically composed of hysteretic elements capable of capturing irreversible domain wall motion and memory effects. Consequently, the model reduces the search space for parameters and does not need to learn the fundamental concept of hysteresis from massive datasets.

In the MMINN Hysteresis Subnetwork, the responses of conceptual PI stop operators (S_r) are treated as inputs to a feed-forward neural network (FNN). The discrete-time output signal $S_r(k)$ of a stop operator at time step k, parameterized by a threshold r, given an input signal $u(k)$, can be updated using a Symmetric Saturated Linear Unit (SSLU)[90]:

$$S_r[u(k)] = min\{r_i, max\{-r_i, u(k) - u(k-1) + S_r[u(k-1)]\}\}. \tag{3.3}$$

The FNN is designed to learn the weighted contribution ($\mu_r S_r$) of each conceptual stop operator. Let $y_{FNN,i}(t)$ denote the output of the FNN corresponding to the i-th conceptual operator at time t. The FNN effectively learns the distribution proportion μ_r implicitly within its output. From a physical perspective, the H_h arises from the collective behavior of magnetic domains, each conceptually represented by a stop operator. Therefore, the Hysteresis Subnetwork estimates H_h y summing the contributions learned by the FNN for all operators.

The output calculation of the Hysteresis Subnetwork can be represented as:

$$H_h(t) = \sum_{i=1}^{n} y_{FNN,i}(t), \tag{3.4}$$

where n is the number of conceptual operators.

3.2.2 Dynamic Subnetwork

The Dynamic Subnetwork is designed to model the contribution to the magnetic field arising from dynamic effects (H_{dyn}), primarily eddy currents (Section 2.1.2). This subnetwork adopts the idea of segmentation from the core loss ladder network concept proposed in [32], [33](Section 2.2.4). The ladder network approach conceptually discretizes the core cross-section into theoretical segments to account for the spatial distribution of electromagnetic fields and eddy currents, particularly relevant for modeling skin effect at higher frequencies. In the ladder network model, the magnetic flux within each segment is assumed to be uniformly distributed. A dynamic loss model is then applied to each segment to calculate its contribution to the dynamic magnetic field, as follows [23]:

$$H_{seg,i}(t) = C_{cl,i}\frac{dB(t)}{dt} + C_{a,i}\left|\frac{dB(t)}{dt}\right|^{0.5}, \tag{3.5}$$

where C_{cl} and C_a are loss coefficients associated with the sample, and $\frac{dB}{dt}$ is the flux density change rate. The total H_{dyn} is then related to the sum of these segment contributions.

In the MMINN Dynamic Subnetwork, the concept of segmenting the dynamic response is implemented using a Recurrent Neural Network (RNN). Recognizing that the precise dynamic field contribution from each conceptual segment is complex and not easily determined physically, the RNN is employed to learn these contributions directly from data. The number of hidden layer neurons in the RNN represents the number of conceptual segments within the core.

To ensure physical consistency, a strict feature selection strategy is applied to the network inputs, whick include the flux density (B), its rate of change ($\frac{dB}{dt}$), frequency (f) and temperature

(T). The RNN is designed to learn the dynamic effects associated with each conceptual segment's dynamic response. The output of the RNN for neuron k at time t, denoted $y_{RNN,k}(t)$, is designed to represent the dynamic effect within the k-th conceptual segment, providing the network with memory, which conforms to the dynamic characteristics of hysteresis.

The Dynamic Subnetwork estimates the H_{dyn} as a weighted sum of the dynamic effects represented by the RNN outputs. As depicted in Figure 3.2, the RNN outputs are fed into a final fully connected layer whose weights, learned during training, represent the dynamic effects contribution (C_{ceg}) for each conceptual segment. A hyperbolic tangent activation is then applied to introduce additional nonlinearity. The overall output of the Dynamic Subnetwork is given by:

$$H_{\text{dyn}}(t) = \tanh\left(\sum_{k=1}^{m} C_{\text{seg},k} \cdot y_{\text{RNN},k}(t)\right), \tag{3.6}$$

where m is the number of conceptual segments (RNN neurons).

3.3 Overall MMINN Model

As described in the preceding subsections, the MMINN model consists of two main subnetworks: the Hysteresis Subnetwork (Section 3.2.1) and the Dynamic Subnetwork (Section 3.2.2). The overall MMINN model integrates these two components by summing their outputs to predict the total H corresponding to the input excitation. This combination is consistent with the physical decomposition in Equation (3.1) and is illustrated in Figure 3.2 (Section 3.2). The inputs to the overall MMINN model are summarized in Table 3.1

3.4 Model Implementation and Training

This section details the practical aspects of implementing and training the MMINN model. The overall training workflow for the MMINN model involves several key steps, from data acquisition to saving the trained model parameters. Figure 3.3 provides a schematic illustration of this detailed training flow.

TABLE 3.1: Input and output variables used in the MMINN model

Variable	Description	Unit	I/O
B	Average magnetic flux density	T	Input
dB/dt	Time derivative of average magnetic flux density	T/s	Input
f	Operating frequency	Hz	Input
T	Ambient temperature	°C	Input
H	Average magnetic field strength	A/m	Output

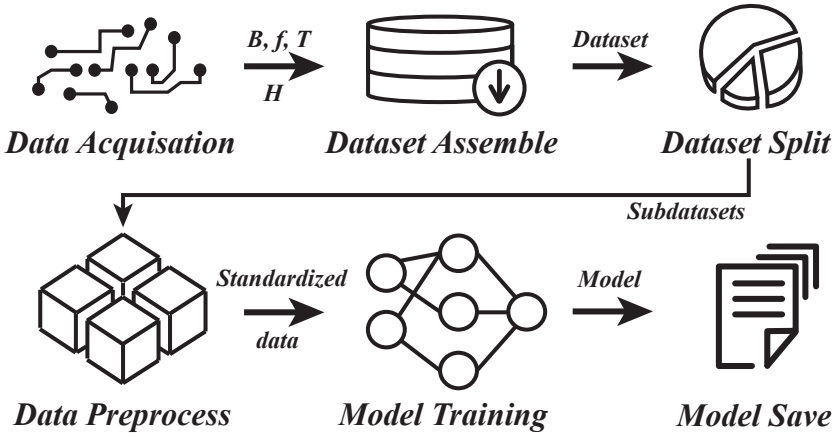

FIGURE 3.3: The MMINN training workflow diagram.

3.4.1 Data Acquisation and Data Preparation

The foundation of any data-driven or hybrid model lies in the quality and quantity of the data used for training. For the MMINN model, dynamic magnetization data, specifically B–H curves, are required, along with corresponding operating conditions such as temperature and frequency (or sampling time). Acquiring such data accurately across a wide range of conditions is a complex and time-consuming process.

In this work, the data acquisition is based on the MagNet open-source database [40], [41], [45]. The MagNet database provides a large collection of experimentally measured excitation and magnetic response pairs for 15 ferromagnetic materials under diverse operating conditions, including different waveforms, frequencies, amplitudes, and temperatures. We gratefully

acknowledge the MagNet database for providing this extensive dataset, which significantly simplified the complex process of data acquisition and initial processing that would otherwise be necessary. The data in the MagNet database are collected using automated systems and standardized procedures, such as the two-winding (voltamperometric) method [91], [92]. Details regarding the hardware setup and data acquisition process used for MagNet are available in [40], [93].

For the initial validation of the MMINN model detailed in this chapter, relevant data is extracted from the MagNet database. The primary material studied is TDK N87 ferrite. The dataset includes dynamic hysteresis responses under various operating conditions, focusing on steady-state, high-frequency, symmetric magnetic flux density excitation waveforms, such as sinusoidal, triangular, and trapezoidal shapes, across frequency ranges of 50-500 kHz, flux density amplitudes of 10-300 mT, and temperatures of 25-90 °C. The total available dataset for N87 ferrite from MagNet is 40616 excitation-response pairs. Each original waveform sequence consists of 1024 discrete sampling points per cycle.

3.4.2 Dataset Split and Data Preprocess

Once the initial dataset is assembled, it undergoes several preprocessing steps before being used for model training. Following the workflow in Figure 3.3, the dataset is first split into training, validation, and testing subsets. This splitting is a common practice to evaluate the model's performance and prevent overfitting. A typical split ratio is 60% for training, 20% for validation, and 20% for testing.

Data preprocessing is essential to ensure that network parameters are learned efficiently and on a similar scale, which helps reduce training complexity and improve model performance. Key preprocessing steps include:

- **Normalization:** Input features (eg., B, $\frac{dB}{dt}$, f, T) are typically normalized to a similar range to prevent features with larger magnitudes from dominating the learning process. Z-score normalization is a common preprocessing technique applied to the input features to standardize their scale and improve training convergence. For a

given feature value v, its normalized value v' is calculated as:

$$v' = \frac{v - \mu}{\sigma}, \tag{3.7}$$

where μ is the mean of the feature across the dataset, and σ is the standard deviation.

- **Outlier Detection and Removal:** Outlier data points, which may arise from measurement errors or rare anomaly operations, can negatively impact model training. Algorithms can be employed to detect and remove these outliers based on criteria such as smoothness analysis or deviation from expected values [45].
- **Waveform Processing and Downsampling:** To optimize the neural network's computational efficiency and ensure model compactness, the original 1024-point magnetic sequences are downsampled to 128 discrete points per cycle using a shape-preserving piecewise cubic Hermite interpolating polynomial (PCHIP) algorithm [94].

  The selection of 128 points as the sampling factor is a deliberate trade-off between signal fidelity and computational cost, supported by recent authoritative studies. According to Serrano et al. [45], fundamental magnetic characteristics such as core loss density (P_v) and amplitude permeability (μ_a) are highly robust against sampling effects. Their findings demonstrate that even a reduction to 64 points does not significantly affect the accuracy of P_v calculation ($< 3\%$), as the flux density B is inherently smoothed through the numerical integration of the induced voltage. Furthermore, the 128-point resolution aligns with the standardized input configuration established in *MagNet-AI* [40] for high-performance magnetic modeling. From a signal processing perspective, 128 points per period provide sufficient bandwidth to resolve harmonics up to the 64th order (Nyquist limit), which is more than adequate to capture the significant spectral energy of the non-sinusoidal waveforms (e.g., triangular and trapezoidal) analyzed in this study.

For the Hysteresis Subnetwork, which utilizes conceptual PI stop operators, the number of these operators, denoted by n. Each operator is parameterized by a threshold r_i. These thresholds are typically initialized by dividing the maximum normalized magnetic field

intensity (typical 1) in the training data evenly according to the index of the operator:

$$r_i = \frac{i}{n}, \tag{3.8}$$

where i is the operator index $(1, 2, ..., n)$. Additionally, for the iterative update of the stop operator state (Equation (3.4) in Section 3.2.1), an initial state for each operator at the beginning of the sequence ($S_r(0)$) must be defined. This initial state is typically set to 0, corresponding to a demagnetized state.

3.4.3 Model Training Process

The training of the MMINN model involves optimizing its internal parameters (weights and biases of the neural networks) by minimizing a defined objective function. To address the engineering demands of both accurate core loss estimation and magnetization process simulation, the training is formulated as a multitask learning problem. The model is trained to perform two primary tasks simultaneously: predicting the magnetic field strength (H) and predicting the core loss density (P_v). The objective function for multitask learning is defined as a weighted sum of the loss functions for each task. Thus, the loss function L is formulated as:

$$L = \lambda_H L_H + \lambda_{P_v} L_{P_v}, \tag{3.9}$$

where L_H is the loss function for the magnetic field prediction task, and L_{P_v} is the loss function for the core loss density prediction task. The loss for the magnetic field prediction task, L_H is defined as the mean square error (MSE) between the predicted field strength (H) and the true measured field strength ($\hat{H}$) over a sequence of N data points:

$$L_H = \frac{1}{N} \sum_{i=1}^{N} (H_i - \hat{H}_i)^2. \tag{3.9a}$$

This loss component primarily quantifies the accuracy of the model in capturing the local characteristics of the magnetic response (the shape of the $\mathbf{B}$–$\mathbf{H}$ loop). The loss for the core loss density prediction task (L_{P_v}) is defined as the mean square error (MSE) of the relative error between the predicted core loss density (P_v) and the true measured core loss density

($\hat{P}_v$):

$$L_{P_v} = (\frac{P_v - \hat{P}_v}{\hat{P}_v})^2. \tag{3.9b}$$

This loss component primarily quantifies the accuracy of the model in simulating the global characteristics of the core loss. By minimizing both L_H and L_{P_v} simultaneously, the multitask learning approach aims to ensure that the model accurately captures both the local details of the magnetic response and the overall energy dissipation, thereby achieving a robust core loss model.

The parameters λ_H and λ_{P_v} are weighting factors that balance the importance of the two tasks during training. Selecting appropriate weights is crucial for effective multitask learning. The Dynamic Weight Average (DWA) technique [95] is a method used to dynamically adjust these task weights during training based on the inverse training progress of each task. The core idea of DWA is to give more weight to tasks that have been learning slower recently, aiming to balance the learning rates across all tasks. The weight for task k (where i can be H or P_v) at training step t is calculated based on the loss values from recent steps (e.g., $t-1$ and $t-2$):

$$\lambda_i(t) = \frac{e^{\frac{w_i(t-1)}{T}}}{\sum_j e^{\frac{w_j(t-1)}{T}}}, \tag{3.10}$$

where $w_i(t-1) = \frac{L_i(t-1)}{L_i(t-2)}$ represents the training progress of task i at step $t-1$ (ratio of loss at $t-2$ to loss at $t-1$), T is a temperature parameter (a hyperparameter controlling the sensitivity of weights to loss ratios), and the sum in the denominator is over all tasks j (H and P_v). DWA thus dynamically increases the weight of tasks that show less recent progress, encouraging balanced learning.

The optimization algorithm used to minimize the objective function plays a crucial role in the training process. The Adam optimizer [96], which combines the benefits of adaptive learning rates and momentum, is a widely used and effective choice for training neural networks.

Early stopping is a technique used to prevent overfitting and determine the appropriate point to terminate training [97]. The performance of the model on the validation dataset is monitored during training. If the objective function on the validation dataset does not show significant improvement (e.g., does not decline) for a certain number of training epochs, the

training process is stopped, and the model parameters from the epoch with the best validation performance are saved.

3.5 Validation Results

This section presents the experimental validation results for the MMINN model, demonstrating its performance in core loss estimation and dynamic hysteresis response prediction under steady-state, high-frequency, symmetric magnetic flux density excitation waveforms. The validation is conducted using a test dataset extracted from the MagNet open-source database [40], [41], [45], specifically focusing on TDK N87 and N49 ferrite materials, consistent with the data preparation described in Section 3.4.1. The performance of the MMINN is evaluated based on key metrics for both magnetic field prediction and core loss estimation, and compared against other neural network models as presented in [40].

3.5.1 Evaluation Metrics

To quantitatively evaluate the performance of the MMINN model, two key metrics are employed, consistent with the analysis presented in [88]. For a given data point, the relative error of core loss is calculated as:

$$RelativeError = \frac{|P_{v,pred} - P_{v,meas}|}{P_{v,meas}} \times 100\%, \tag{3.11}$$

where $P_{v,pred}$ is the predicted core loss density and is the predicted core loss density and $P_{v,meas}$ is the measured core loss density. To provide a comprehensive view of performance across the test dataset, the average relative error, maximum relative error, and the 95th percentile of the relative error (95% PE) are reported. The 95% PE indicates the error value below which 95% of the data points fall, helping to identify potential high-error scenarios

3.5.2 Overall Performance

The MMINN model's performance is first evaluated on the test dataset for N87 ferrite under various steady-state, high-frequency, symmetric excitation waveforms. For the validated the MMINN model, the number of conceptual stop operators (n) in the Hysteresis Subnetwork is 30, and the number of RNN neurons (m) in the Dynamic Subnetwork is 30. Other key hyperparameters, such as the learning rate and learning rate scheduler, were selected as 0.002 and 0.99.

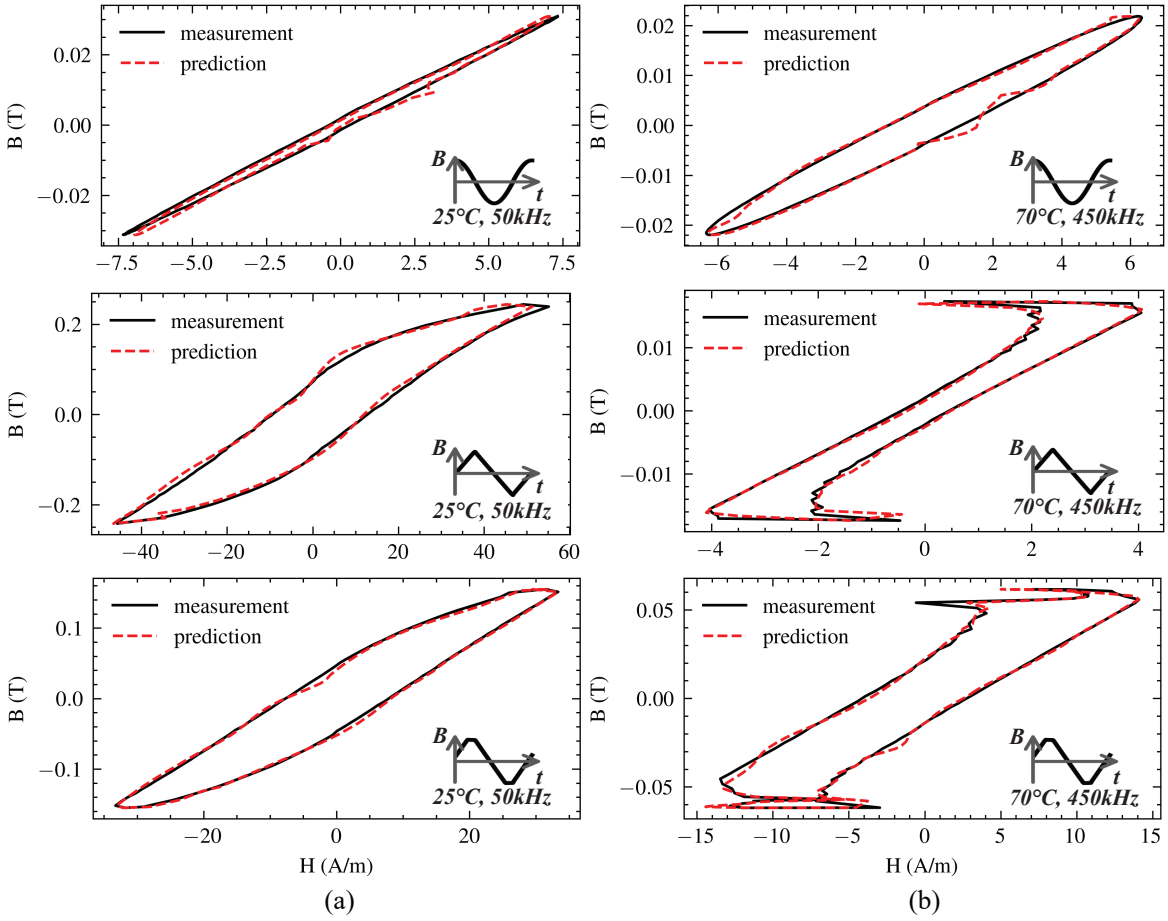

FIGURE 3.4: Measured vs. predicted $\mathbf{B}$–$\mathbf{H}$ loops for the MMINN (N87 ferrite, representative waveforms at (a) 25°C, 50kHz and (b) 70°C, 450kHz)

Figure 3.4 presents examples of measured and predicted $\mathbf{B}$–$\mathbf{H}$ loops for representative steady-state, symmetric excitation waveforms (sinusoidal, triangular and trapezoidal) on N87 ferrite, comparing conditions at different frequencies and temperatures. Specifically, Figure 3.4(a)

shows loops at 25°C and 50 kHz, while Figure 3.4(b) shows loops at 70°C and 450 kHz. Objectively speaking, the measured $\mathbf{B}$–$\mathbf{H}$ loops for these two conditions are noticeably different, with a clear difference in their area (representing core loss) and shape. This significant variation in core loss and $\mathbf{B}$–$\mathbf{H}$ loop characteristics with changes in frequency and temperature highlights the complexity of magnetic material behavior and demonstrates why simple power law equations are insufficient for accurate prediction across varying conditions, thus underscoring the significance of developing more sophisticated models like the MMINN.

Comparing the MMINN predictions to the measured data in Figure 3.4, the model visually shows a good match with the measured $\mathbf{B}$–$\mathbf{H}$ loops across both low-frequency/room temperature and high-frequency/higher temperature conditions, capturing the general shape and area well, although minor discrepancies are visible at local extremum points. It is also observed that the prediction error is slightly larger for sinusoidal magnetic flux density excitations compared to triangular and trapezoidal waveforms. Furthermore, in some instances, the predicted $\mathbf{B}$–$\mathbf{H}$ loops exhibit discontinuous jumps, deviating from the smooth measured curves. These observations are attributed to two main factors. First, the model assumes an initial demagnetized state with zero operator states for the hysteresis subnetwork, which may not be appropriate for magnetic components operating in a steady-state environment, as is the case for the test data. Second, the training data distribution in the MagNet database is uneven; for N87 ferrite, sinusoidal magnetic flux density excitation data comprises only about 4% of the total training set, while the majority consists of triangular and trapezoidal waveforms, leading to a bias in the learned patterns.

For core loss estimation, the MMINN model demonstrates satisfactory accuracy in this scenario. Figure 3.5 shows the distribution histogram of the relative core loss error for the N87 ferrite test dataset. As shown, the majority of predictions fall within a low error range. The average absolute relative core loss error for the N87 test set is 2.16%, with a 95% PE within (-3.7%, 4.6%), and a maximum relative error of 22.36%. These results indicate that the MMINN is well-suited for core loss estimation in this specific application context.

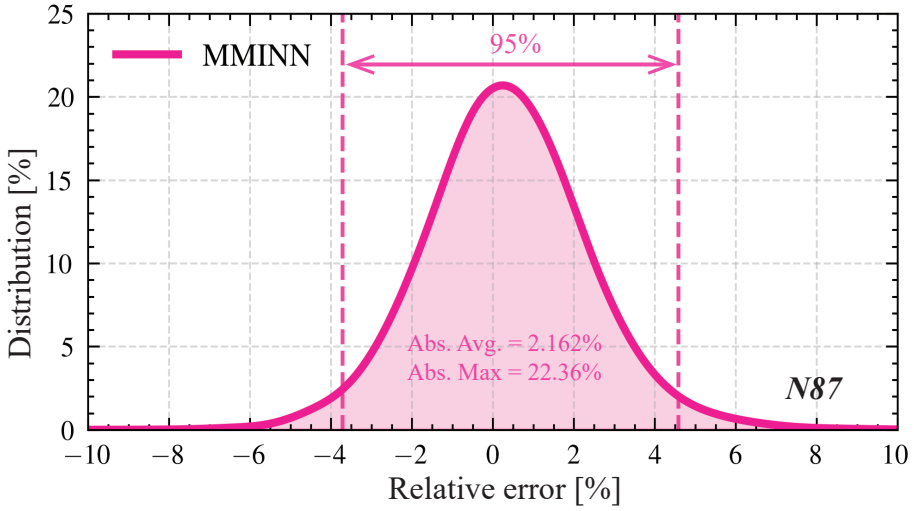

FIGURE 3.5: Histogram of core loss relative error for MMINN (N87 ferrite test set).

3.5.3 Comparison with Other Neural Network Models

To further contextualize the MMINN's performance, it is compared with other existing neural network models for core loss estimation, specifically the transformer-based encoder-decoder model [40] and the LSTM-FNN model [98], as presented in [88]. These models represent different state-of-the-art data-driven or hybrid NN approaches for magnetic modeling. The comparison focuses on model accuracy, speed, memory requirements (model size), and data dependency.

Comparison with Transformer-Based Encoder-Decoder Model:

TABLE 3.2: Comparison of model performance on TDK N49 ferrite

Metric	**Transformer [40]**	**MMINN**
Model parameters	28,481	1,086
Prediction time	4.1 ms	0.2 ms
Avg. abs. error (N49)	13.88%	2.57%
Max abs. error (N49)	184.2%	20.02%
Data required for 13.88% error	5,000	~200
Physical insights	No	Yes

For the comparison of model size, memory requirements, and inference speed, both the MMINN and the transformer-based encoder-decoder model [40]. were trained and evaluated using a dataset of 5000 excitation-response pairs for N49 ferrite from the MagNet database. the MMINN has a simple structure and small memory requirements. The transformer-based model used for comparison has 28481 model parameters. In contrast, the MMINN, built with 30 operators/RNN neurons, only requires 1086 model parameters. This difference in parameter count means that the MMINN's memory requirements are reduced by over 26 times compared to the transformer-based model. The file size of the MMINN model is approximately 7kb. As a result of its smaller size and simpler structure, the MMINN can obtain core losses more rapidly compared to the transformer-based model, achieving an inference speed of 0.2ms versus 4.1ms per 128-step excitation when evaluated on a high-performance laptop (Intel Xeon Gold 5315Y with RTX A5000 GPU). Regarding accuracy for N49 ferrite, the MMINN also demonstrates significant advantages. Table 3.2 summarizes the comparison results for N49 ferrite.

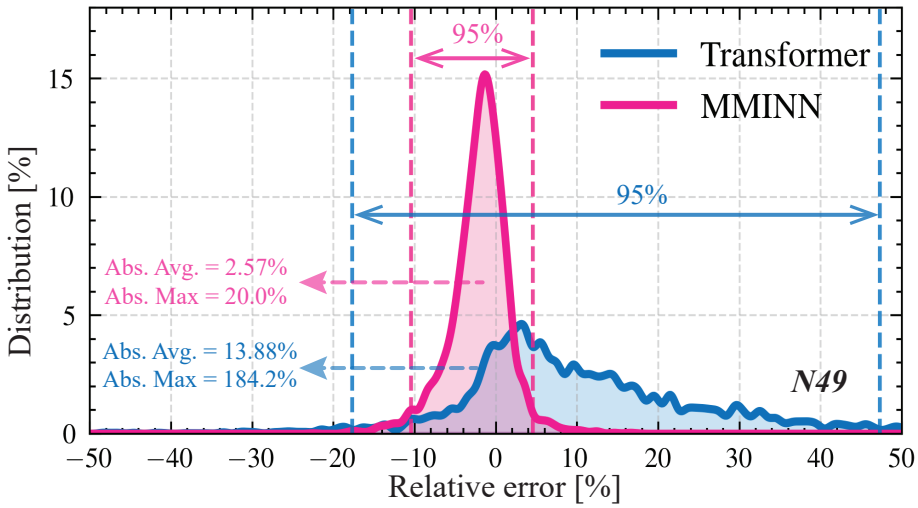

FIGURE 3.6: Histograms comparing core loss relative error distributions (N49 vs Transformer).

Figure 3.6 illustrates the core loss relative error distribution for N49 ferrite, comparing the MMINN with the transformer-based model. As shown, the MMINN model exhibits a significantly narrower error distribution, with both average and maximum errors (2.57% / 20.02%) substantially lower than those of the Transformer model (13.88% / 184.2%).

Comparison with LSTM-FNN Model:

TABLE 3.3: Comparison of model performance on Feroxcube 3C95 ferrite

Metric	LSTM-FNN [98]	MMINN
Model parameters	90,654	1,086
Prediction time	0.13 ms	0.2 ms
Avg. abs. error (3C95)	1.61%	1.81%
Max. abs. error (3C95)	20.93%	21.94%
Data requirement	Extensive	Light
Physical insights	No	Yes

A similar comparison was performed with the LSTM-FNN model [98] using Ferroxcube 3C95 ferrite data from the MagNet database. Table 3.3 summarizes the comparison results for 3C95 ferrite. Table 3.3 outlines the model comparison results in different angles. The primary benefit of the MMINN in this comparison lies in its compact model size, which allows it to achieve comparable prediction performance (average absolute core loss error of 1.81% vs 1.61%) but with much fewer parameters (1086 vs 90654) than the LSTM-FNN model. Consequently, the MMINN model file size is 1/90 of the LSTM-FNN model (7kb vs 361kb), and often requires substantially less computational burden on model training with a smaller parameter search space. the MMINN also demonstrated a lighter dependence on data amount in this experiment, requiring merely 5357 sets of training data. In contrast, the LSTM-FNN model, in this comparison scenario, initially required a large-scale database (comprising over 100,000 sets of data for ten materials from the MagNet database) to build a base model before applying transfer learning to achieve a fine-tuned model.

It is noted that the MMINN model's prediction time (0.2ms) is slightly slower than that of the LSTM-FNN model (0.13ms). This difference is attributed to the nature of their predictions. The LSTM-FNN model is designed as a scalar-to-scalar model that directly outputs the core loss (a single scalar value). In contrast, the MMINN model predicts the dynamic hysteresis $\mathbf{B}$–$\mathbf{H}$ loop (a sequence of H values, effectively a vector prediction) and then calculates the core loss from the loop area. This vector prediction involves iterative calculations within the model architecture. While sacrificing some computational speed for a single prediction, the

MMINN model's capability to predict the full dynamic hysteresis loop provides a wider range of application scenarios, such as real-time core loss prediction based on instantaneous H-B behavior, or the ability to perform magnetic component anomaly detection by analyzing the shape of the predicted **B**–**H** loop.

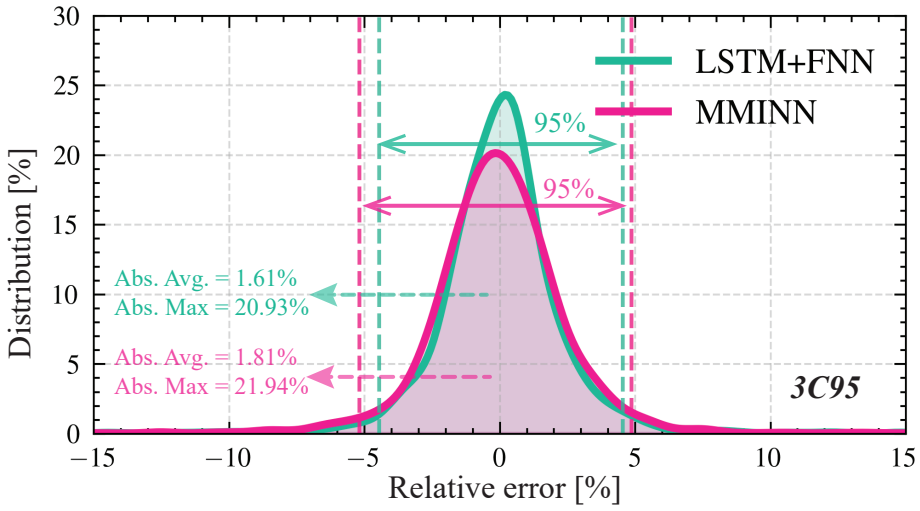

FIGURE 3.7: Histograms comparing core loss relative error distributions (3C95 vs LSTM-FNN).

Figure 3.7 illustrates the core loss relative error distribution for 3C95 ferrite, comparing the MMINN with the LSTM-FNN model. As shown, the MMINN exhibits a comparable error distribution to the LSTM-FNN model, with average and maximum errors of 2.57% / 21.94% versus 1.81% / 21.94%, respectively.

3.5.4 Discussion of Performance Characteristics

The validation results presented in the preceding subsections demonstrate the performance characteristics of the MMINN model in core loss estimation and dynamic hysteresis response prediction under steady-state, high-frequency, symmetric waveforms.

A key advantage highlighted by the comparative analysis (Section 3.5.3) is the MMINN's data efficiency and memory requirements when compared to other neural network models like the transformer-based encoder-decoder model and the LSTM-FNN model. the MMINN was able to achieve comparable or superior accuracy with significantly less training data

and fewer model parameters, resulting in a much smaller memory footprint. This data-light characteristic is particularly valuable for practical applications where acquiring large, comprehensive datasets is costly and time-consuming.

Furthermore, the MMINN demonstrates competitive computational speed for inference, making it suitable for applications requiring fast predictions. While slightly slower than the scalar-output LSTM-FNN model due to its vector prediction nature, it is significantly faster than more complex architectures like the transformer model. The ability to predict the full $\mathbf{B}$–$\mathbf{H}$ loop, despite the minor speed trade-off compared to a scalar model, offers broader utility for tasks beyond simple core loss calculation.

Being inspired by physical magnetizaiton mechanisms (loss separation, PI model, ladder network), the MMINN offers a degree of physical interpretability compared to purely black-box neural networks (Section 2.3.1). The separation into hysteresis and dynamic subnetworks aligns with physical understanding, and the structure within subnetworks is related to physical concepts. This interpretability can provide some insights into the model's behavior and potentially guide future improvements, although it does not provide the full physical insight of a first-principles model. As noted in [88], [89], while some fully data-driven models might achieve high accuracy through sophisticated feature engineering, they often lack this physical interpretability.

The observed prediction artifacts, such as slightly larger errors for sinusoidal waves and occasional discontinuous jumps (Section 3.5.3), suggest areas for potential improvement, likely related to the model's initial state assumption for steady-state data and the uneven distribution of training data types. However, overall, the MMINN demonstrates satisfactory accuracy for the targeted application scenario.

3.6 Discussion and Summary

This section summarizes the key findings from the experimental validation of the MMINN model presented in Section 3.5.

The initial validation of the MMINN model using the MagNet database for TDK N87, N49, and Ferroxcube 3C95 ferrite materials under steady-state, high-frequency, symmetric waveforms confirms its effectiveness for this specific application scenario. The MMINN achieves satisfactory accuracy in both magnetic field prediction (reflected in the visual match of $\mathbf{B}$–$\mathbf{H}$ loops) and core loss estimation. For the N87 ferrite test set, the average absolute relative core loss error is 2.16%, and the absolute relative error lies within the range of -3.7% to 4.6% for 95% of the samples. These error levels are well within typical engineering requirements (e.g., often below 5% or 10%).

Comparative analysis with other neural network models (transformer-based and LSTM-FNN) demonstrates the MMINN's significant advantages in terms of data efficiency, requiring substantially less training data for comparable accuracy. It also exhibits superior computational efficiency regarding memory requirements and prediction speed compared to the transformer-based model, and comparable speed/accuracy with significantly lower memory compared to the LSTM-FNN model.

Furthermore, the MMINN offers a degree of physical interpretability due to its mechanism-inspired architecture. These results highlight MMINN's potential as a practical and efficient hybrid modeling tool for core loss estimation and dynamic hysteresis response prediction in scenarios involving steady-state, high-frequency, symmetric excitations, particularly where data and computational resources are limited.

However, despite the MMINN demonstrating the viability of physics-inspired neural structures, its simplified hysteresis modeling and lack of explicit memory mechanisms limited its ability to accurately capture complex, history-dependent phenomena. Specifically, its performance significantly degraded under non-symmetric excitation waveforms, such as those with DC bias or intricate minor loops, which are prevalent in real-world power electronic applications. This crucial limitation, underscoring the need for a more fundamental and general material model capable of handling arbitrary quasi-static excitations, directly motivated the subsequent development of the History-Dependent Prandtl-Ishlinskii Neural Network (HDPI-NN) in Chapter 4.

CHAPTER 4

History-Dependent Prandtl-Ishlinskii Neural Network (HDPI-NN)

This chapter introduces the HDPI-NN, the second hybrid modeling strategy explored in this thesis. Building upon the foundational concepts and the initial exploration of hybrid physics-neural network approaches presented in Chapter 3, the HDPI-NN is developed to address specific limitations encountered when modeling magnetic material behavior under more complex and arbitrary operating conditions.

4.1 Introduction and Motivation

The accurate and generalizable modeling of magnetic core losses is a critical endeavor for advancing the design of modern high-performance power electronic systems. As power electronic devices operate under increasingly demanding conditions, characterized by complex, non-linear material behaviors and diverse excitation waveforms that deviate significantly from common waveform patterns, the need for precise predictive models becomes paramount. These demanding conditions include the presence of DC bias, high-order harmonics, and the generation of intricate minor loops, all of which introduce significant history-dependent effects into the magnetization process. These effects are crucial to capture for accurate performance prediction, as they directly influence the energy dissipation and overall efficiency of magnetic components under realistic operating scenarios, such as during converter startup, shutdown, or when subjected to non-ideal control signals.

The MMINN, developed in Chapter 3, represented a significant step towards hybrid physics-neural network approaches. the MMINN was initially validated on a subset of the MagNet dataset focusing on steady-state, high-frequency, symmetric excitation waveforms, including sinusoidal, triangular, and trapezoidal shapes. For these common conditions, the MMINN demonstrated satisfactory accuracy in predicting both the $\mathbf{B}$–$\mathbf{H}$ loops and core loss. For instance, the average absolute relative core loss error on the N87 ferrite test set for these symmetric waveforms was found to be around 2.16%, with a 95% PE within (-3.7%, 4.6%). However, while the MMINN achieved reasonable performance for these specific scenarios,

its ability to generalize to more complex excitations, such as those involving DC bias or significant harmonic content, was limited. This limitation, stemming from its simplified hysteresis modeling, underscored the need for a more sophisticated material model capable of accurately capturing intricate hysteresis phenomena, including memory effects and reversible magnetization dynamics, under a wider range of quasi-static conditions.

This limitation underscores the need for a more sophisticated material model that can accurately represent the intrinsic hysteresis behavior of magnetic materials, including their memory effects and the nuanced interplay of reversible and irreversible magnetization processes under a wider range of quasi-static conditions. The challenge lies in developing a model that is not only accurate but also generalizable across a broad spectrum of excitation waveforms, thereby reducing the reliance on extensive material characterization for every new operating scenario. Such a model is essential for bridging the gap between simplified physics-based approaches and purely data-driven methods, offering a pathway to achieve both high accuracy and data efficiency in material characterization.

To address these specific challenges, our research focuses on enhancing the modeling of the hysteresis component, which is fundamental to understanding and predicting core losses under complex conditions. Building upon the insights gained from the MMINN and the review of existing hysteresis models in Chapter 2, we propose a novel approach, the HDPI-NN [99], that integrates the strengths of operator-based models with advanced neural network capabilities. Our core idea is to improve the fundamental hysteresis operator by incorporating more comprehensive physical mechanisms, such as the reversible magnetization components inspired by the Jiles-Atherton (J-A) model [24], [26]. This forms an enhanced hysteresis operator framework that is then parameterized and learned by a neural network. By leveraging the advanced pattern recognition and learning capabilities of neural networks, this approach aims to directly capture the complex, history-dependent $\mathbf{B}$–$\mathbf{H}$ behavior, including the effects of DC bias and minor loops, without the need for complex analytical parameter identification. This allows for a more accurate and generalizable prediction of core loss across a wider range of arbitrary quasi-static excitation types.

The subsequent sections of this chapter will detail the architecture of the HDPI-NN model, explaining how it incorporates these history-dependent mechanisms and reversible magnetization through its generalized operator framework. It will then describe the model's implementation, the training methodology employed to optimize its parameters, and the experimental setup used for data acquisition and validation. Finally, the chapter will present the validation results, demonstrating the HDPI-NN's superior accuracy and generality in modeling magnetic material behavior under complex quasi-static conditions compared to MMINN and other existing approaches, and highlighting its data efficiency. This work establishes the HDPI-NN as a crucial, advanced material model that will be integrated into the scalable physics-based solver in Chapter 5 to achieve accurate, general, and scalable core loss prediction across a wider range of conditions.

4.2 Generalized Stop Operator

The development of accurate and generalizable models for magnetic materials under arbitrary excitation waveforms is a significant challenge. As discussed in Chapters 2 and 3, while hybrid physics-neural network approaches offer a promising direction, the fidelity of the material model within these frameworks is paramount. The MMINN model, which utilized a hysteresis subnetwork based on the classical Prandtl-Ishlinskii (PI) model, demonstrated the feasibility of embedding operator-based concepts within a neural network for magnetic hysteresis modeling. This approach showed that neural networks can effectively learn the distribution and contributions of operators, bypassing some of the challenges associated with traditional parameter identification methods.

However, the experience with the MMINN also highlighted the inherent limitations of the classical PI model when applied to more complex scenarios. These limitations, which were also identified in the literature review (Section 2.2.3), include:

- **Parameter Identification Complexity:** Traditional PI models require the identification of an operator distribution function (μ_r). This process is often challenging, time-consuming, and relies on empirical assumptions about the distribution's form

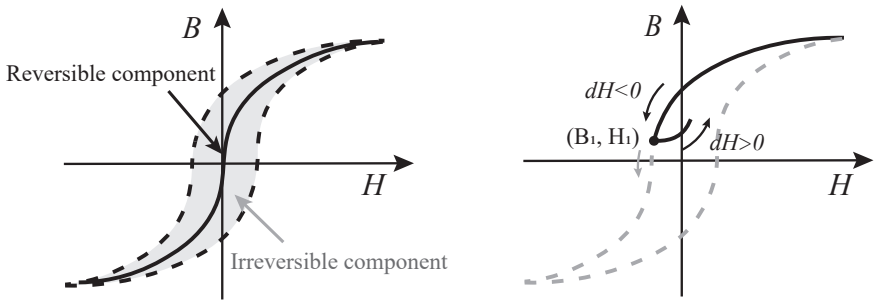

(a) Reversible magnetization (b) Historical dependency

FIGURE 4.1: Key mechanisms of magnetization process simulation: (a) Reversible Magnetization and (b) Historical Dependency.

(e.g., Gaussian [100]), which may not accurately reflect the material's true behavior. This complexity can lead to suboptimal parameter sets and limit the model's predictive accuracy, especially when trying to generalize across different materials or complex excitation conditions.

- **Incomplete Magnetization Mechanisms:** Classical PI operators tend to oversimplify the magnetization process, particularly the reversible magnetization component. They may not fully capture the gradual, continuous nature of domain wall bending or the subtle reversible domain wall movements that are critical for accurately representing minor loops and the overall $\mathbf{B}$–$\mathbf{H}$ curve shape. As illustrated in Figure 4.1(a), which conceptually depicts the reversible and irreversible components of magnetization, classical PI models often struggle to precisely model the reversible part.
- **Lack of Explicit Memory Mechanism:** The classical PI model's ability to capture history dependence is often achieved through assumptions about the distribution of its operators. However, these assumptions may not fully represent the material's true memory effect, where the magnetization state is critically dependent on the most recent reversal point or extremum. This deficiency becomes particularly apparent under DC bias or complex excitation sequences involving repeated minor loops, where the magnetization path is not simply dictated by the current instantaneous field but by its past trajectory. Figure 4.1(b) conceptually illustrates this historical

dependency, showing how the magnetization path is influenced by previous states and reversal points [23], [25].

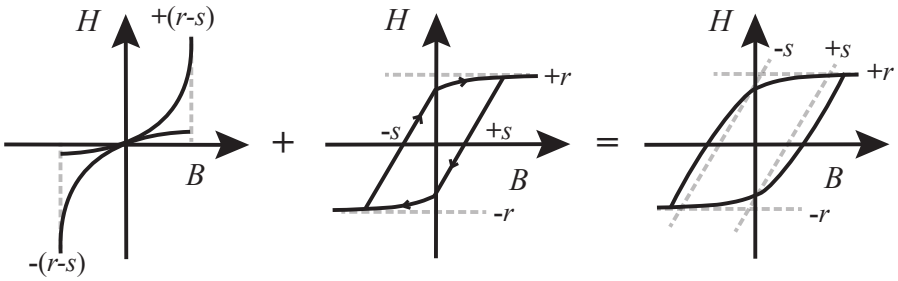

(a) Reversible Component (b) Irreversible Component (c) Generalized Stop Operator

FIGURE 4.2: Conceptualization of the Improved PI Hysteresis Operator: (a) Reversible Magnetization Component, (b) Irreversible Magnetization Component and (c) Generalized Stop Operator.

These limitations, inherited by the MMINN's hysteresis subnetwork, underscore the necessity for a more robust and physically grounded hysteresis model. To overcome these issues, we propose the Generalized Stop Operator. This improved operator is designed to explicitly incorporate the necessary physical mechanisms that are lacking or simplified in the classical PI model:

1. **Integration of Reversible Magnetization:** Inspired by models like the Jiles-Atherton (J-A) model [12], [24], [26], the Generalized Stop Operator explicitly accounts for the reversible component of magnetization.The J-A model describes the magnetization process by separating it into reversible (M_{rev}) and irreversible (M_{irr}) components, where the total magnetization (M) is $M = M_{rev} + M_{irr}$. Crucially, M_{rev} is associated with the global equilibrium state of anhysteretic magnetization (M_{an}), which represents the ideal reversible magnetization in the absence of hysteresis:

$$M_{rev} = c(M_{an} - M_{irr}), \tag{4.1}$$

where c is a domain flexing parameter. This anhysteretic magnetization can often be approximated by a Langevin function, which depends on the effective magnetic field

and material properties, and can be expressed as:

$$M_{an} = M_{sat}(coth(\frac{H_e}{a}) - \frac{a}{H_e}), \tag{4.2}$$

where M_{sat} is the saturation magnetization, H_e is the effective magnetic field, and a is a coupling parameter. As a consequence, the reversible magnetization component can be illustrated in the piece-wise single-valued form [99], [101], which is amenable to neural network modeling. By incorporating such a formulation, the Generalized Stop Operator aims to provide a more accurate representation of the gradual, continuous changes in magnetization that occur before irreversible domain wall motion or rotation. Figure 4.2(a) conceptually illustrates the contribution of the reversible component to the overall hysteresis loop. From a mathematical perspective, the presence of the a/H_e term in the Langevin function indicates that reciprocal relationships are intrinsic to the physics of reversible magnetization. This suggests that providing reciprocal features to a neural network can significantly simplify the task of learning the asymptotic behavior of the magnetization curve near saturation.

2. **Incorporate historical dependencies:** A critical aspect of accurately modeling magnetic hysteresis, especially under complex excitations like DC bias and minor loops, is the material's memory effect. Traditional PI models, as discussed, often lack explicit mechanisms to capture this path dependence. To address this, the Generalized Stop Operator includes mechanisms to retain and utilize information about the most recent reversal points and the overall magnetization history. This is achieved through techniques that can be inspired by the way the Preisach model handles history. In the Preisach model, the concept of a Preisach plane is used to represent the distribution of elementary hysterons, and the model's state is updated based on tracking when the applied field crosses the switching thresholds of these hysterons, effectively creating a memory stack of previous states and reversal points [27], [65]. Similarly, the Generalized Stop Operator incorporates a mechanism to store and utilize this critical historical information. By feeding the model with information about the most recent reversal points and past states, the operator's output becomes path-dependent, ensuring that the model's predictions accurately

reflect the material's memory effects. As conceptually illustrated in Figure 4.2(b), the modified irreversible magnetization component, which incorporates these memory effects, deviates from the simplistic, abrupt transitions of classical PI operators (see Figure 2.6(a)). It can be observed that in the region where the domain wall motion is significant, the $\mathbf{B}$–$\mathbf{H}$ loop does not exhibit a single, sudden slope change. Instead, it demonstrates a more gradual and continuous evolution, reflecting that the irreversible energy dissipation does not occur abruptly in a single form. This more nuanced representation leads to a more accurate prediction of the overall hysteresis loop, as shown in Figure 4.2(c).

It is important to note that while the conceptual framework of the Generalized Stop Operator draws inspiration from physics-based models, certain parameters within the operator, such as the shape factor 's' and operator distribution, cannot be directly and quantitatively expressed via analytical formulas. These parameters are intrinsically linked to the material's microstructural properties and the complex interplay of domain dynamics. Therefore, they must be inferred from experimental data. This is where data-driven models come into play, enabling the neural network to learn these crucial parameters from the measured $\mathbf{B}$–$\mathbf{H}$ loops and operating conditions. By embedding the improved operator within a neural network, we can effectively learn these data-dependent parameters, thereby achieving a more accurate and generalizable model.

4.3 HDPI-NN Model Architecture

Building upon the foundation of the Generalized Stop Operator and the insights gained from the MMINN, this section details the architecture of the HDPI-NN. The HDPI-NN is designed to leverage the strengths of both physics-inspired modeling and data-driven learning to accurately capture the complex, history-dependent magnetic material behavior under arbitrary quasi-static excitation waveforms.

The overall architecture of the HDPI-NN model is illustrated in 4.3, which reflects the physical decomposition of the magnetic field strength (H) into its reversible (H_{rev}) and irreversible

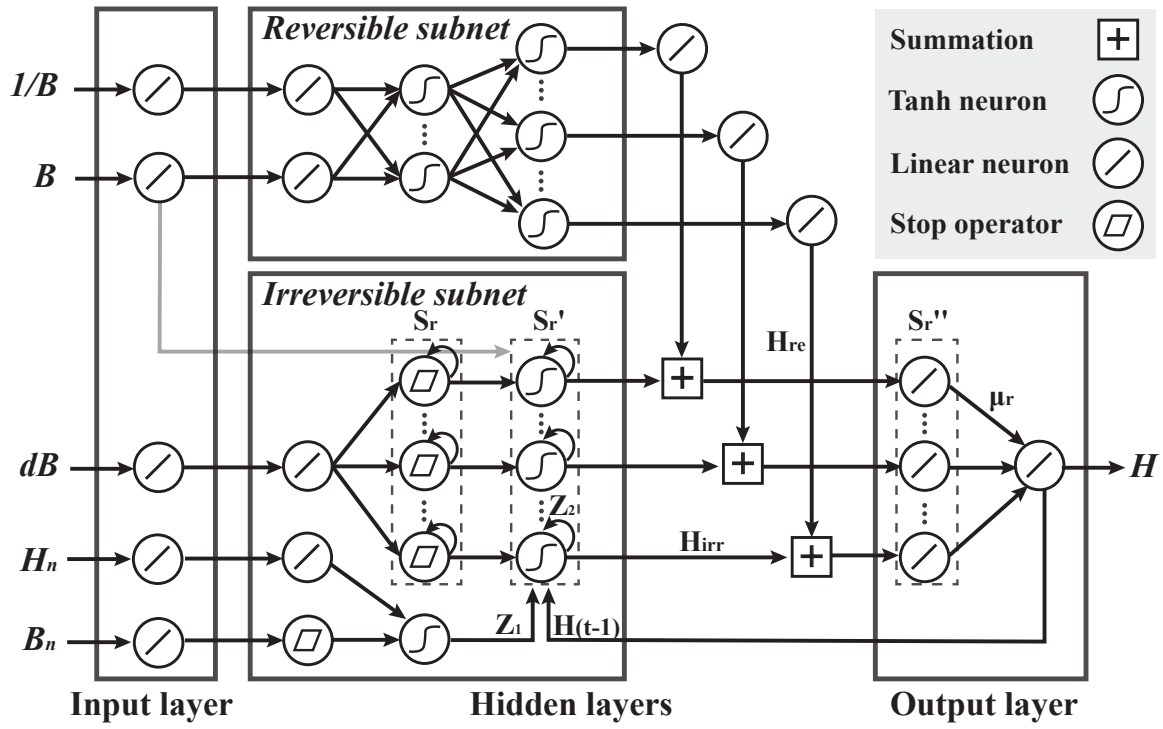

FIGURE 4.3: History-dependent PI core loss hybrid model architecture.

(H_{irr}) components, as represented by the improved hysteresis operator. The model takes magnetic flux density $B(t)$, its time derivative dB/dt and crucially, historical information (e.g., previous $H(t-1)$, and reversal points (H_n, B_n)) as inputs. The neural network then predicts the corresponding magnetic field strength $H(t)$ by processing these inputs through its specialized layers.

The HDPI-NN architecture is broadly divided into the following key components:

- **Input Layer:** Processes the raw input features, including $B(t)$, dB/dt, $H(t-1)$ and recent reversal points (H_n, B_n). Additionally, a reciprocal feature $1/B(t)$ is introduced as a targeted input for the reversible subnetwork. This feature is directly inspired by the $1/x$ term in the Langevin function (Equation 4.2). By explicitly providing $1/B(t)$, the model can more accurately capture the highly non-linear, asymptotic transition into the magnetic saturation region, which is often challenging for standard neural network layers to approximate using only linear or polynomial-like features. Each input feature is typically passed through a linear transformation

layer (represented by the circles with diagonal lines in the figure) to prepare it for the subsequent neural network layers.

- **Hidden Layers:** This is where the core processing of the improved hysteresis operator occurs. It is structured into two main subnetworks:
  - **Reversible Subnetwork:** A dedicated neural network component designed to model the reversible magnetization component (H_{rev}). This subnetwork is structured to learn the smooth, path-independent (or weakly path-dependent) relationship between B and H, potentially inspired by functions like the Langevin function or other smooth mappings representing reversible domain wall bending. It typically consists of several layers of Tanh neurons to capture the non-linear mapping.
  - **Irreversible Subnetwork:** Another neural network component focused on modeling the irreversible magnetization component (H_{irr}). This subnetwork is designed to incorporate the memory mechanisms and history dependence of the material. It builds upon the concept of the Generalized Stop Operator, which enhances the classical Stop Operator (S_r) by explicitly integrating historical information. While traditional PI models utilize S_r to represent discrete state transitions, the improved irreversible component operator (S'_r) within the HDPI-NN is designed to capture these transitions while being influenced by the magnetization history. This is achieved through recurrent connections (indicated by the arrows looping back to the input of subsequent layers, labeled as Z_1 and $H(t-1)$) to maintain the magnetization history.
- **Output Layers:** The outputs from the reversible and irreversible subnetworks are combined, typically through summation (indicated by the '+' symbols), to produce the final predicted magnetic field strength $H(t)$. The final output layer may also involve further processing with linear neurons, to produce the final H value, whose weight (μ_r) represent the distribution of the generalized operators (S''_r) within the material.

The overall workflow of the HDPI-NN model, from input processing to output prediction, can be summarized by Algorithm 1, which highlights the iterative computation over a discrete

sequence of length n and incorporates n_s operators to capture the underlying magnetization dynamics and hysteresis effects through the integration of historical states.

Algorithm 1 The HDPI-NN Inference Procedure

Input: Flux Density $B(t)$
Output: Field Strength $H(t)$

Initialize reversal point (H_n, B_n)
Initialize initial magnetization $(H(t_0), B(t_0))$
Initialize hidden state $S'_r(t_0)$
for $i = 1$ to n **do**
    $dB(t_i) \leftarrow B(t_i) - B(t_{i-1})$
    if $\text{sign}((H(t_i) - H(t_{i-1})) \cdot (H(t_i) - H_n)) < 0$ **then**
        $(H_n, B_n) \leftarrow (H(t_i), B(t_i))$
    end if ▷ Input layer
    $H_{\text{re}}(t_i) \leftarrow \text{FNN}_{\text{rev}}(B(t_i), 1/B(t_i)$ ▷ Reversible branch
    for $j = 1$ to n_s **do**
        $S_j(t_i) \leftarrow \text{SSLU}(dB(t_i), r)$
        $z_{1j}(t_i) \leftarrow f_h(\text{SSLU}(B_n, r), H_n)$
        $z_{2j}(t_i) \leftarrow f_h(S'_j(t_{i-1}), H_n)$
        $S'_{r_j}(t_i) \leftarrow \text{FNN}_{\text{irr}}(z_{1j}(t_i), z_{2j}(t_i), H(t_{i-1}))$
        $H_{\text{irr}}(t_i) \leftarrow S'_{r_j}(t_i)$
    end for ▷ Irreversible branch
    $S''_r(t_i) \leftarrow H_{\text{re}}(t_i) + H_{\text{irr}}(t_i)$
    $H(t_i) \leftarrow \text{FNN}_{\text{out}}(S''_r(t_i))$ ▷ Output layer
end for
return $H(t) = \{H(t_1), H(t_2), \ldots, H(t_n)\}$

4.4 Model Implementation and Training

The development and validation of the HDPI-NN model involve a systematic process, encompassing model implementation, data preparation, and the training of the neural network. This section outlines the practical steps taken to realize the HDPI-NN for accurate and generalizable hysteresis and core loss prediction.

4.4.1 Data Preparation and Feature Engineering

The foundation of any data-driven or hybrid model lies in the quality and quantity of the data used for training and validation. For the HDPI-NN model, dynamic magnetization data, specifically $\mathbf{B}$–$\mathbf{H}$ loops and associated core loss measurements under various excitation waveforms, are required. As discussed in Section 4.1 and 4.2, the model is designed to handle arbitrary quasi-static excitations, including those with DC bias and complex minor loops. Therefore, the dataset needs to reflect this diversity.

The experimental data used for training and validation in this study was acquired using a specialized setup, as described in Section 4.5. This setup allowed for controlled application of excitation waveforms, including sinusoidal, triangular, and trapezoidal shapes, as well as those with DC bias and harmonic content. The data acquisition process involved measuring voltage and current signals to reconstruct the $\mathbf{B}$–$\mathbf{H}$ loops and calculate the corresponding core loss density. This conversion process follows standard magnetic characterization protocols (e.g., IEC 60404) and is governed by fundamental electromagnetic principles derived from Maxwell's equations.

Key data preparation steps include:

- **Data Collection:** Measurements were performed on representative magnetic materials, such as silicon steel B35A270 and ferrite N87, across a range of excitation conditions relevant to the model's intended application. This included varying magnetic field strengths, frequencies (within the quasi-static regime), and temperatures, with a specific focus on waveforms that induce DC bias and minor loops.
- **Feature Extraction and Physical Mapping:** From the acquired voltage and current signals, the magnetic flux density $B(t)$ and magnetic field strength $H(t)$ were derived. According to Ampere's Circuital Law, $H(t)$ is determined by Ampere's Law, considering the current in the excitation winding (i_p) and the effective magnetic path length (l_e):

$$H(t) = \frac{N_p i_p(t)}{l_e}, \tag{4.3}$$

where N_p is the number of turns in the excitation winding. Based on Faraday's Law of Induction, $B(t)$ is derived from the voltage induced in the sensing winding (v_s) via Faraday's Law of Induction:

$$B(t) = \frac{1}{N_s A_e} \int_0^t v_s(\tau) d\tau, \tag{4.4}$$

where N_s is the number of turns in the sensing winding and A_e is the effective cross-sectional area.

To ensure the model accurately captures complex excitations, specific features were engineered to account for **DC bias and harmonics**:

(1) **DC Bias Handling:** Historical information, including the previous magnetic field strength $H(t-1)$ and the most recent reversal points (B_n, H_n), was computed. Physically, these serve as "memory anchors" that allow the neural network to identify the asymmetry of the $\mathbf{B}$–$\mathbf{H}$ loop and the shift in the operating point caused by DC bias.

(2) **Harmonic Content Handling:** The time derivative of flux density (dB/dt) was included as a primary input to capture the instantaneous rate of change associated with high-order harmonics. When combined with the recursive architecture of the Generalized Stop Operator, these features enable the model to track and quantify the energy dissipation of the resulting minor loops.

- **Core Loss Calculation:** The core loss density (P_v) for each measured $\mathbf{B}$–$\mathbf{H}$ loop is calculated by integrating the area enclosed by the loop, which represents the energy dissipated per unit volume per cycle. This is performed by integrating H with respect to B:

$$P_v = \frac{1}{T} \int H dB, \tag{4.5}$$

where T is the period of the excitation waveform. This calculated core loss serves as the target output for the loss prediction task during model training and validation.

- **Data Normalization:** To ensure efficient training and prevent features with larger magnitudes from dominating the learning process, all input features were normalized. Instead of Z-score normalization, which standardizes features based on their mean and standard deviation and lacks direct physical interpretation in this context, we

employ normalization based on the material's saturation characteristics. For B and H, we utilize their respective maximum or saturation values (B_{sat} and H_{sat}) as the normalization factor. This approach treats the instantaneous values as relative states within the material's operational limits, providing a more physically grounded representation. The normalized values B' and H' are calculated as:

$$B' = \frac{B}{B_{sat}}$$
$$H' = \frac{H}{H_{sat}}$$

where B_{sat} and H_{sat} are the saturation values for the specific magnetic material. This normalization helps the neural network learn the intrinsic magnetic behavior independent of the absolute scale of the applied fields, improving its ability to generalize and interpret the physical meaning of the input features.

- **Dataset Splitting:** The prepared dataset was divided into training, validation, and testing subsets. Specifically, 20% of the training set was randomly selected and used as a validation set for hyperparameter tuning and early stopping. In contrast, the testing set was collected through a separate set of experiments using entirely different excitation waveforms, ensuring that the model is evaluated on truly unseen data. This provides a robust and unbiased assessment of its generalization capability. Further details regarding the testing data design and waveform diversity are discussed in Section 4.5.2.
- **Waveform Processing:** Depending on the sampling rate of the acquired data and the computational constraints, sequences need be downsampled to a fixed number of points per cycle (e.g., 128 points) using shape-preserving interpolation techniques to create a consistent input format for the neural network. This can reduce the difficulty of model training and make the model compact.

Through this feature engineering strategy, the physical complexities of DC bias and harmonics are directly embedded into the input space, allowing the HDPI-NN to learn non-linear magnetization paths that traditional models often fail to represent.

4.4.2 Model Training

The training of the HDPI-NN model involves optimizing its internal parameters (weights and biases of the neural networks) by minimizing a defined objective function. Although the main focus of this model is to get accurate prediction for core loss density P_v, it is also essential to make the H prediction correct at each moment. Therefore, the objective function (L) is formulated as a weighted sum of the loss functions for each task:

$$L = \lambda_H L_H + \lambda_{P_v} L_{P_v}, \tag{4.6}$$

where L_H represents the loss for magnetic field prediction and L_{P_v} represents the loss for core loss prediction.

- **Magnetic Field Prediction Loss (L_H):** This loss quantifies the accuracy of the model in capturing the $\mathbf{B}$–$\mathbf{H}$ loop shape and dynamic behavior. It is typically defined as the Mean Squared Error (MSE) between the predicted magnetic field strength sequence (H_{pred}) and the measured sequence ($H_{meas}(t)$):

  $$L_H = \frac{1}{N}\sum_{i=1}^{N}(H_{meas}(t_i) - H_{pred})^2, \tag{4.7}$$

  where N is the number of data points in the sequence. This loss component directly penalizes deviations in the predicted $\mathbf{B}$–$\mathbf{H}$ loop trajectory.
- **Core Loss Prediction Loss (L_{P_v}):** This loss quantifies the accuracy of the predicted core loss. The core loss is calculated from the area enclosed by the predicted $\mathbf{B}$–$\mathbf{H}$ loop. The loss function is typically defined as the MSE of the relative error between the predicted core loss density ($P_{v,pred}$) and the measured core loss density ($P_{v,meas}$):

  $$L_{P_v} = (\frac{P_{v,meas} - P_{v,pred}}{P_{v,meas}})^2. \tag{4.8}$$

  This loss component focuses on the global energy dissipation accuracy.

The weighting factors λ_H and λ_{P_v} are crucial for balancing the learning process between the two tasks. These weights can be fixed or dynamically adjusted during training using techniques like Dynamic Weight Average (DWA) [95] to ensure a balanced convergence.

The performance and generalization ability of the HDPI-NN model are significantly influenced by its hyperparameters. These include the number of operators (n_s) and the number of neurons in the reversible subnetwork, which define the model's capacity. Other crucial hyperparameters for the training process include the learning rate (l_s), batch size (n_b), and the number of training epochs (n_{epo}).

To determine optimal hyperparameter values, we employed a systematic search strategy. For the benchmark HDPI-NN model, hyperparameter optimization was performed using a grid search approach, exploring various combinations of parameters within predefined ranges. The search settings are summarized in Table 4.1. Specifically, the number of operators was explored within the range of [10, 10, 40], with 30 selected as the optimal value. The number of neurons in the reversible subnetwork was set to 5, with a search range of [1, 2, 10]. The learning rate was explored across 0.01, 0.05, 0.1, 0.2, with 0.1 chosen for training. A batch size of 128 was found to provide a good balance between computational efficiency and convergence. The number of epochs was set to 2000, with early stopping [97] employed to terminate training when validation performance plateaued.

TABLE 4.1: Hyperparameter Search Settings

Description	Symbol	Search Range	Selected Value
Number of operators	n_s	[10, 10, 40]	30
Reversible subnetwork neurons	n_{rev}	[1, 2, 10]	5
Learning rate	l_r	{0.01, 0.05, 0.1, 0.2}	0.1
Batch size	n_b	[64, 64, 256]	128
Number of epochs	n_{epo}	–	2000

The optimization process utilizes an algorithm such as Adam [96], which combines adaptive learning rates and momentum to efficiently minimize the objective function. The careful implementation of these training steps, along with the architectural design of the neural networks within the reversible and irreversible subnetworks (incorporating the Generalized Stop Operator), is crucial for achieving accurate and generalizable predictions for complex magnetic material behaviors.

4.5 Experimental Setup and Data Preparation

This section details the experimental setup employed for acquiring the necessary magnetic material data and outlines the organization of the collected data for validating the HDPI-NN model. To rigorously evaluate the model's cross-material generality and its ability to capture the nuances of different magnetic behaviors, we focused on testing two distinct classes of soft magnetic materials commonly used in power electronics:

- **Silicon Steel:** Widely utilized in applications requiring high magnetic flux density and good performance at moderate frequencies, silicon steel serves as a representative material for validating the model's response to various excitation waveforms, including those with DC bias and harmonics.
- **Ferrite:** Prevalent in high-frequency applications due to its low core losses and high permeability at elevated frequencies, ferrite materials present a different set of magnetic characteristics. Testing with ferrite allows us to assess the model's adaptability to materials with distinct microstructures and magnetization processes, further validating its generalizability.

The experimental procedures were designed to generate comprehensive datasets that capture the material's behavior under a range of conditions, including those with DC bias and complex harmonic excitations, which are crucial for testing the model's generality and history-dependent capabilities.

4.5.1 Experimental Setup

The magnetic material characterization was performed using specialized experimental setups tailored to the material type and the desired measurement conditions, aiming to rigorously evaluate the HDPI-NN model's generality and history-dependent capabilities.

- **Silicon Steel Characterization using a Single Sheet Tester (SST):** For silicon steel samples (e.g., B35A270), a double yoke single sheet tester (SST) was utilized (see Figure 4.4). The SST is a standard apparatus for characterizing magnetic

materials under controlled conditions, allowing for precise application of excitation waveforms and accurate measurement of B and H. The SST setup employed in this study featured:

- **Material Samples and Geometry:** Standardized silicon steel samples (B35A270) with specified dimensions (e.g., 100 mm by 600 mm specimen size) and magnetic path length ($l_e = 500mm$) were used.
- **Winding Configuration:** The SST incorporated two sets of windings for different frequency ranges. For low-frequency measurements, the exciting winding had 189 turns, and the sensing winding comprised 199 turns.
- **Excitation and Control:** The setup was equipped with both AC and DC power sources, enabling the application of various magnetic field conditions including pure AC sinusoidal excitations, excitations with superimposed harmonics, and excitations with a DC bias. A feedback control algorithm ensured accurate waveform generation and synchronization.
- **Measurement Instrumentation:** Induced voltage and excitation current were measured using high-bandwidth instrumentation, specifically a voltage probe (e.g., Micsig DP1500) and a 1 ohm shunt resistor, recorded by a Tektronix MSO44B oscilloscope.

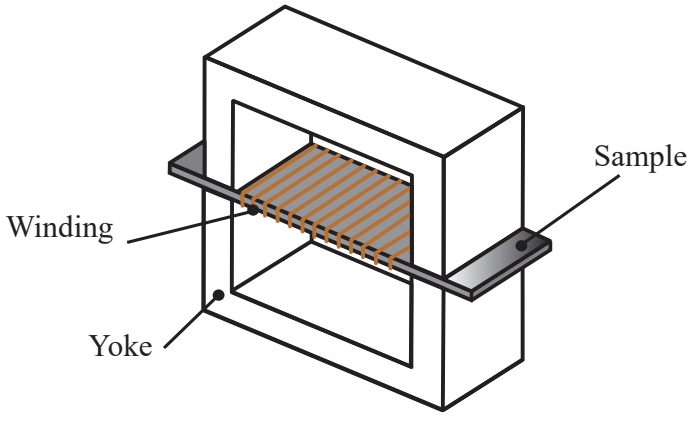

FIGURE 4.4: Schematic of the Single Sheet Tester (SST) Setup.

- **Ferrite Characterization using a Two-Winding Method:** For ferrite materials (e.g., TDK N87 toroidal cores), a two-winding method was employed [91]–[93],

directly measuring the voltage and current of the device under test (DUT). This approach is suitable for toroidal cores and allows for direct acquisition of signals for $\mathbf{B}$–$\mathbf{H}$ loop reconstruction and core loss calculation. The experimental setup included:

- **Material Samples:** The TDK N87 TX12.7/7.9/6.35 toroidal core was used.
- **Excitation and DC Bias Injection:** A function generator produced AC excitation waveforms, a DC power supply provided the bias, and a power amplifier drove the magnetic core samples. Crucially, a DC-bias injection circuit with a mirror transformer was implemented to allow for controlled superposition of a DC bias onto the excitation waveform, enabling the measurement of magnetization data under biased conditions. This method is essential for testing the HDPI-NN's ability to handle asymmetric $\mathbf{B}$–$\mathbf{H}$ loops and shifted operating points, as described in [102].
- **Measurement Instrumentation:** Differential voltage probes and the excitation current measured via a shunt resistor were recorded by a high-bandwidth oscilloscope (e.g., Tektronix MSO44B) to capture the dynamic signals accurately.

4.5.2 Data Summary

The experimental data was organized to facilitate the rigorous validation of the HDPI-NN model. This involved collecting data under a wide range of conditions designed to challenge the model's capabilities in terms of generality and history dependence. The training dataset was specifically curated to ensure diversity and cover a representative range of operating points for both silicon steel and ferrite materials.

- **Training Data:** To enable the model to effectively predict magnetization processes under diverse circumstances, we prioritized ensuring diversity in the training data. The training dataset included a comprehensive set of quasi-static $\mathbf{B}$–$\mathbf{H}$ loops.
  - **Silicon Steel (B35A270):** For silicon steel, which typically exhibits a higher saturation magnetic flux density (around 1.8 T), we collected data across a broad range of magnetic flux densities. This involved finer sampling at intervals

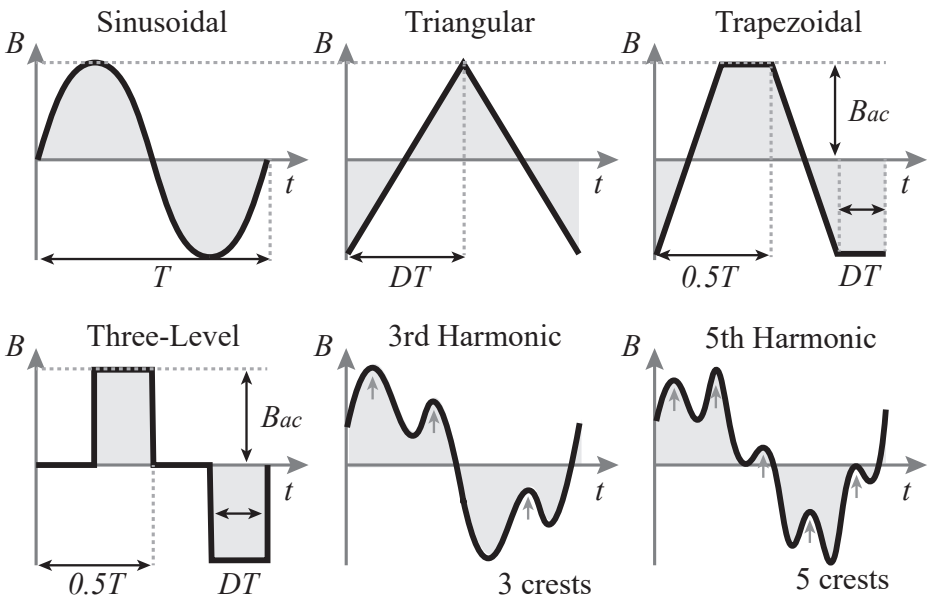

FIGURE 4.5: Waveform shapes in the training dataset.

of 0.1 T from 0.1 T to 1.8 T (18 sets) to capture the fundamental waveform behavior and saturation characteristics. Additionally, 10 sets of data at high magnetic densities (1.7 to 1.8 T) were specifically collected to observe the material's saturation behavior. All silicon steel measurements were conducted under quasi-static conditions at a frequency of 5 Hz to primarily isolate the hysteresis effects without significant influence from dynamic losses like eddy currents.

- **Ferrite (TDK N87):** For ferrite materials, which typically exhibit lower saturation magnetic flux densities (around 0.5 T for the N87 core), a similar sampling strategy was employed to ensure adequate coverage of their practical operating range. Data was collected using a fine mesh of sampling points up to approximately 0.5 T. The excitation frequency was set to 1000 Hz to balance measurement feasibility and magnetic characterization quality. Although 1000 Hz may seem relatively high, it is considered quasi-static in the context of ferrites. This assessment is supported by the observation that B–H loops measured across a range from 1 kHz to 10 kHz show negligible variation in shape, suggesting that the magnetic behavior is primarily governed by hysteresis rather

than dynamic effects such as eddy currents. The inherently high resistivity of ferrite materials significantly suppresses these frequency-dependent losses. Furthermore, performing measurements at lower frequencies would place more stringent demands on the experimental setup (e.g., higher signal-to-noise ratios), thereby increasing both the complexity and the uncertainty of the measurement process.

- **Data Sampling:** To provide a consistent input format for the neural network, a cycle-based sampling strategy was adopted for both materials. Each measured waveform was resolved into 1000 discrete points per period. This constant phase resolution allows the model to inherently account for temporal dynamics, as the effective time step between points is defined by $\Delta t = 1/(f \cdot 1000)$, where f is the excitation frequency.
- **Data Normalization:** To ensure numerical stability and efficient training. The magnetic flux density B and field strength H were normalized by their respective saturation values (B_{sat}) and peak magnitudes (H_{max}), mapping the input space into a standardized range (typically $[-1, 1]$). This preprocessing ensures that the network focuses on learning the intrinsic shape and history-dependent features of the hysteresis loops rather than the absolute scales of the signals.
- **Waveform Diversity and Memory Mechanism:** For both materials, to reflect memory mechanisms and capture the behavior under more complex excitations, magnetization data was obtained under sine flux density excitation containing third or fifth harmonics. These datasets included harmonic components at 30%, 50%, and 70% of the fundamental, with initial phase angles of 0°, 60°, and 90°. It is important to note that all flux density excitation waveforms used for model training were symmetric and did not include DC bias. This deliberate exclusion of DC bias in the training set allows us to later test the model's ability to generalize to asymmetric conditions. Figure 4.5 lists all the excitation waveforms used in the training dataset, providing a visual summary of the data diversity.

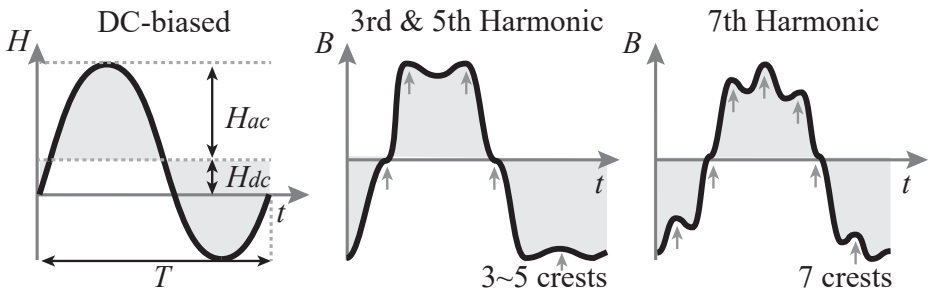

FIGURE 4.6: Waveform shapes in the testing dataset.

- **Testing Data:** The testing dataset was constructed to be entirely distinct from the training set, allowing for a rigorous evaluation of the HDPI-NN model's generalization capabilities. This dataset included:
  - **Arbitrary Quasi-Static Excitation Waveforms:** These waveforms were specifically chosen to include challenging scenarios not fully covered in the training set, such as DC-biased excitations and waveforms with higher-order harmonics or combinations of harmonics, which generate teardrop-shaped BH loops and intricate minor loops. Figure 4.6 illustrates these challenging waveforms used for testing, highlighting the presence of DC bias and higher-order harmonics, and emphasizing the need for a model with robust memory and history-dependent capabilities.

TABLE 4.2: Number of Data Points for Model Training and Testing

Training				
Type	Sine	Tri.	Trap.	Three-level
#Number	28	8	32	24
Type	3rd harm.	5th harm.	Total	
#Number	72	48	212	

Testing				
Type	DC biased	3rd&5th harm.	7th harm.	Total
#Number	85	17	17	119

- **Quantitative Data Summary:** To provide a clear overview of the experimental effort and the scope of the collected data, Table 4.2 summarizes the number of data points acquired for each type of excitation waveform used in both training and testing. This table quantifies the dataset size, offering insight into the coverage and

diversity of the validation process. The values presented correspond to the silicon steel measurements; while the dataset for ferrite cores follows the same structure, the exact numbers may vary slightly due to differences in validation objectives (e.g., the absence of third- and fifth-harmonic data), though the overall scale remains comparable.

4.6 Validation Results

This section presents the experimental validation of the HDPI-NN model, demonstrating its performance in accurately predicting magnetic field strength (H) and core loss density (P_v) under various arbitrary quasi-static excitation waveforms. The validation is conducted using the prepared test dataset, which includes conditions with DC bias and higher-order harmonics, designed to challenge the model's generality and history-dependent modeling capabilities. The performance of the HDPI-NN is evaluated based on key metrics, and comparative analyses are performed against the MMINN model to highlight the advantages of the proposed approach.

4.6.1 Evaluation Metrics

To quantitatively assess the performance of the HDPI-NN model, several key metrics are employed, consistent with common practices in magnetic modeling and the analysis presented in [99]. These metrics evaluate both the accuracy of the magnetic field prediction and the core loss estimation.

- **Magnetic Field Prediction Accuracy:**
  - **Coefficient of Determination (R^2):** This metric measures the goodness of fit between the predicted magnetic field strength (H_{pred}) and measured sequences (H_{meas}). It quantifies the extent of correlation, with a value of 100% indicating

a perfect match. R^2 is calculated as:

$$R^2 = 1 - \frac{\sum_{i=1}^{N}(H_{meas}(t_i) - H_{pred}(t_i))^2}{\sum_{i=1}^{N}(H_{meas}(t_i) - \bar{H_{meas}})^2}, \tag{4.9}$$

where N is the number of data points in the sequence, $H_{meas}(t_i)$ and $H_{pred}(t_i)$ are the predicted and measured field strengths at point i, respectively, and $\bar{H_{meas}}$ is the mean of the measured field strength sequence.

- **Normalized Root Mean Squared Error (NRMSE):** This metric provides an alternative measure of the average prediction error for the magnetic field, normalized by the peak measured value to make it scale-independent. It is calculated as:

$$NRMSE_H = \frac{1}{H_p}\sqrt{\frac{1}{N}\sum_{i=1}^{N}(H_{meas}(t_i) - H_{pred}(t_i))^2}, \tag{4.10}$$

where H_p is the peak amplitude of the measured magnetic field strength sequence.

- **Core Loss Estimation Accuracy:**
  - **Mean Absolute Percentile Error (MAPE):** This metric quantifies the average relative error between the predicted core loss density ($P_{v,pred}$) and the measured core loss density ($P_{v,meas}$):

$$MAPE = \frac{|P_{v,pred} - P_{v,meas}|}{P_{v,meas}} \times 100\%. \tag{4.11}$$

  - **95th Absolute Percentile Error (95% APE):** This metric indicates the error value below which 95% of the absolute relative errors fall. It provides insight into the typical error range and helps identify potential high-error scenarios.

4.6.2 Performance on Common Excitation Waveforms

To assess the HDPI-NN's performance on more standard, yet still relevant, operating conditions, we evaluated its predictions on common excitation waveforms. These tests are important

to ensure that the model also performs well under less extreme scenarios, providing a baseline for its capabilities.

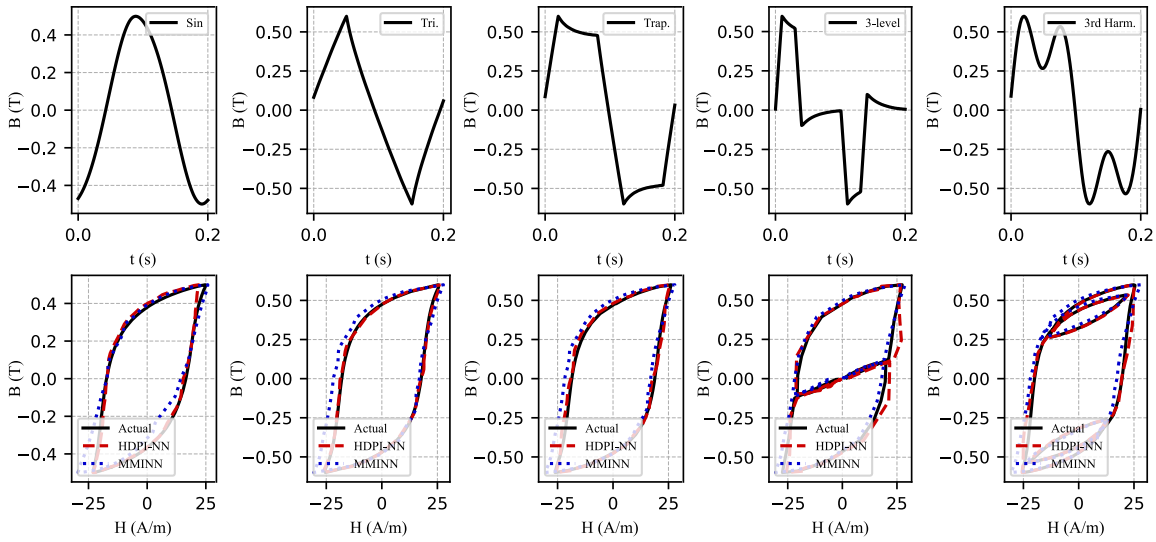

FIGURE 4.7: Simulated B–H loops of silicon steel B35A270 under typical common flux excitation waveforms.

As illustrated in Figure 4.7, the HDPI-NN model was used to predict $\mathbf{B}$–$\mathbf{H}$ loops for silicon steel B35A270 under typical common flux excitation waveforms, including sinusoidal, triangular, trapezoidal, and three-level shapes. For these symmetrical and relatively smooth waveforms, the model demonstrated highly accurate predictions, with both models achieving R^2 scores of approximately 98% for the predicted H and core loss relative errors remaining below 4%. This indicates that the HDPI-NN can effectively capture the fundamental magnetization processes even in these less complex scenarios. The core loss estimation for these common waveforms also showed satisfactory accuracy. The HDPI-NN's predictions aligned well with the measured core loss values, with errors generally falling within acceptable engineering tolerances (<5%).

To contextualize these results, a simplified version of the MMINN model, comprising only the static subnetwork, was included as a benchmark for comparison [99]. Due to its mechanism-inspired structure, this reduced the MMINN still achieved reasonable accuracy under steady-state, symmetric conditions. However, the primary strength of the HDPI-NN lies in its ability to generalize beyond such idealized cases to more complex, history-dependent excitations,

where the performance of simplified the MMINN becomes limited. A detailed comparison under these conditions is presented in Section 4.6.3.

In addition to improved prediction accuracy, the HDPI-NN offers a significant advantage in terms of structural efficiency. As summarized in Table 4.3, the HDPI-NN model requires only 436 trainable parameters, compared to 990 parameters in the MMINN. This is achieved through its compact operator-based architecture and specialized reversible/irreversible sub-networks, whereas the MMINN relies on a fully connected feedforward neural network to represent the entire hysteresis behavior. The reduced parameter count not only lowers memory and computational requirements but also facilitates faster inference, making the HDPI-NN more practical for deployment in real-time or resource-constrained environments.

TABLE 4.3: The HDPI-NN and the MMINN structure comparison table

Index	HDPI-NN	MMINN
Stop operator	30	30
FNN layer	2(rev. subnet) + 1 (output)	1
FNN neuron	5(rev. subnet) + 30 (output)	30
RNN neuron	30 (irrev. output)	0
Activation	tanh	sigmoid
Parameters	436	990

4.6.3 Performance on Arbitrary Quasi-Static Excitation Waveforms

This subsection presents the validation results of the HDPI-NN model on the prepared testing dataset, which includes various arbitrary quasi-static excitation waveforms, such as DC-biased and harmonic-rich signals. These tests are crucial for evaluating the model's generality and its ability to capture history-dependent effects.

- **Performance under DC Bias:** To assess the model's capability to handle DC bias, experiments were conducted with silicon steel B35A270 under varying DC bias levels (e.g., 20 A/m, 40 A/m, 60 A/m, 80 A/m, 100 A/m) while applying a reversal flux density of 1.4 T. The predicted $\mathbf{B}$–$\mathbf{H}$ loops were compared against the measured data. As shown in Figure 4.8 and quantified in Table 4.4, the HDPI-NN model demonstrated excellent accuracy in capturing the $\mathbf{B}$–$\mathbf{H}$ loop shape, including the

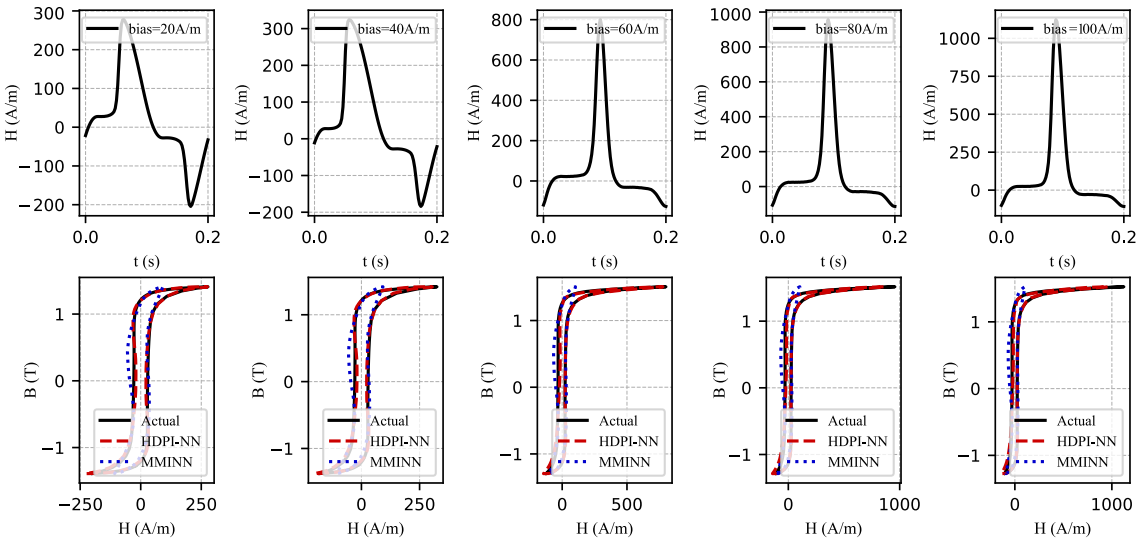

FIGURE 4.8: Simulated B–H loops of silicon steel B35A270 under high bias conditions (20 A/m, 40 A/m, 60 A/m, 80 A/m, and 100 A/m) with 1.4T reversal flux density.

characteristic water-drop shaped envelope, even under significant DC bias. The R^2 values for magnetic field prediction remained high (e.g., above 96% for most DC bias levels), and the MAPE for core loss was notably low (e.g., around 5-8% for silicon steel). In contrast, the MMINN model's performance degraded significantly under DC bias, exhibiting lower R^2 values and higher core loss errors, underscoring the importance of explicit memory mechanisms and improved reversible magnetization modeling.

TABLE 4.4: The HDPI-NN and the MMINN model prediction error in biased data

Model	Metric	20A/m	40A/m	60A/m	80A/m	100A/m
HDPI-NN	R^2	98.5%	96.9%	99.4%	98.7%	97.5%
	MAPE	2.13%	2.62%	0.43%	0.67%	1.35%
MMINN	R^2	66.6%	55.8%	25.3%	17.9%	12.5%
	MAPE	2.75%	2.10%	8.15%	8.06%	7.50%

- **Performance under Harmonic Excitations:** To evaluate the model's generality with complex waveforms, tests were conducted on silicon steel B35A270 under excitations containing combinations of third and fifth harmonics, as well as seventh

harmonics. Figure 4.9 visually compares the simulated **B–H** loops of the HDPI-NN and the MMINN against measured data for these conditions. The HDPI-NN accurately captured the intricate minor loops generated by these harmonic-rich waveforms, demonstrating its ability to learn and reproduce complex magnetization paths.

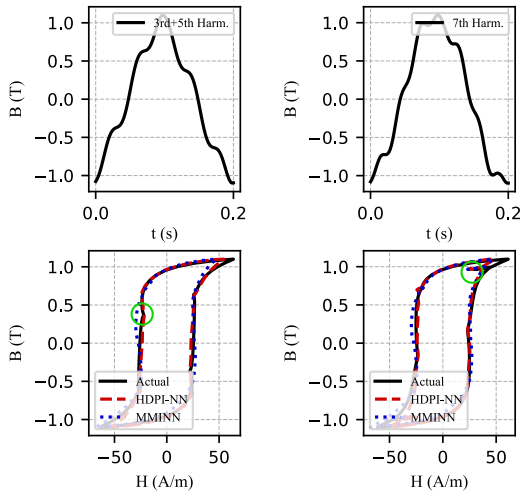

FIGURE 4.9: Simulated B–H loops of silicon steel B35A270 under 3rd & 5th and 7th order harmonic conditions.

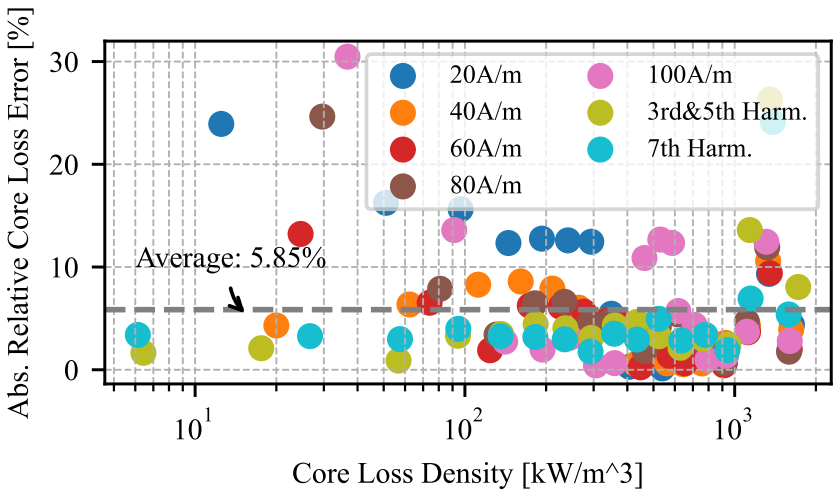

FIGURE 4.10: Core loss distribution for silicon steel B35A270 testing dataset.

- **Comprehensive Performance Analysis for The Testing Dataset:** To provide a comprehensive view of the model's core loss prediction accuracy across a range

of operating conditions, the distribution of absolute relative core loss error was analyzed on the silicon steel B35A270 testing dataset. Figure 4.10 illustrates this distribution, plotting the absolute relative core loss error against the core loss density. The figure shows that for most operating points, the HDPI-NN model achieves low core loss errors, with the average error being approximately 5.85%. The distribution is generally concentrated at low error values, indicating good overall accuracy. The spread of errors across different excitation types (DC bias, harmonics) is also visualized, demonstrating the model's consistent performance across these varied conditions. The quantitative results, presented in Table 4.5, further confirm the HDPI-NN's superior accuracy in terms of R^2 and core loss MAPE compared to the MMINN under these challenging conditions.

TABLE 4.5: The HDPI-NN and the MMINN model performance comparison table

Metric	HDPI-NN	MMINN
H normalized root means square error	1.15%	6.89%
Goodness of fit	96.0%	27.63%
P_v mean absolute percentile error	5.58%	16.57%
P_v 95th percentile error trained with training set	15.96%	58.0%
P_v 95th percentile error trained with all data	2.66%	56.6%

4.6.4 Cross-Material Validation

To evaluate the cross-material generalizability of the HDPI-NN model, its performance was further validated on ferrite material (TDK N87) using a set of arbitrary quasi-static excitations, including DC bias and harmonic-rich waveforms containing seventh-order harmonics. Experimental measurements were conducted on TDK N87 samples under these excitation conditions, and the results are presented in Figure 4.11. The simulated B–H loops generated by the HDPI-NN model exhibit excellent agreement with the measured curves, demonstrating its ability to accurately reproduce the distinct hysteresis behavior of ferrite materials under both harmonic and dc bias conditions.

In addition to qualitative loop comparisons, a quantitative analysis of the core loss prediction error was also performed. Figure 4.12 shows the distribution of the absolute relative core loss

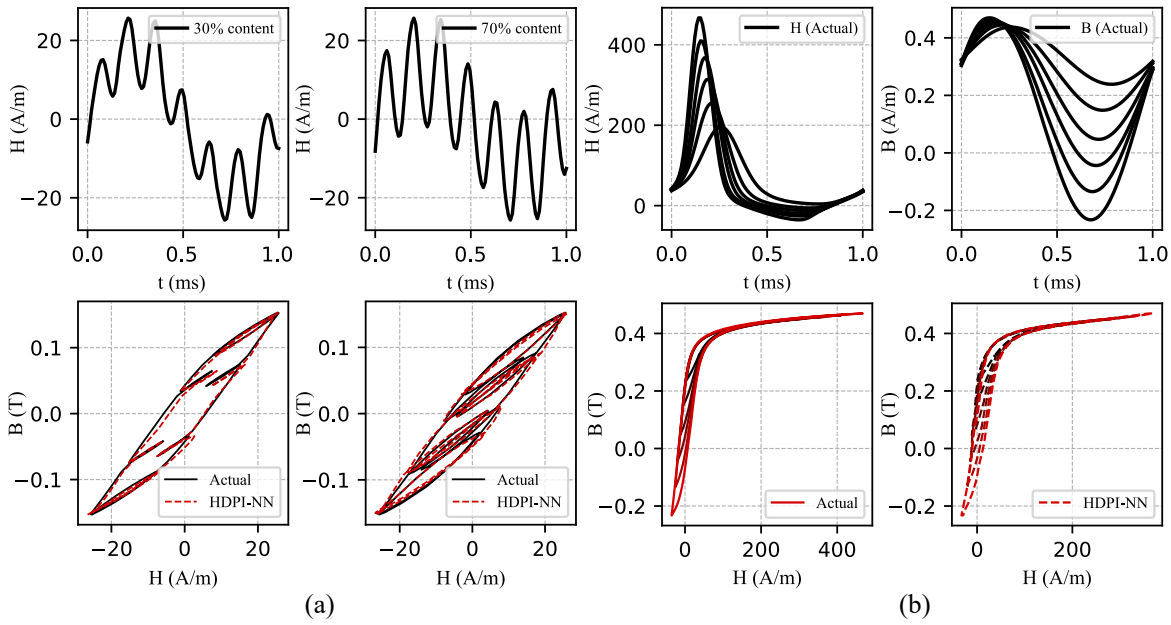

FIGURE 4.11: B–H loop comparison on ferrite (TDK N87): (a) Harmonic excitation; (b) DC bias excitation.

error with respect to core loss density across various operating points. The prediction errors remain within a moderate range across most operating points, with the majority of absolute relative core loss errors falling below 10%, where the average error on the ferrite dataset is approximately 7.9%. This stable performance across different excitation conditions, including 30%, 50% and 70% seventh-harmonic content as well as 60 A/m DC bias, demonstrates the robustness and generalization capability of the HDPI-NN architecture when applied to ferrite materials.

4.7 Discussion and Summary

This chapter presented the HDPI-NN, the second hybrid modeling strategy explored in this thesis. Building upon the foundational understanding of magnetic material behavior and core loss mechanisms established in Chapter 2, and addressing the limitations of the initial MMINN model introduced in Chapter 3, the HDPI-NN was developed to tackle the critical challenge of accurately modeling magnetic material hysteresis under arbitrary quasi-static excitation waveforms.

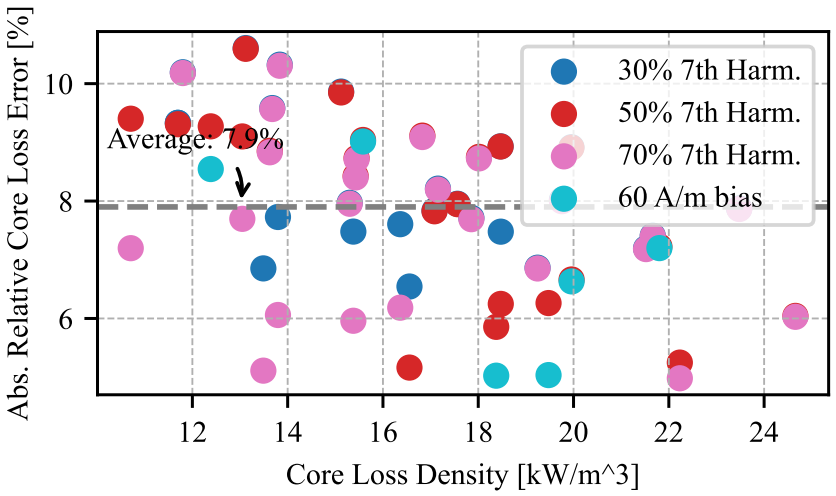

FIGURE 4.12: Core loss distribution for ferrite N87 testing dataset (7th harmonics and DC-biased conditions).

The development and validation of the HDPI-NN model have yielded several key findings that significantly advance the field of magnetic material modeling. A primary contribution is its ability to accurately model magnetic hysteresis and predict core loss under a wide range of arbitrary quasi-static excitation waveforms, including those with DC bias and intricate minor loops. This capability stems from the integration of a Generalized Stop Operator, which explicitly incorporates reversible magnetization components (inspired by Jiles-Atherton) and robust memory mechanisms. This enhanced physical grounding allows the HDPI-NN to capture complex history-dependent phenomena more faithfully than the MMINN, as evidenced by its superior accuracy in **B–H** loop prediction (e.g., high R^2 values in Figure 4.8, Figure 4.9) and core loss estimation (low MAPE and 95% APE as quantified in Table 4.5). Furthermore, the physics-informed approach contributes to the HDPI-NN's data efficiency, enabling high accuracy with a relatively smaller dataset compared to purely data-driven models.

While the HDPI-NN model demonstrates significant progress in accurately modeling magnetic material hysteresis and core loss under arbitrary quasi-static excitations, its current scope is primarily focused on these conditions. It does not explicitly incorporate macroscopic dynamic effects such as eddy currents or skin effects, which become dominant at higher frequencies and are inherently influenced by component geometry. Recognizing these limitations, the

research presented in this thesis progresses to Chapter 5, where we introduce the Neural-Enhanced Physics (NEP) paradigm. This paradigm aims to address the remaining challenges by combining the accurate material behavior captured by the HDPI-NN with a scalable physics-based solver. The Neural-Enhanced Dynamic Circuit Model (NE-DCM), developed in Chapter 5, will embed the HDPI-NN material model within a mesh-based dynamic circuit solver. This integration is crucial for achieving accurate, generalizable, and dimension-aware core loss prediction across a wider range of operating conditions, including those involving dynamic effects and varying geometries, thereby providing a comprehensive solution for modern magnetic component design automation. In conclusion, the HDPI-NN represents a significant step towards this ultimate goal, offering a robust and data-efficient material model that lays the groundwork for more advanced and integrated modeling strategies.

CHAPTER 5

Neural-Enhanced Physics Paradigm: Accurate and Scalable Modeling with NE-DCM

This chapter introduces the NEP paradigm and its implementation in the NE-DCM. Building upon the foundational understanding of magnetic material behavior and core loss mechanisms established in Chapter 2, and leveraging the insights gained from the initial hybrid modeling explorations with the MMINN (Chapter 3) and HDPI-NN (Chapter 4), this chapter presents a comprehensive framework designed to achieve accurate, generalizable, and scalable core loss prediction across a wide range of operating conditions and component dimensions.

5.1 Introduction

As highlighted in Chapter 1, accurately modeling core loss is essential for modern power electronics, but existing model-driven and data-driven approaches face fundamental trade-offs between accuracy, scalability, and generality. Physics-Based Dynamic Models (Section 2.2.4) offer inherent scalability based on dimensions, yet their accuracy is often limited by the fidelity of the underlying material models when faced with complex excitations. Conversely, high-fidelity Physics-Based Hysteresis Models (Section 2.2.3) or advanced Analytical Hysteresis Models (Section 2.2.2), while capturing intricate material behavior, typically lack inherent scalability across different component dimensions. Pure data-driven models (Section 2.3.1), despite their accuracy on trained data, are data-hungry and struggle with generalization to unseen dimensions. Even existing hybrid models (Section 2.3.2), while promising, have not fully resolved the combined challenge of accuracy, scalability, and data efficiency for arbitrary excitations across varying dimensions.

Scalability is a critical attribute for core loss models in modern power electronics applications, where magnetic components are subjected to diverse operating conditions, including wide frequency ranges, non-sinusoidal excitations, varying temperatures, and different material types [34], [56]. A truly scalable model can generalize well across these conditions and, crucially, across different component dimensions, significantly reducing the need for extensive

recalibration or retesting under every new scenario or component size. This is particularly important as the industry moves toward high-frequency and wide-bandgap converter technologies, where waveform shapes and thermal environments vary dynamically. Moreover, scalable models facilitate efficient design optimization and system-level integration, enabling accurate loss estimation in circuit simulation, thermal modeling, and EMI analysis. They also support rapid evaluation of emerging materials and novel core dimensions without requiring bespoke model development for each case. Therefore, scalability not only enhances the model's practicality but also accelerates the development cycle of magnetic devices.

Building upon the foundational understanding of magnetic material behavior and core loss mechanisms from Chapter 2, and leveraging the insights gained from the initial hybrid modeling explorations with the MMINN (Chapter 3), which successfully addressed aspects of data efficiency and accurate arbitrary waveform modeling at the material level, and HDPI-NN (Chapter 4), which provided a high-fidelity material model for complex quasi-static excitations — this chapter proposes the NEP paradigm as a novel, comprehensive framework to achieve accurate, generalizable, and scalable core loss prediction across a wide range of operating conditions and component dimensions. This integration is crucial as the MMINN, while data-efficient for symmetric conditions, lacked the generality for arbitrary waveforms, and HDPI-NN, while accurate for quasi-static arbitrary excitations, did not inherently account for dynamic effects and dimensional scalability. The NE-DCM, therefore, represents the culmination of this progressive research journey, directly addressing the full spectrum of challenges identified in Chapter 1. The core idea of NEP is to create a synergistic hybrid architecture that leverages the strengths of both physics-based models and neural networks through a principled decomposition of the problem. Specifically, NEP aims to achieve the thesis objectives of high accuracy, robust scalability, and broad generality (Section 1.4) by employing a scalable, physics-based solver to handle the dimension-dependent dynamic effects, while embedding a data-efficient, high-fidelity neural network to capture the complex, non-linear material behavior. This approach is designed to overcome the limitations of relying on simplified physics assumptions in model-driven approaches and the data hunger/lack of

scalability in data-driven methods. This section introduces the NEP paradigm and its implementation as the Neural-Enhanced Dynamic Circuit Model (the NE-DCM), with subsequent sections detailing its architecture, implementation, and rigorous validation.

5.2 The NE-DCM Integrated Architecture

The NE-DCM is the practical implementation of the NEP paradigm for core loss modeling. Its integrated architecture is designed to address the multifaceted challenges by synergistically combining a physics-based solver with a neural network-based material model. This strategic integration directly contributes to the thesis objectives of achieving accurate, generalizable, and scalable core loss prediction.

The NE-DCM fundamentally extends the Generalized Dynamic Circuit Model (GDCM) (Section 2.2.4) by replacing its traditional, often simplified, material model with an advanced neural network-based material model. The GDCM, with its inherent capability to discretize the core's cross-section into concentric segments and represent them as a coupled RL mesh network (Figure 2.7), provides the scalable framework for handling dimension-dependent electromagnetic dynamics and eddy currents. Figure 5.1 illustrates the overall integrated architecture of the NE-DCM. It shows how the physics-based dynamic solver component (derived from GDCM principles) interacts with the neural material model component. The total core loss and current response is determined by the output of this integrated system.

5.2.1 Physics-Based Dynamic Solver Component

The Physics-Based Dynamic Solver Component serves as the scalable backbone of the NE-DCM architecture, primarily derived from the Generalized Dynamic Circuit Model (GDCM) (Section 2.2.4) [31]–[33]. Its main role is to accurately capture the macroscopic dynamic effects, such as eddy currents and skin effect, and to explicitly account for the component's dimensions, ensuring the model's scalability.

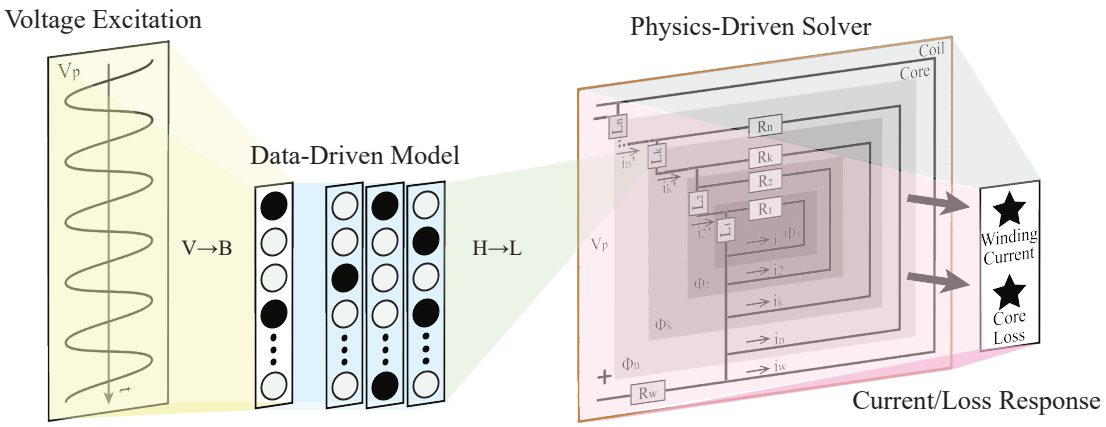

FIGURE 5.1: The NE-DCM Integrated Architecture.

As described in Section 2.2.4, the GDCM works by conceptually discretizing the magnetic core's cross-section into multiple concentric segments. Each segment is then represented as an element in an equivalent electrical circuit network. Figure 5.2 illustrates the core idea of the GDCM, showing the conceptual discretization of the core cross-section and its corresponding equivalent circuit analogy as a coupled RL mesh network. This mesh network formulation allows for the modeling of the spatial distribution of magnetic flux and eddy currents within the core, which is crucial for high-frequency applications where skin effect is prominent. The number of segments, n, is determined based on the core's dimensions and material properties to ensure sufficient spatial resolution for capturing non-uniform field distributions at high frequencies, particularly considering the skin depth δ, as follows:

$$\Delta y_{max} \leq \delta = \sqrt{\frac{1}{\pi f \sigma \mu_i \mu_0}}, \tag{5.1}$$

where Δy_{max} is the maximum allowable segment thickness (corresponding to the shortest dimension of the cross-section), f is the frequency, σ is the electrical conductivity, μ_i is the initial permeability and μ_0 is the vacuum permeability.

The governing equations for this component are derived from Maxwell's equations [103] applied to the discretized segments, forming a system of coupled differential equations. These equations describe the dynamic interaction between the applied voltage, the winding current, and the induced eddy currents within the core segments. For the coil winding, Faraday's

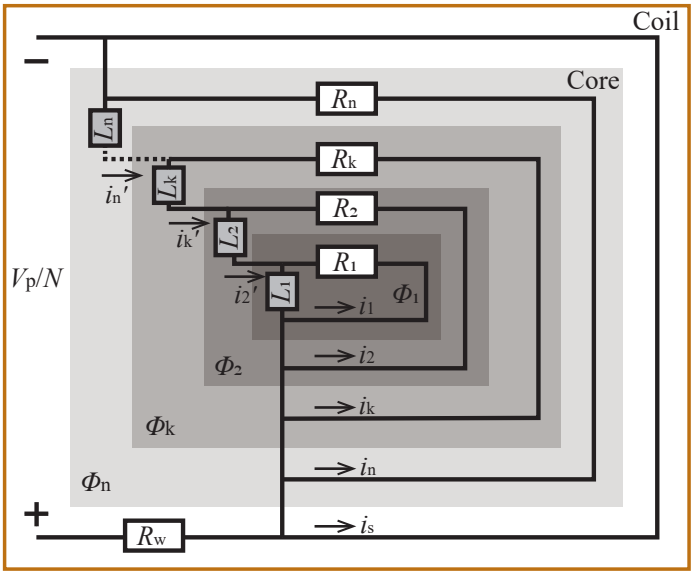

FIGURE 5.2: Conceptual illustration of core cross-section discretization and equivalent circuit in the GDCM.

Law relates the applied primary voltage (V_p) to the total flux rate of change across all core segments:

$$\text{Coil:} \qquad R_w i_w + N\frac{d(\phi_1 + \phi_2 + ... + \phi_n)}{dt} = V_p, \tag{5.2}$$

where R_w is the winding resistance, i_w is the current flowing through the coil, ϕ_k is the magnetic flux in the k-th segment, and N is the number of turns in the winding. For modeling convenience, voltage and flux quantities are typically normalized per turn, allowing the governing equations to reflect unit-turn characteristics. Within the core, Kirchhoff's Voltage Law (KVL) is applied to the n internal meshes formed by the segments, yielding a system of equations that describe the dynamic relationship between the mesh currents (i_k') and the fluxes (ϕ_k):

$$\begin{aligned} \text{Core:} \qquad R_n i_n + \frac{d(\phi_1 + \phi_2 + ... + \phi_n)}{dt} &= 0, \\ &... \\ R_2 i_2 + \frac{d(\phi_1 + \phi_2)}{dt} &= 0, \\ R_1 i_1 + \frac{d(\phi_1)}{dt} &= 0. \end{aligned} \tag{5.3}$$

To solve this system, we use mesh analysis, where a mathematical mesh current is defined for each closed loop in the circuit. It is important to distinguish this from the physical eddy current. The physical eddy current i_k flowing in the k-th concentric segment of the core is the net result of the mesh currents flowing on its boundaries. Specifically, i_k is equal to the difference between the adjacent mesh currents: $i'_k - i'_{k-1}$.

This complete system can be compactly expressed in matrix form using mesh analysis:

$$\mathbf{R}\,\mathbf{i}' + \mathbf{L}[\frac{\mathbf{di}'}{\mathbf{dt}}] = \mathbf{V}, \tag{5.4}$$

where $\mathbf{i}' \in \mathbf{R}^n$ is the mesh current vector, and $\mathbf{V} \in \mathbf{R}^n$ is the mesh-wise voltage excitation vector, where elements are zero except for the last entry related to the coil current ($V_n = \frac{R_n}{R_w+R_n}(\frac{V_p}{N})$). $\mathbf{L} \in \mathbf{R}^{n\times n}$ is a diagonal matrix whose entries represent the differential inductance of each mesh ($L_k = \frac{d\phi}{di'}$ for $k = 1, 2, \ldots, n$) and $\mathbf{R} \in \mathbf{R}^{n\times n}$ is the non-diagonal mesh resistance matrix, defined as:

$$\mathbf{R} = \begin{bmatrix} R_1 & -R_1 & 0 & \cdots & 0 \\ -R_1 & R_1+R_2 & -R_2 & \cdots & 0 \\ \vdots & \vdots & \ddots & \vdots & 0 \\ 0 & \cdots & & -R_{n-1} & R_{n-1}+\frac{R_n Rw}{R_n+Rw} \end{bmatrix}.$$

The critical elements in these equations are the differential inductances (L_k) and the dynamic resistances (R_k) for each segment. Unlike conventional static hysteresis models where these parameters are often simplified, in the NE-DCM, these time-varying parameters are dynamically determined at each time step based on the core's magnetic state, using the Neural Material Model Component (as detailed in Section 5.2.2). This dynamic parameter update via the neural network significantly improves the accuracy of magnetic material characterization within the GDCM solver.

The key strength of this component is its inherent scalability. Since its parameters (e.g., segment resistances, nominal inductances) are calculated directly from the core's physical dimensions and material conductivity, the solver can be systematically adapted to different

core sizes. This enables the NE-DCM to generalize its predictions across varying component dimensions, a critical aspect of the thesis objective.

5.2.2 Neural Material Model Component

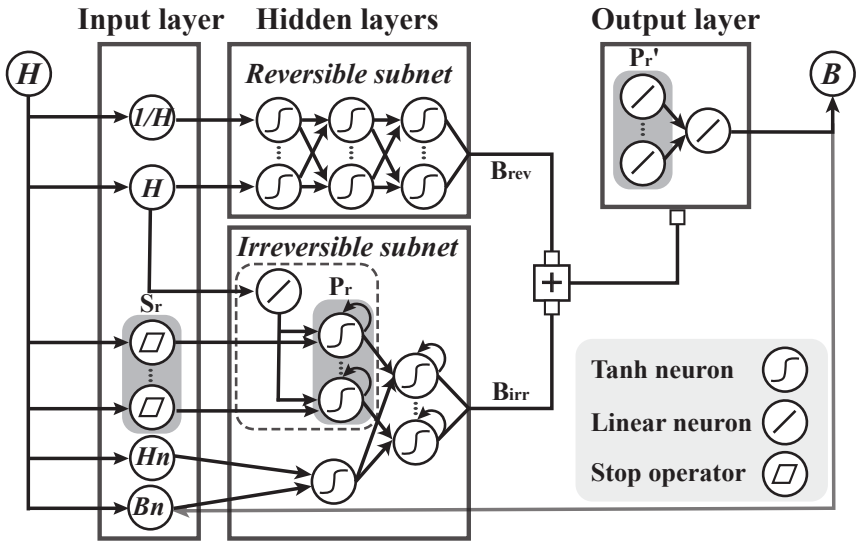

FIGURE 5.3: Architecture of the Modified HDPI-NN model for H-to-B mapping.

The Neural Material Model Component is the high-fidelity core of the NE-DCM architecture, tasked with accurately capturing the complex, non-linear, and history-dependent magnetization behavior of the magnetic material. This component is based on the History-Dependent Prandtl-Ishlinskii Neural Network (HDPI-NN), developed in Chapter 4.

As detailed in Chapter 4, HDPI-NN significantly advances material modeling by incorporating key physical mechanisms that were previously lacking or simplified in traditional hysteresis models, such as reversible magnetization (inspired by Jiles-Atherton concepts, Section 2.2.3) and historical dependencies (memory mechanism) (Section 4.2). These enhancements are achieved through a generalized stop operator framework, parameterized and learned by a neural network.

Crucially, within the NE-DCM framework, the Neural Material Model Component functions as a forward H-to-B mapping (taking magnetic field H as input and predicting magnetic flux

density B as output). This is a transformation from its primary H-to-B mapping in Chapter 4, to suit the requirements of a circuit solver, where B needs to be determined from H calculated within each segment.

To achieve this, we transformed the fundamental building blocks of the network, converting the stop operators (S_r) into play operators (P_r) suitable for the $H \rightarrow B$ mapping. This transformation process, detailed in [66], [90], [104]. Furthermore, to accurately capture phenomena like reversible magnetization and memory effects, which are critical for precise minor loop prediction, the standard play operator was enhanced. Figure 5.3 illustrates the architecture of this Modified HDPI-NN as implemented in the NE-DCM. It comprises reversible and irreversible subnetworks. The inputs to this H-to-B mapping include the current magnetic field strength $H(t)$ (which is the effective magnetic field inside the certain segment), its time derivative (dH/dt), and crucially, historical information (e.g., previous magnetic flux values $B(t-1)$, reversal points (H_n, B_n)) to ensure accurate representation of memory effects. The HDPI-NN then outputs the corresponding magnetic flux density $B(t)$.

The key strength of this component is its ability to provide a high-fidelity, physically-informed non-linear material law under a wide range of arbitrary and complex excitations (including DC bias and minor loops), as rigorously validated in Chapter 4. Its data-efficient training process (Section 4.4) also contributes to the overall efficiency of the NE-DCM framework.

5.3 Simulation Workflow and Numerical Implementation

The synergy of the NE-DCM is realized through a dynamic, time-stepped coupling between its Physics-Based Dynamic Solver Component (Section 5.2.1) and the Neural Material Model Component (Section 5.2.2). This iterative process allows the model to accurately simulate the complete dynamic hysteresis behavior of the magnetic core under various excitations.

5.3.1 Overall Simulation Workflow

The overall simulation workflow for the NE-DCM model follows an iterative process at each discrete time step. Figure 5.4 provides a schematic illustration of this detailed workflow. At each step, the model calculates the current magnetic state of the core, queries the Neural Material Model (HDPI-NN) to obtain the corresponding material response, updates the parameters of the GDCM solver based on this response, and then solves the circuit equations to advance the system to the next time step. This process is repeated over the entire excitation waveform, ensuring a dynamic and self-consistent simulation of the core's electromagnetic behavior.

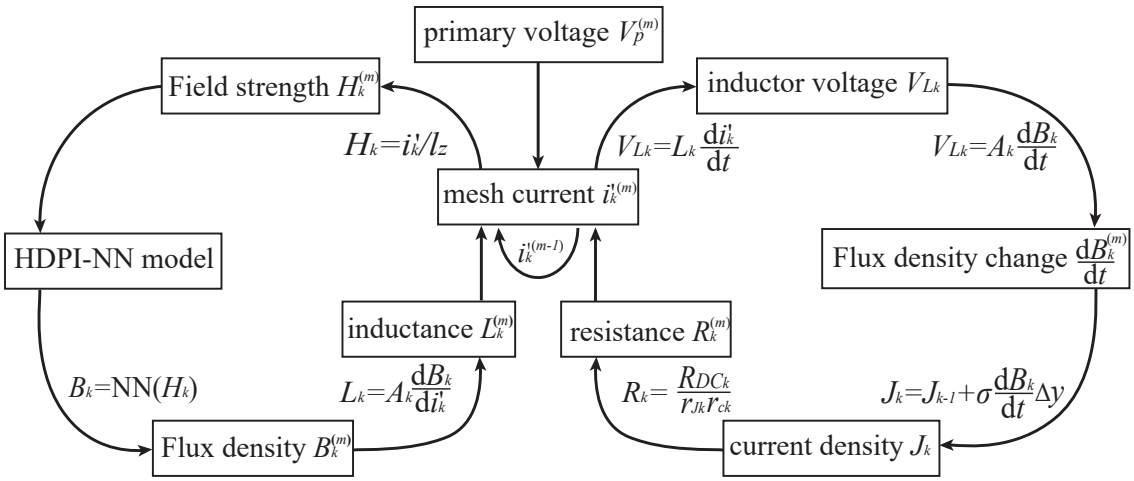

FIGURE 5.4: the NE-DCM Simulation Workflow Diagram.

5.3.2 Numerical Implementation Details

The core of the NE-DCM simulation involves a series of specific calculations performed at each discrete time step m:

- **Determine Differential Inductance ($L_k^{(m)}$):**
  - At each time step m, for each conceptual segment k in the GDCM discretization, the magnetic field $H_k^{(m)}$ is calculated directly from the mesh current $i_k'^{(m)}$

(obtained from the previous time step's solution) using Ampere's Law:

$$H_k^{(m)} = \frac{N \cdot i_k^{\prime(m)}}{l_z}. \tag{5.5}$$

– The calculated magnetic field $H_k^{(m)}$ (along with its time derivative $H_k^{(m)}/dt$ and historical information like previous reversal points, as detailed in Section 5.2.2) is fed into the Neural Material Model Component (HDPI-NN). The HDPI-NN, trained as a forward H-to-B mapping, then predicts the corresponding magnetic flux density $B_k^{(m)}$ for that segment. This step is crucial as it provides the high-fidelity, non-linear, and history-dependent material response.

– The time-varying differential inductance $L_k^{(m)}$ for each segment is then determined from the instantaneous slope of the $\mathbf{B}$–$\mathbf{H}$ trajectory provided by the Neural Material Model. Conceptually, $L_k^{(m)}$ is proportional to the differential permeability at the current operating point:

$$L_k^{(m)} = \frac{B_k^{(m)} - B_k^{(m-1)}}{H_k^{(m)} - H_k^{(m-1)}} \frac{N^2 A_k}{l_z}. \tag{5.6}$$

• **Determine Dynamic Resistance ($R_k^{(m)}$):**

– The voltage across each segmental inductor, $V_{L_k}^{(m)}$, is computed from the circuit state at time step m.

– Using Faraday's Law, the rate of change of magnetic flux density is obtained as:

$$V_{L_k}^{(m)} = A_k \cdot \frac{dB_k^{(m)}}{dt}. \tag{5.7}$$

– The eddy current density $J_k^{(m)}$ is estimated based on this flux variation, incorporating spatial resolution Δy, electrical conductivity σ, and the previously accumulated current density:

$$J_k^{(m)} = \sigma \cdot \left(\frac{dB_k^{(m)}}{dt} \right) \cdot \Delta y + J_{k-1}^{(m)}. \tag{5.8}$$

– The effective dynamic resistance $R_k^{(m)}$ is then updated using empirical correction factors r_{J_k} and r_{c_k} to reflect both classical eddy current and anomalous losses

(Section 2.1.2):

$$R_k^{(m)} = \frac{R_{DC_k}}{r_{J_k} r_{c_k}} = \frac{\frac{2a}{\sigma l_z \Delta y}}{r_{J_k} r_{c_k}}, \tag{5.9}$$

where a is the smallest physical dimension of the core segment's cross-section, and R_{DC_k} is the DC resistance of segment k.

- **Solve for the Next State $i_k'^{(m+1)}$:** With the updated differential inductances ($L_k^{(m)}$) and dynamic resistances ($R_k^{(m)}$), the discretized system of circuit equations for the GDCM (Equation 5.4 in Section 5.2.1) is formulated. This system of equations is then solved for the unknown mesh currents $i_k'^{(m+1)}$ at the next time step $m+1$. The trapezoidal integration method is commonly employed for discretizing the differential equations, offering a good balance of accuracy and stability in time-stepped simulations. Practically, the trapezoidal rule converts continuous-time elements (inductors/capacitors) into equivalent discrete-time companion circuits, where each inductor is replaced by a Norton or Thévenin equivalent plus a "memory" current source from the previous step. This approach is mathematically identical to the GDCM's original discrete-transform technique [105], which models inductors using transmission-line-style sections to represent dynamic behavior.

5.3.3 Numerical Stability and Convergence Mechanisms

To ensure robust convergence and accurate results for the highly non-linear dynamics and iterative nature of the NE-DCM simulation, several numerical stability and convergence mechanisms are incorporated:

- **Inductance Variation Limiter:** A practical consideration in the iterative solution is numerical stability. Due to the highly non-linear and history-dependent nature of the magnetic constitutive relationship provided by the HDPI-NN, the calculated differential inductance $L_k^{(m)}$ which is derived from the slope of the predicted $\mathbf{B}$–$\mathbf{H}$ curve) can exhibit abrupt, non-physical fluctuations during rapid flux transitions. This problem arises because the neural network, despite its accuracy, can be sensitive to small input variations, and its predicted $\mathbf{B}$–$\mathbf{H}$ relationship might not be perfectly

smooth or continuously differentiable everywhere, leading to excessively rapid changes in differential permeability (and thus inductance). These fluctuations can potentially lead to instability or divergence in the time-stepping numerical solver. To address this, an empirical inductance variation limiter is introduced with a tunable parameter α:

$$\tilde{L}_k^{(m)} = \min\left((1+\alpha)L_k^{(m-1)},\ \max\left(\alpha L_k^{(m-1)},\ L_k^{(m)}\right)\right). \tag{5.10}$$

This limiter ensures that the updated inductance $\tilde{L}_k^{(m)}$ at time step m does not deviate excessively from its value at the previous time step $L_k^{(m-1)}$, preventing non-physical jumps and improving numerical stability.

- **DC Bias Compensation:** A Numerical Technique for Target Condition Simulation. To accurately simulate performance under specific DC bias conditions, a feedback-based compensation mechanism is included within the simulation workflow. As illustrated in Figure 5.7 this mechanism continuously monitors the average value of the predicted primary current ($\bar{i_w}$) over previous simulation cycles. If this average current deviates from a predefined DC bias target (i_b), a small, corrective voltage offset (V_b, e.g., 1% of V_p) is dynamically added to the excitation voltage V_p.
  It is critical to emphasize that this is a numerical control loop within the solver, designed to achieve a desired simulation condition, not an adaptive component of the predictive model itself. The model does not use any external measurement data during the testing phase to correct its predictions. This process is analogous to a simple integral controller that adjusts the simulation input to ensure the output matches a user-specified operating point, which would otherwise be difficult to achieve with an open-loop voltage source. This distinction is crucial for a fair evaluation of the model's predictive capabilities.
- **Temporal Resolution and Duration:** The simulation's temporal resolution is defined by n_{step} (number of steps per cycle), which is selected to be sufficiently high (e.g., $n_{step} \geq 100$ to accurately resolve the waveform dynamics and ensure numerical stability. The total duration of the simulation, represented by the total number of simulation cycles (n_{cycle}), is determined to ensure the simulation reaches a

steady state. This is crucial for obtaining stable and meaningful core loss predictions. n_{cycle} is often guided by material properties and component dimensions, and can be calculated as:

$$n_{cycle} \approx \frac{5}{f} \cdot \frac{A_{eff}\mu_i\mu_0}{l_z R_w}. \tag{5.11}$$

where A_{eff} is the total effective cross-sectional area, μ_i is the initial permeability of the material, μ_0 is the vacuum permeability, f is the operating frequency, l_e is the effective magnetic path length, and R_w is the winding resistance.

These implementation details ensure that the NE-DCM model can robustly and accurately simulate the complex dynamic behavior of magnetic components across diverse operating conditions.

5.4 Experimental Setup and Data Preparation

This section details the experimental setup employed for acquiring the necessary magnetic material data and outlines the organization of the collected data specifically for validating the NE-DCM. To rigorously evaluate the model's performance in terms of accuracy, generality, and scalability across varying component dimensions, a targeted data acquisition strategy was implemented. The primary validation was conducted on TDK N87 ferrite toroidal cores of varying dimensions. Furthermore, to critically assess the material extensibility of the NEP paradigm and its associated workflow, a complete, parallel validation was performed on a second, distinctly different material, TDK T65, which exhibits contrasting magnetic properties. This dual-material approach allows for a comprehensive assessment of the framework's robustness and portability.

5.4.1 Experimental Setup

Magnetic material characterization for the NE-DCM validation was performed using specialized experimental setups tailored to the material type and the desired measurement conditions,

aiming to rigorously evaluate the model's performance in terms of accuracy, generality, and scalability across varying component dimensions.

For ferrite materials (e.g., TDK N87 toroidal cores), a two-winding DC-bias injection method was employed, as described in [91], [93]. Figure 5.5 illustrates the schematic of this experimental setup, showing the principle of the two-winding method with DC bias injection. This setup enables the controlled superposition of a DC bias onto the excitation waveform, allowing for testing under conditions common in many power converters. Figure 5.6 provides a photograph illustrating the hardware configuration of this magnetic test system. The system components included:

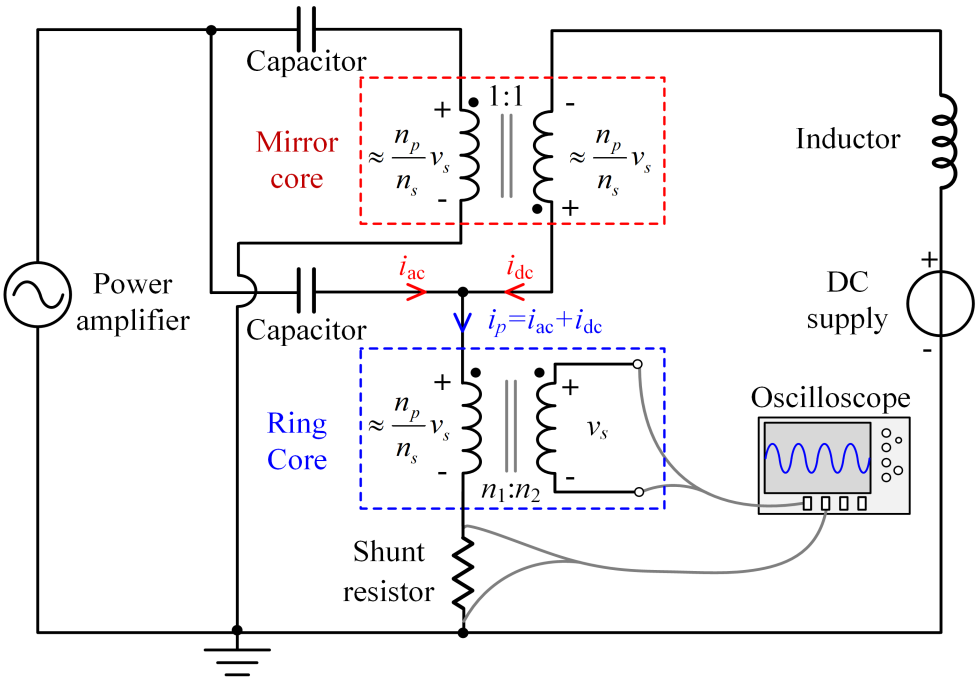

FIGURE 5.5: Schematic of the two-winding DC-bias injection method for magnetic characterization.

- **Function Generator & Power Amplifier:** An Aigtek ATA-4052C power amplifier, driven by a function generator, was used to apply AC excitation waveforms to the Device Under Test (DUT).
- **DC Power Supply:** An ITECH IT6720 DC power supply was utilized to provide the DC bias current, often involving a mirror transformer to allow for controlled superposition of DC bias onto the excitation waveform [93].

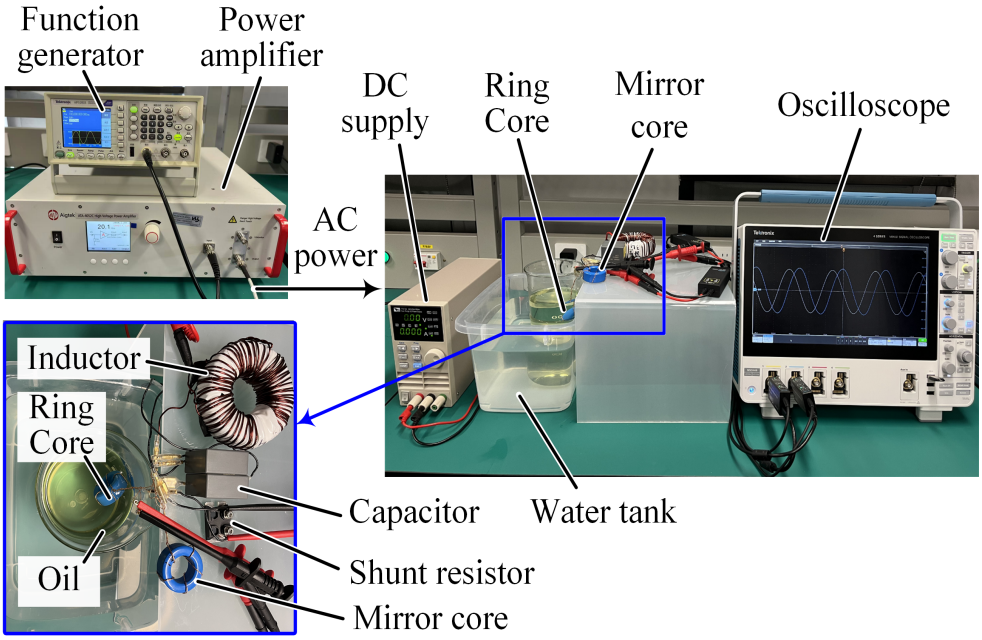

FIGURE 5.6: Hardware configuration of the magnetic test system.

- **Measurement Instrumentation:** Current and voltage signals were measured using Micsig DP1500 differential voltage probes and a 1 ohm shunt resistor, recorded by a Tektronix MSO44B oscilloscope.
- **Temperature Control:** All tests were conducted under controlled ambient conditions (approximately 20°C) with the DUT submerged in an oil tank to ensure stable temperature.

The DUTs for the NE-DCM validation were TDK N87 ferrite toroidal cores of significantly different sizes. Table 5.1 summarizes the detailed parameters for the three cores used: Core A, Core B, and Core C. These cores were chosen to provide a robust evaluation of the model's scalability across various dimensions.

From the measured voltage ($v_s(t)$) across the secondary winding and current ($i_w(t)$) in the primary winding, magnetic field strength ($H(t)$) and magnetic flux density ($B(t)$) were

TABLE 5.1: Parameters of Test Toroidal Magnetic Cores

Parameter	**Core A**	**Core B**	**Core C**
Outer diameter d_{out} (mm)	12.5	40.0	34.0
Inner diameter d_{in} (mm)	7.9	24.0	20.5
Height h (mm)	6.35	16.0	12.5
Effective magnetic path length l_e (mm)	31.17	96.29	82.06
Effective cross-sectional area A_e (mm^2)	14.96	125.3	82.6
Core volume V_e (mm^3)	466	12070	6778
Electrical conductivity σ (S/m)	0.1	0.1	0.1
Initial permeability μ_i	2200	2200	2200

calculated using standard formulas. $H(t)$ is derived from Ampere's Law:

$$H(t) = \frac{n_p i_w(t)}{l_e}, \tag{5.12}$$

where n_p is the number of turns in the excitation (primary) winding and l_e is the effective magnetic path length. $B(t)$ is derived from the voltage induced in the sensing (secondary) winding via Faraday's Law of Induction, by integrating the voltage over time, accounting for the effective cross-sectional area (A_e):

$$B(t) = \frac{1}{n_s A_e} \int v_s(\tau)\, d\tau, \tag{5.13}$$

where n_s is the number of turns in the sensing (secondary) winding. The core loss density (P_v) for each measured $\mathbf{B}$–$\mathbf{H}$ loop is calculated by integrating the instantaneous power over one cycle. This represents the energy dissipated per unit volume per cycle:

$$P_{\text{v}} = \frac{1}{N_w T} \int_{t_0}^{t_0+N_w T} v_s(t) \cdot i_s(\tau), d\tau, \tag{5.14}$$

where N_w is the number of excitation cycles and T is the period. The sampling rate was set to 1000 times the test frequency, ensuring 1000 points per cycle.

5.4.2 Data Preparation

The experimental data for the NE-DCM validation was meticulously prepared to facilitate a rigorous evaluation of the model's scalability and generality. This involved collecting data

from specific N87 ferrite toroidal cores (Core A, B) under a wide range of conditions, as well as leveraging an external dataset for comparative analysis.

The data preparation for the NE-DCM validation rigorously follows a two-stage strategy. Figure 5.7 provides a detailed flowchart of the NE-DCM workflow, highlighting the distinct Training process and Testing process stages. This strategy distinctly separates material-specific learning from dimension-specific calibration, optimizing data usage.

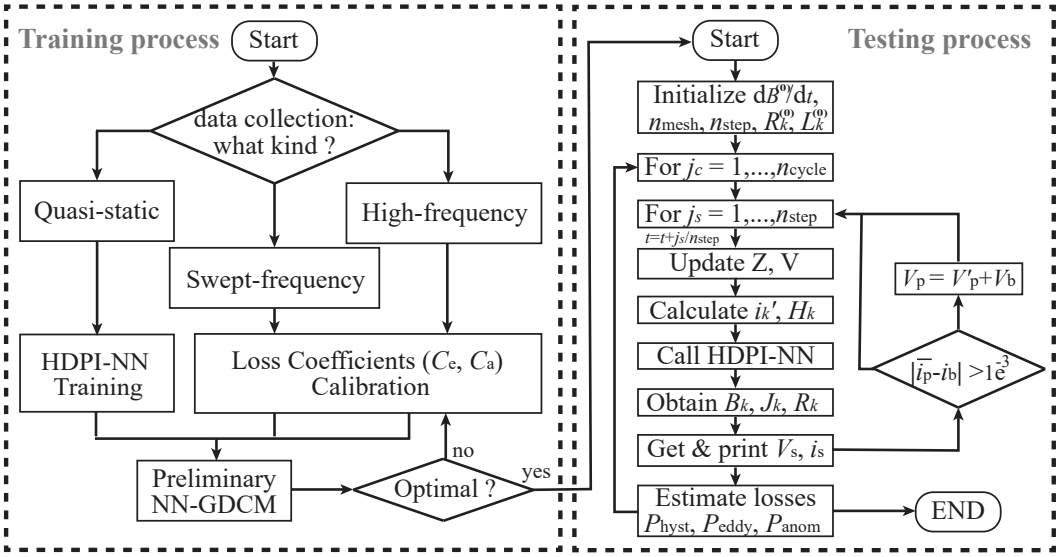

FIGURE 5.7: Flow chart of NN-GDCM.

- **Stage 1: One-Time Material Learning:**
  - **Purpose:** This stage focuses on capturing the intrinsic, dimension-independent properties of the magnetic material, which are consistent across different component sizes made of the same material.
  - **Data Used:** A limited set of quasi-static B–H loop data, primarily collected from Core A (TDK N87 ferrite) at low frequencies (e.g., 1 kHz), was used. This data is sufficient to accurately capture the material's complex, non-linear, and history-dependent magnetization behavior. This stage specifically involves training the HDPI-NN material model (as detailed in Chapter 4) only once for a given material family (e.g., N87 ferrite).

- **Advantage:** This process results in a reusable, high-fidelity material model that does not need to be retrained for other components made of the same material, drastically reducing overall data collection and training effort.

- **Stage 2: Minimal, Dimension-Specific Calibration:**
  - **Purpose:** This stage adapts the pre-trained HDPI-NN material model and the GDCM framework to a new, specific core dimension. It primarily involves tuning a small set of dynamic parameters (C_{cl}, C_a, α, etc.) that account for dimension-dependent effects (e.g., eddy currents, skin effect) not fully captured by the quasi-static material model.
  - **Data Used:** A small set of frequency-swept sinusoidal loss data, collected from Core A (TDK N87 ferrite) for initial calibration, and subsequently from Core B (TDK N87 ferrite, a different size) for testing scalability. This data allows for fitting the model's predicted loss to measured data, following core loss separation procedures outlined in [32], [106].
  - **Advantage:** This is a lightweight, targeted calibration step, not a full-scale retraining. It effectively tunes the scalable physics model to the new dimensions with minimal new data, thereby enabling efficient generalization across different core dimensions.

This two-stage strategy provides sufficient data for model training. For the subsequent validation of the NE-DCM, the test dataset includes dynamic hysteresis responses under various excitation conditions, primarily collected from Core A and Core B, spanning up to 312.5 kHz. This upper frequency limit was partly determined by the measurement equipment's bandwidth, but also aligns with typical application scenarios where core dimensions and winding structures effectively suppress high-frequency resonance effects below this range [107]. Extension of the model's applicability to higher frequencies is feasible with appropriate data and structural considerations (e.g., explicitly modeling resonance), and will be explored in future work.

For comparative analysis with purely data-driven models (as presented in Section 5.5), an external dataset from the MagNet open-source database [40], [41], [45] was also utilized.

This specifically included high-frequency data for Core C (TDK N87 ferrite TX 37/22/14) [40] from MagNet, which served as a benchmark for evaluating the NE-DCM's scalability against models trained on extensive external data.

5.5 Model Implementation and Baselines

This section details the specific implementation choices for the NE-DCM model and introduces the benchmark models used for comparative analysis.

5.5.1 The NE-DCM Implementation Details

The NE-DCM, as described in Section 5.2, integrates the HDPI-NN material model (Section 5.2.2) within the GDCM solver framework (Section 5.2.1). The implementation process follows the two-stage strategy outlined in Section 5.4.2, which fundamentally relies on the physical separation of static and dynamic loss components.

For Stage 1: One-Time Material Learning and Hysteresis Isolation, the HDPI-NN component was trained end-to-end using the Adam optimizer [96]. The training utilized 252 quasi-static B–H loops collected from Core A (TDK N87 ferrite), as described in HDPI-NN model development (Section 4.5.2). The training objective, following the methodology in [99], combined the mean squared error (MSE) between the predicted magnetic flux density $B(t)$ and the measured reference, along with the error in the predicted loop area. This setup ensures that the HDPI-NN model accurately captures the underlying static hysteresis behavior of the material rather than dynamic loss. This setup ensures that the HDPI-NN model captures the intrinsic static hysteresis characteristics of the material, rather than dynamic loss phenomena. The key hyperparameters of HDPI-NN, such as the number of hysteresis operators and the architecture of the subnetworks, were selected empirically based on the configurations presented in Chapter 4. While this empirical approach yielded satisfactory performance in this work, more systematic hyperparameter optimization frameworks (e.g., Optuna [108]) offer a promising direction for further improving model generalization and data efficiency.

Subsequently, for Stage 2: Minimal Calibration and Dynamic Loss Separation, the dynamic parameters (C_{cl}, C_a, α) for each core dimension (Core A, Core B, Core C) were determined through a minimal calibration process. This stage isolates the dynamic loss components (classical and anomalous eddy currents) by analyzing the surplus loss observed at higher frequencies compared to the quasi-static baseline. This involves fitting the model's predicted dynamic loss to a small set of frequency-swept sinusoidal loss data (as described in Section 5.4.2).

This calibration involves two main aspects:

- **Extracting Eddy Current Loss Coefficients (C_{cl} and C_e):** These coefficients are extracted from frequency-swept sinusoidal loss data (ranging from low to high frequencies), following a loss separation procedure outlined in [32], [106]. This procedure relates measured power loss to peak flux density B_p and frequency, assuming sinusoidal flux density. A common formulation used for fitting core loss under sinusoidal excitation, consistent with Bertotti's theory [23], [46], is:

$$P_{total} = P_{hyst} + 2\pi^2 C_{cl} f^2 B_p^2 + 8.764 C_a f^{1.5} B_p^{1.5}, \tag{5.15}$$

  where P_{hyst} is first approximated by extrapolating the measured core loss density curve to a very low frequency (e.g., 1 Hz), where contributions from eddy current and excess loss become negligible. The coefficients C_{cl} and C_e are then obtained by performing a least-squares fitting that minimizes the variance of the discrepancy between measured and predicted core losses under various sinusoidal operating conditions from the frequency sweep data.
- **Tuning the Empirical Inductance Variation Limiter Parameter (α):** The inductance variation limiter α (introduced in Equation (5.10), Section 5.3.3) plays a key role in maintaining numerical stability during rapid flux transitions by bounding the rate of inductance change between time steps. Its value is empirically tuned using a small yet representative subset of high-frequency primary-side voltage and current waveforms (typically 3–5 datasets). The goal is to identify a value of α that effectively suppresses spurious numerical oscillations during abrupt transients,

while preserving the fidelity of inductance dynamics. The selected value consistently enabled the NE-DCM solver to achieve over 96% waveform fitting accuracy (coefficient of determination, R^2) and kept the core loss prediction error within 10% across the evaluated cases.

The final calibrated parameters for each core and material are summarized below. For the TDK N87 material:

- Core A: $C_e = 1.64 \times 10^{-5}$, $C_a = 2.31 \times 10^{-6}$, $\alpha = 0.52$
- Core B: $C_e = 1.59 \times 10^{-5}$, $C_a = 6.73 \times 10^{-6}$, $\alpha = 0.4$
- Core C: $C_e = 1.81 \times 10^{-5}$, $C_a = 3.55 \times 10^{-6}$, $\alpha = 0.45$

For the TDK T65 material, following the same calibration workflow:

- Core A: $C_e = 2.63 \times 10^{-5}$, $C_a = 4.31 \times 10^{-8}$, $\alpha = 0.4$
- Core B: $C_e = 6.57 \times 10^{-5}$, $C_a = 1.85 \times 10^{-7}$, $\alpha = 0.2$

An observed trend was that larger cores required a higher α value. This suggests the inductance limiter may be partially compensating for dimension-dependent dynamic nuances or numerical stiffness effects that become more pronounced at larger physical scales. This minimal set of calibrated dynamic parameters, combined with the respective pre-trained HDPI-NN material model for each material, fully defines the NE-DCM for each specific core.

All relevant hyperparameters for both the training (Stage 1) and simulation (Stage 2) stages, such as the learning rate, number of cycles (n_{cycle}) and steps per cycle (n_{step}), were selected to ensure waveform resolution and simulation convergence (as discussed in Section 5.3.3). Table 5.2 summarizes these overall hyperparameters for the NE-DCM simulation.

5.5.2 Benchmark Models for Comparative Analysis

To provide a comprehensive benchmark for evaluating the NE-DCM's performance against conventional paradigms, two main types of models were prepared as baselines:

TABLE 5.2: HDPI-NN Hyperparameters and Simulation Settings

Parameter	**Value**
Number of Hysteresis Operators	30
Neurons per layer (Reversible subnetwork)	5
Batch Size (HDPI-NN)	128
Learning Rate	0.01
Number of Cycles (n_{cycle})	30
Time Steps per Cycle (n_{step})	200

- **Model-Driven Baseline (Traditional GDCM):** This baseline utilizes the same GDCM circuit structure as the proposed the NE-DCM, but it replaces the high-fidelity HDPI-NN material model with a simplified, conventional static hysteresis model (limiting Preisach model [32]). Its parameters are identified using the limiting hysteresis loop. This benchmark directly demonstrates the accuracy and generality improvements gained by integrating the neural material component.
- **Data-Driven Baseline (HARDCORE):** This model represents a purely data-driven approach, utilizing dilated convolutional neural networks [43] to predict core loss. It is crucial to note that pure data-driven models like HARDCORE typically do not support physical dimensions as explicit inputs and require extensive datasets for generalization. For comparison purposes, the HARDCORE model was trained on an extensive high-frequency dataset (over 40,000 sequences) for a single core (e.g., Core C from the MagNet database, Section 5.5.2) [43]. Its performance is evaluated by testing its ability to extrapolate and predict losses for cores with different dimensions (e.g., Core B) for which it has not seen specific data during training. This benchmark highlights the NE-DCM's superior scalability and data efficiency.

Table 5.3 outlines the strategic roles and characteristics of the three validated magnetic cores used to demonstrate the capabilities of the proposed the NE-DCM. Each core serves a distinct purpose in the evaluation framework: Core A (small, 12.5 mm OD) is used as the material learning core to capture fine-grained magnetic behavior; Core B (large, 40 mm OD) serves as the scalability test core to assess model generalization across dimentional scales; and Core C (medium, 37 mm OD) is adopted from a public dataset [40] and serves as the training core

TABLE 5.3: Benchmark Core Roles and Characteristics for Model Evaluation

Attribute	Core A	Core B	Core C
Material	TDK N87 Ferrite	TDK N87 Ferrite	TDK N87 Ferrite
Dimensions (Outer Diameter)	Small – 12.5 mm OD	Large – 40 mm OD	Medium – 37 mm OD
Data Source	Experimentally Measured (This Work)	Experimentally Measured (This Work)	Open-source Dataset [40]
Evaluation Role	Material Learning Core	Scalability Test Core	HARDCORE Training Core

for the HARDCORE baseline. This provides insight into the strategic choice of baselines for rigorously evaluating the NE-DCM's capabilities across different dimensions and data requirements.

5.6 Validation Results

This section presents the comprehensive experimental validation results for the NE-DCM, demonstrating its performance in achieving high accuracy, robust generality across diverse operating conditions, and scalability across varying component dimensions. The validation is conducted using experimental data acquired from TDK N87 ferrite toroidal cores (Core A, Core B, Core C) and, for comparative analysis, external data from the MagNet database, as detailed in Section 5.5.2. The performance of the NE-DCM is rigorously evaluated against both traditional model-driven (Traditional GDCM) and purely data-driven (HARDCORE) baselines (Section 5.6.2).

5.6.1 Evaluation Metrics

To quantitatively assess the performance of the NE-DCM and benchmark its capabilities against baselines, two primary metrics are employed, consistent with standard practices in power magnetics modeling [45]:

- **Coefficient of Determination (R^2):** This metric quantifies the goodness of fit for the primary-side current waveform prediction, measuring the correlation between the predicted waveform (i_p) and the measured waveform ($\hat{i_p}$). R^2 is calculated as:

$$R^2 = 1 - \frac{\sum_{i=1}^{N} \left(i_p(t_i) - \hat{i_p}(t_i) \right)^2}{\sum_{i=1}^{N} \left(i_p(t_i) - \bar{i_p} \right)^2}, \tag{5.16}$$

where N is the number of data points, and $\bar{i_p}$ is the mean measured current over one period. A value closer to 1 (or 100%) indicates a better fit.

- **Core Loss Error (ε_{P_v}):** This metric quantifies the relative deviation between the predicted core loss P_{pred} and the benchmark loss P_{meas}. It is calculated as:

$$\varepsilon_{P_v} = \frac{|P_{\text{pred}} - P_{\text{meas}}|}{P_{\text{meas}}} \times 100\%. \tag{5.17}$$

This metric provides a direct measure of the accuracy in estimating the energy dissipated per cycle.

5.6.2 Baseline Accuracy and Generality on the Training Core (Core A)

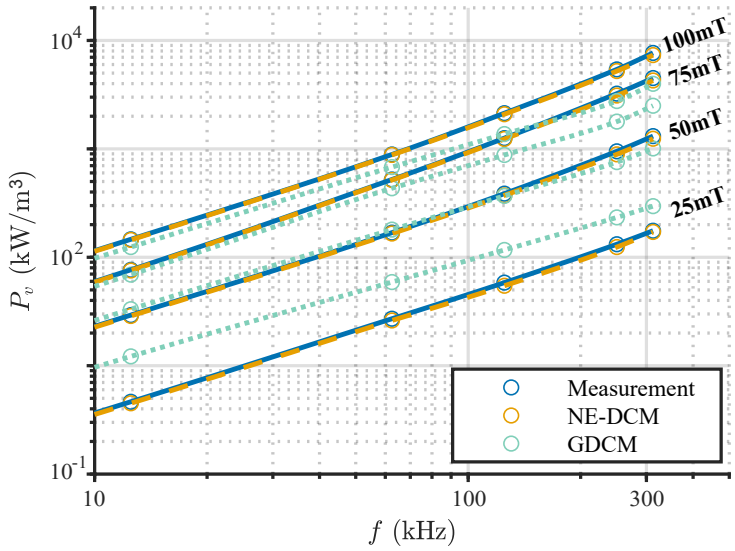

FIGURE 5.8: Baseline Accuracy on Core A: Predicted vs. Measured Core Loss.

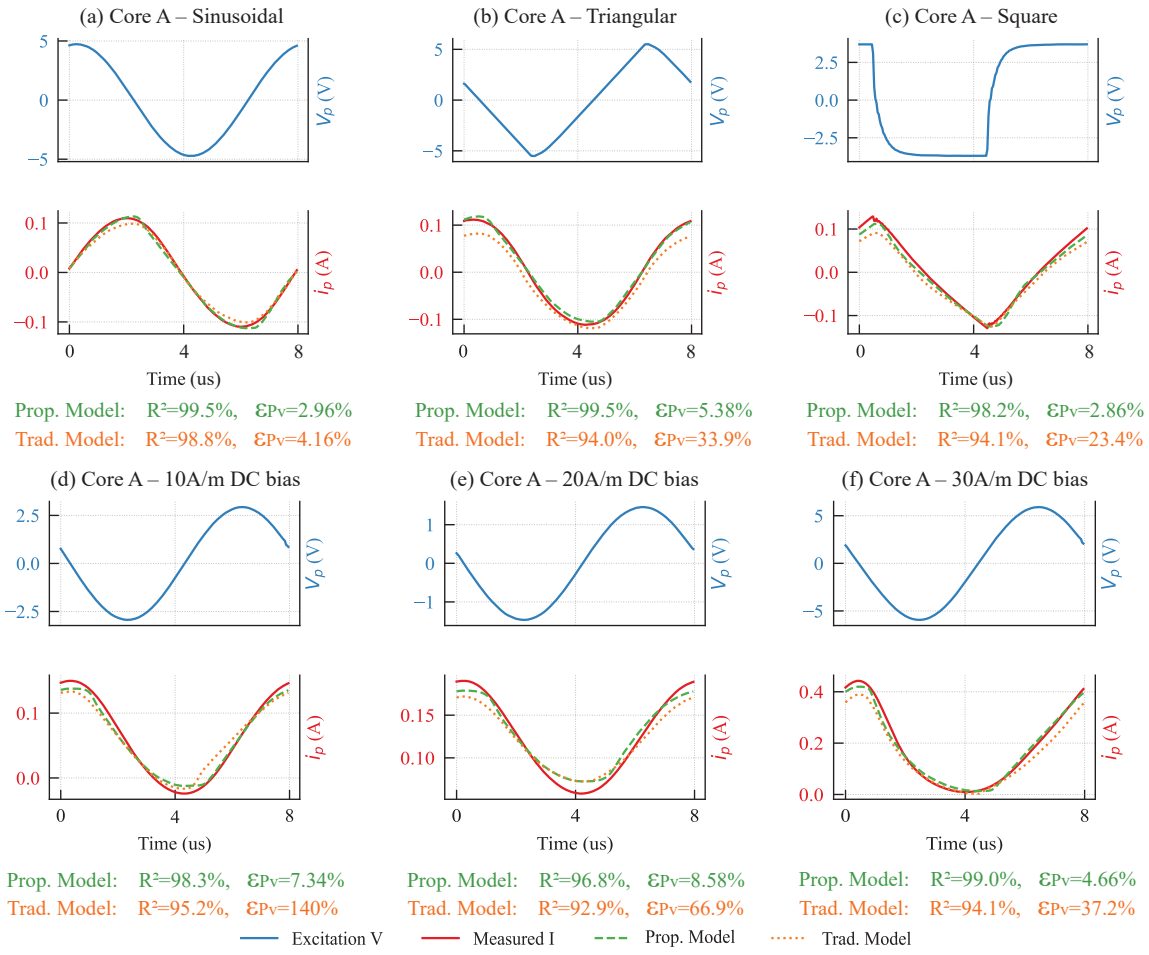

FIGURE 5.9: Validation of model accuracy and generality on Core A under various 125 kHz voltage excitations.

This subsection establishes the fundamental accuracy and generality of the NE-DCM on Core A (TDK N87 ferrite), which was used for the one-time material learning (HDPI-NN training) and initial dynamic calibration. This serves as a baseline performance assessment before evaluating scalability to unseen dimensions.

Figure 5.8 presents the core loss versus frequency for Core A under sinusoidal excitation, comparing the NE-DCM's predictions with experimental measurements and the Traditional GDCM baseline. As illustrated, the NE-DCM's predictions align closely with the experimental measurements across the entire frequency range, significantly outperforming the Traditional

GDCM. This confirms that replacing the conventional static hysteresis model with the HDPI-NN within the GDCM framework leads to a substantial improvement in baseline prediction accuracy.

Figure 5.9 demonstrates the NE-DCM's robustness and generality on Core A under a wide variety of 125 kHz excitations, including standard waveforms (sinusoidal, triangular, square) and increasing DC bias levels. For all tested waveforms, the NE-DCM consistently achieves a high R^2 or the primary-side current waveform prediction (e.g., above 98% for most cases) and a low ε_{P_v} (typically below 9%). Specifically, under the 30A/m DC bias condition, the NE-DCM's core loss error is 4.66%, representing an 8-fold reduction in prediction error compared to the Traditional GDCM (37.2%). This robust performance validates the generality provided by the history-dependent HDPI-NN component.

5.6.3 Scalability Across Unseen Dimensions (Cores B & C)

This subsection presents the definitive test of the NE-DCM's scalability: its ability to accurately predict performance on new, unseen core dimensions (Core B and Core C) with only minimal dynamic parameter calibration and without retraining the HDPI-NN material model. The validation is twofold: first, we assess the model's ability to scale its prediction of time-domain V-I behavior, and second, we conduct a head-to-head comparison of its scalar core loss prediction scalability against a purely data-driven baseline.

The model's fundamental capability to predict terminal V-I characteristics is a prerequisite for its use in circuit simulations. Figure 5.10 demonstrates the NE-DCM's scalability for time-domain V-I behavior under various complex excitations on both Core B and Core C. For these new, unseen cores, the NE-DCM's predicted current waveforms align closely with the experimental measurements. The coefficient of determination (R^2) for these predictions consistently remains high (above 0.96), indicating a strong correlation in both waveform shape and magnitude. This confirms that the model's underlying physics, which govern the dynamic relationship between flux, field, and terminal quantities, scale robustly and correctly with the core's physical dimensions. The traditional GDCM, while structurally scalable,

shows significant deviations due to its simplified material model, highlighting the critical role of the embedded high-fidelity HDPI-NN.

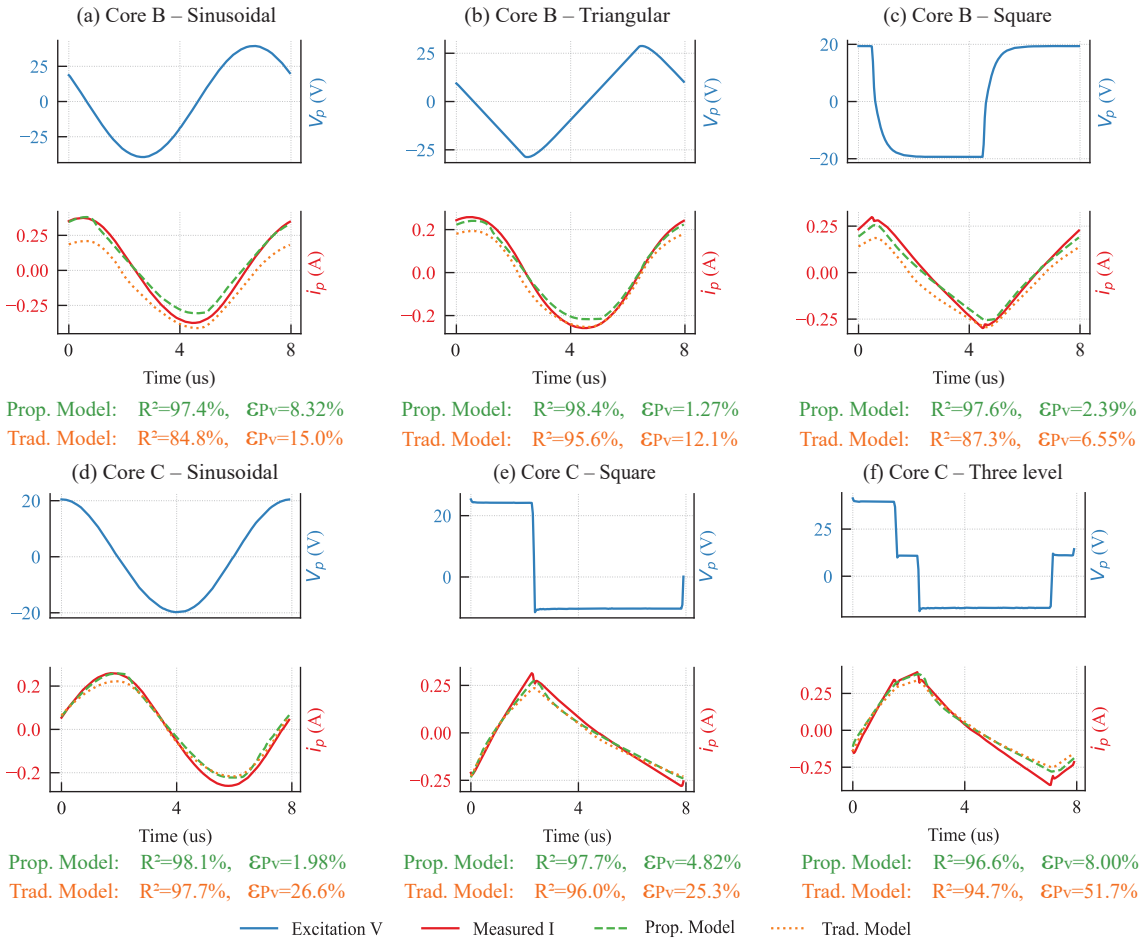

FIGURE 5.10: Demonstration of model scalability. Prediction results for Core B (top row) and Core C (bottom row) under various 125 kHz voltage excitations.

The statistical results presented in Table 5.4 further confirm the robust scalability of the NE-DCM. Even for Cores B and C, which were not seen during the material learning stage, the model maintains a MAPE below 6% and an R^2 above 97% across diverse excitations. This quantitative evidence demonstrates that the integrated physics-based solver effectively handles dimensional scaling, while the neural material law generalizes accurately to different cross-sectional dimensions.

TABLE 5.4: Statistical performance summary of the NE-DCM for unseen core dimensions (Cores B and C).

Test Core	**Waveform Accuracy**	**Core Loss Error** (ε_{P_v})		
	Avg. R^2 **(%)**	**MAPE (%)**	**95% APE (%)**	**Max. Error (%)**
Core B (Large)	97.4	5.38	8.85	11.20
Core C (Medium)	98.1	6.25	10.42	15.60
Overall	**97.8**	**5.82**	**9.64**	**13.40**

Note: The statistical metrics are derived from the comparison between NE-DCM predictions and experimental measurements across 10–312.5 kHz and 25–100 mT.

Building upon the demonstrated waveform accuracy, we performed a direct head-to-head comparison of scalar core loss prediction to further probe the architectural advantages of the NEP paradigm. A rigorous test was designed using Core B, a significantly larger core unseen by either model's training process. The NE-DCM, with its material model trained on the small Core A, was benchmarked against the purely data-driven HARDCORE model, which was trained on an extensive dataset from the medium-sized Core C.

The results of this scalability test, presented in Figure 5.11 , are revealing. The NE-DCM's predictions align closely with the experimental measurements across the entire frequency range, with the core loss prediction error (ε_{P_v}) remaining below 10%. In sharp contrast, the HARDCORE model exhibits a significant and systematic deviation, particularly at lower frequencies.

This pronounced failure of the HARDCORE model raises a critical question: does it stem from a general inaccuracy of the model, or a more fundamental, architectural limitation? To definitively isolate the failure mode, a control experiment was performed to evaluate the HARDCORE model's baseline accuracy on its own training data, Core C. As shown in Figure 5.12, the HARDCORE model demonstrates high fidelity when predicting losses for the core it was trained on, confirming its capability to accurately learn from the data it has seen.

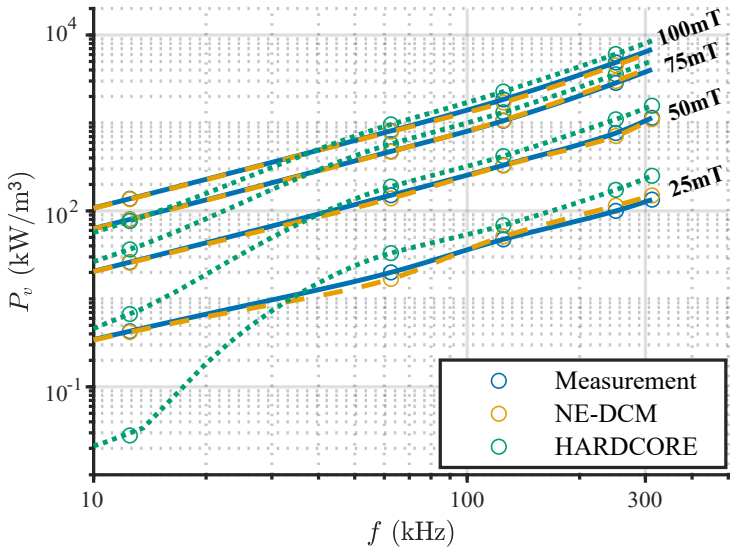

FIGURE 5.11: Core loss vs. frequency comparison on Core B (NE-DCM vs. HARDCORE).

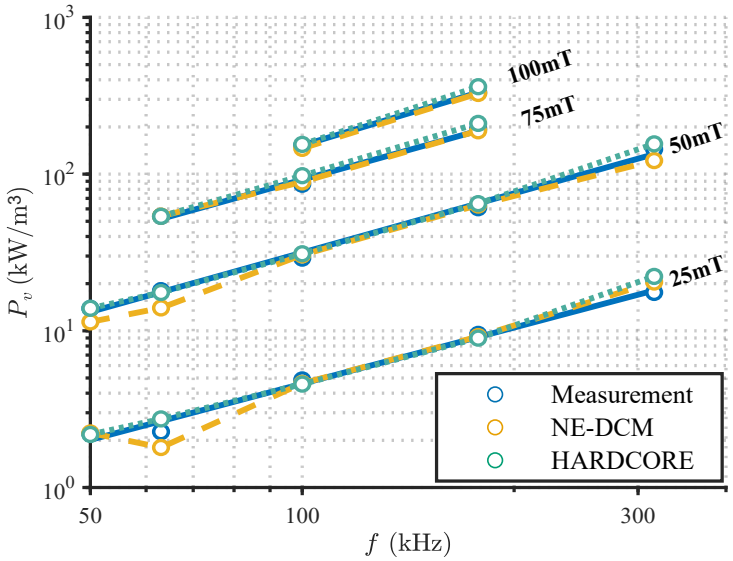

FIGURE 5.12: Core loss vs. frequency comparison on Core C (NE-DCM vs. HARDCORE).

By comparing the results of Figure 5.11 and Figure 5.12 provides a definitive conclusion. The catastrophic failure of HARDCORE on the unseen Core B, given its proven accuracy on its training Core C, is not a simple matter of model inaccuracy. It is a fundamental failure of scalability. Lacking an architectural interface for physical dimensions, the purely data-driven model is structurally incapable of understanding that Core B is a different size from Core C.

It merely processes a similar input waveform and produces a similar output, failing to account for the dimensional scaling of dynamic effects.

In conclusion, the combined evidence from both time-domain waveforms (Figure 5.10) and scalar loss predictions (Figure 5.11 and Figure 5.12) powerfully validates the scalability of the NE-DCM. This success is directly attributable to the NEP paradigm, where a physically-structured, decoupled architecture is uniquely capable of providing the robust dimensional scalability required for practical engineering design.

5.6.4 Material Extensibility and High Non-linearity Validation

Having established the NE-DCM's accuracy, generality, and dimensional scalability on a single material (TDK N87), this section pushes the validation to its conceptual limits. We address two critical questions that determine the true viability of the NEP paradigm as a universal framework: 1) Is the entire modeling workflow extensible to a distinctly new magnetic material? 2) Does the model remain robust when pushed into the highly non-linear regime of magnetic saturation?

A. Material Extensibility: A Complete Workflow Validation on TDK T65

The central claim of the NEP paradigm is that its data-efficient, two-stage workflow is a generalizable and portable methodology, not just a procedure tailored for one material. To verify this, we selected TDK T65 ferrite, a material specifically chosen for its contrasting properties compared to TDK N87. As illustrated in Figure 5.13, T65 exhibits a narrower quasi-static hysteresis loop but a more significant widening at high frequencies, indicating different loss mechanisms and a greater sensitivity to frequency. This makes it an excellent and challenging test case for material extensibility.

To conduct the validation, we rigorously replicated the exact two-stage workflow established for N87, using T65 cores with dimensions identical to the original Core A and Core B:

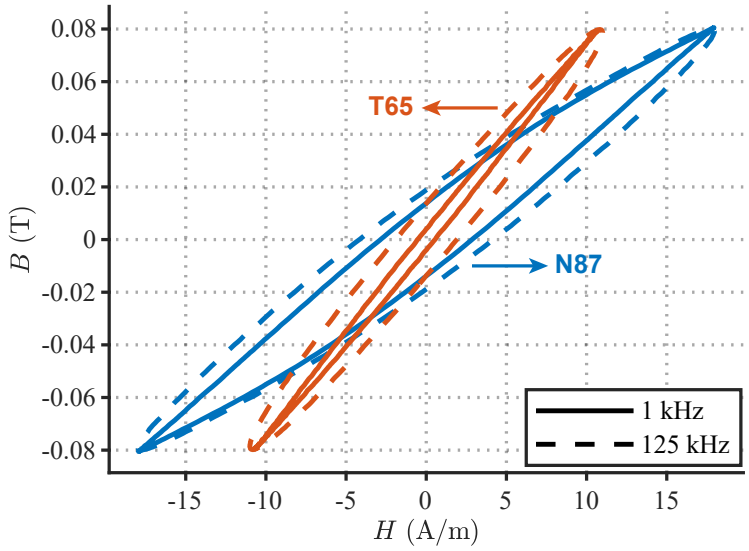

FIGURE 5.13: Comparison of dynamic B–H loops for TDK N87 and TDK T65 ferrite materials at a peak flux density of 0.08 T.

1. **Stage 1 (Material Learning):** A new, material-specific HDPI-NN model for T65 was trained only once using 260 quasi-static (1 kHz) B–H loops collected from the small "T65-Core A".
2. **Stage 2 (Minimal Calibration):** The dimension-dependent dynamic parameters (C_e, C_a) were then calibrated for both the small "T65-Core A" and the large "T65-Core B" using a small set of sinusoidal loss data for each core.

The results compellingly demonstrate the portability and effectiveness of the framework on this new material. First, we validated the model's baseline accuracy and generality on its training core, T65-Core A. As shown in Figure 5.14, the model's time-domain V-I predictions for T65-Core A under a wide variety of arbitrary and biased 125 kHz excitations align closely with the experimental measurements. The coefficient of determination (R^2) consistently remains high (above 98%) across all complex waveforms, confirming the success of the material learning stage.

Most importantly, the model's scalability was then tested on the unseen, larger "T65-Core B" without retraining the T65-specific neural network. Figure 5.15 presents the V-I prediction results for this larger core. The model again maintains a high degree of accuracy, with R^2 values consistently exceeding 93% for all tested excitations. This successful scaling to a

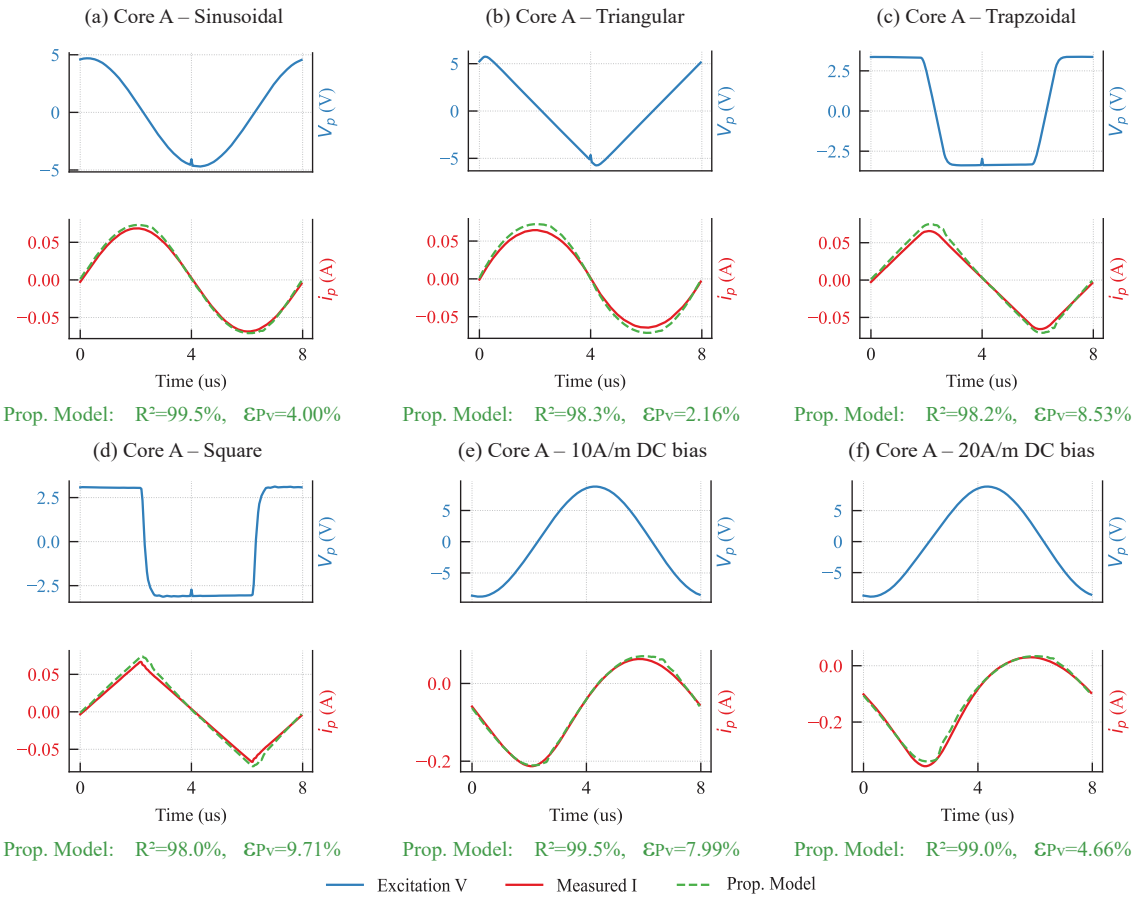

FIGURE 5.14: Validation of the NE-DCM's accuracy and generality on the T65 training core (T65-Core A) under various 125 kHz voltage excitations. The waveforms shown are: (a) sinusoidal, (b) triangular, (c) trapezoidal, (d) square, (e) 10 A/m DC bias, and (f) 20 A/m DC bias.

new dimension on a new material provides powerful evidence that the NEP paradigm and its associated workflow constitute a truly generalizable and portable framework for magnetic core loss modeling.

B. Robustness at the Onset of High-Frequency Saturation To further probe the model's limits and assess its fidelity in the most critical non-linear operating region, we tested its performance at the onset of high-frequency saturation. This regime is paramount for practical design, as engineers often push components close to saturation to maximize performance, where even small prediction errors can lead to catastrophic failure.

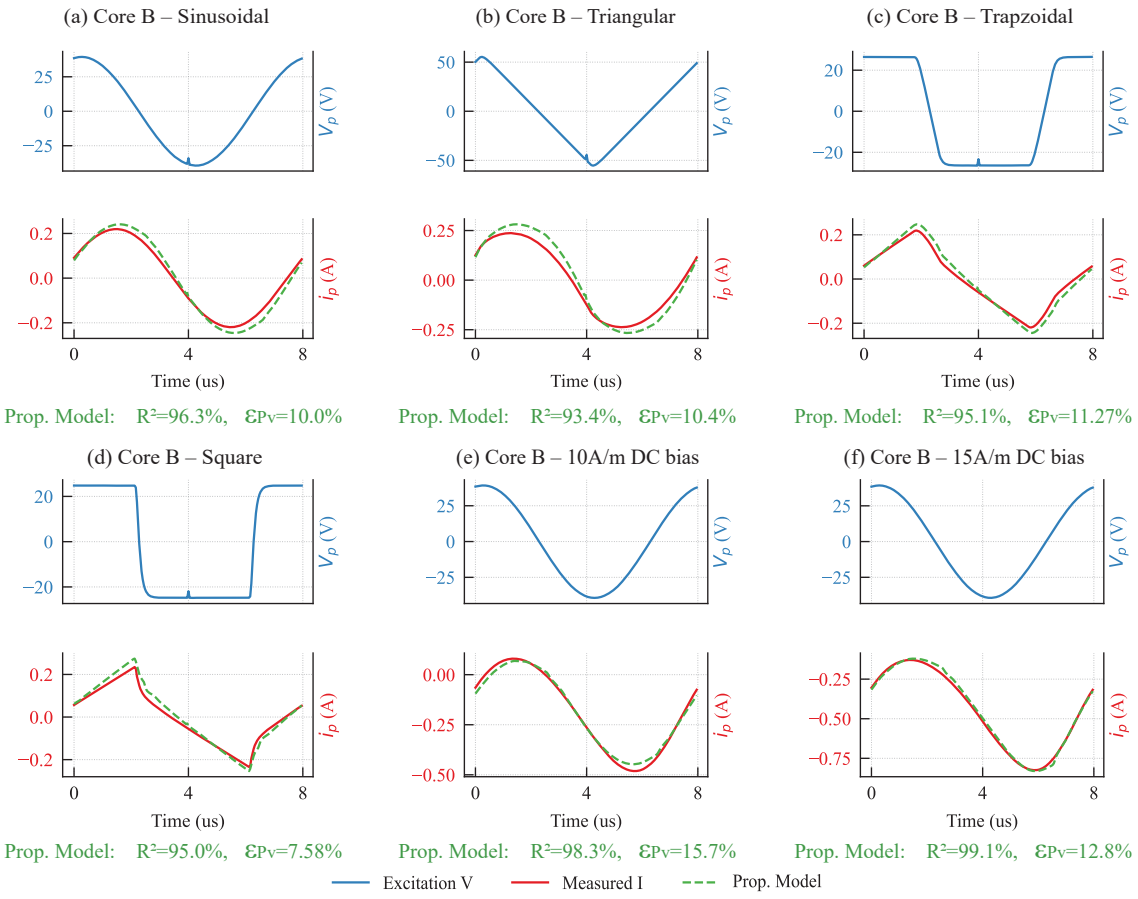

FIGURE 5.15: Demonstration of the NE-DCM's scalability for the T65 material on the unseen, larger (T65-Core B) under various 125 kHz voltage excitations. The waveforms shown are: (a) sinusoidal, (b) triangular, (c) trapezoidal, (d) square, (e) 10 A/m DC bias, and (f) 15 A/m DC bias.

For this test, a 125 kHz sinusoidal voltage excitation was applied to the T65-Core A with progressively increasing amplitude. This drove the core's peak flux density from the linear region (B_p = 0.1 T) towards the onset of saturation at 0.3 T.

The results are presented in Figure 5.16. As the flux density increases, the measured current waveform becomes severely distorted, exhibiting the sharp, non-linear peaks characteristic of a saturating core. The NE-DCM's predictions remarkably capture this highly distorted behavior across all stages. The model accurately matches not only the shape and amplitude of the current spikes but also their precise timing relative to the voltage excitation. With R^2 values remaining above 98% even deep into the non-linear region, this result powerfully demonstrates the model's robustness and high fidelity. It validates the ability of the embedded HDPI-NN to

represent the material's strong non-linearity and the capability of the overall the NE-DCM framework to simulate these extreme dynamics accurately. This provides confidence in the model's utility for predicting component behavior under aggressive operating conditions and for safe design margin analysis.

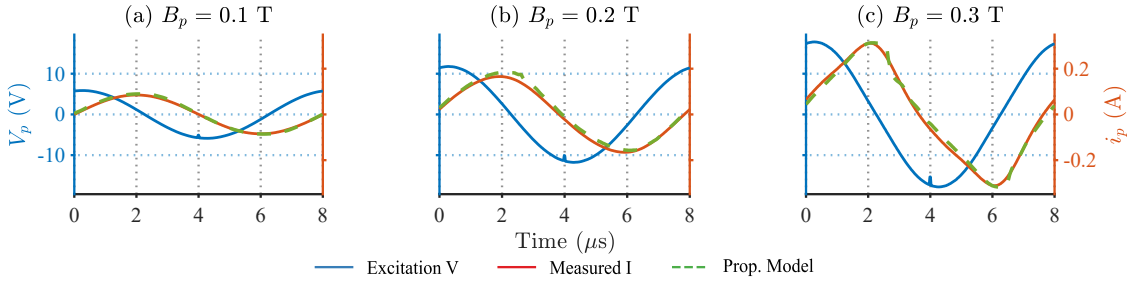

FIGURE 5.16: Validation of the NE-DCM's performance and robustness at the onset of high-frequency saturation on T65-Core A, corresponding to peak flux densities of: (a) 0.1 T (linear region), (b) 0.2 T, and (c) 0.3 T (onset of saturation).

5.6.5 Discussion of Performance Characteristics

The validation results comprehensively demonstrate that the NE-DCM achieves its objectives of accuracy, generality, and scalability. The NEP paradigm successfully resolves the accuracy-scalability trade-off inherent in conventional models. The model's ability to accurately predict material behavior under arbitrary excitations, combined with its robust scalability across different core dimensions, positions it as a powerful tool for power magnetics design.

- **Accuracy and Generality:** the NE-DCM consistently achieves high accuracy for primary-side current waveforms and core loss across a wide range of arbitrary and biased excitations. The integration of the HDPI-NN ensures the material's complex, history-dependent behavior is faithfully captured, as validated in Chapter 4.
- **Scalability and Data Efficiency:** A primary advantage is its robust scalability to new, unseen core dimensions with minimal data. The two-stage modeling workflow (Section 5.4.2) is inherently data-efficient: the HDPI-NN is trained only once on quasi-static data, and dimension-specific adaptation requires only minimal dynamic

parameter calibration. This significantly reduces the experimental and computational cost associated with evaluating multiple core sizes in a design cycle.

- **Physical Interpretability:** By design, the NE-DCM's architecture incorporates electromagnetic field information (via the GDCM) and physically inspired material modeling (via HDPI-NN). This allows for a higher degree of physical interpretability compared to purely data-driven models, potentially facilitating integration with existing field simulation software/tools and guiding magnetic component design.

In summary, the rigorous experimental validation confirms the effectiveness of the NE-DCM. By successfully leveraging the NEP paradigm, the NE-DCM achieves high accuracy, robust scalability, and broad generality for core loss prediction across a wide range of operating conditions and varying component dimensions. Its data-efficient two-stage modeling workflow further enhances its practicality. These results establish the NE-DCM as a comprehensive and highly applicable tool for the design and optimization of power magnetics, demonstrating a significant advancement in the field.

5.7 Discussion and Summary

This section provides a concise summary and discussion of the key findings from the experimental validation of the NE-DCM, as presented in Section 5.6. It synthesizes how the NE-DCM, built upon the NEP paradigm, addresses the overarching research objective of achieving accurate, scalable, and generalizable core loss modeling.

The rigorous experimental validation confirms the effectiveness of the NE-DCM for core loss prediction across a wide range of operating conditions and varying component dimensions. The NE-DCM achieves high accuracy in both primary-side current waveform prediction and core loss estimation (Section 5.6.2), consistently aligning with experimental measurements under diverse excitations including sinusoidal, triangular, square, and DC-biased waveforms. This high fidelity is maintained even in the critical, highly non-linear regime at the onset of high-frequency saturation (Section 5.6.4), where the model robustly captures severe current distortion. This capability directly benefits from the high-fidelity material behavior modeling

achieved by the embedded HDPI-NN (Chapter 4), which captures intricate, history-dependent magnetization.

A primary contribution of the NE-DCM is its demonstrated robust scalability. This was validated on two crucial fronts: dimensional scalability and material extensibility.

First, the model shows exceptional dimensional scalability to new, unseen core dimensions (Section 5.6.3). Unlike purely data-driven models, the NE-DCM successfully predicts core loss for different core sizes (Core B and Core C) with only minimal, dimension-specific calibration. Crucially, our diagnostic analysis (Figure 5.11-5.12) revealed that the failure of the data-driven baseline was not one of general inaccuracy, but a fundamental, architectural inability to scale, a limitation directly overcome by our NEP paradigm. This dimensional scalability stems from the data-efficient two-stage modeling workflow, where the HDPI-NN is trained once on quasi-static material data, and the GDCM handles dimension dependence, significantly reducing the experimental and computational cost in a design cycle.

Second, the framework demonstrates powerful material extensibility. The entire two-stage workflow was successfully replicated on a distinctly different material, TDK T65, yielding similarly high accuracy and scalability (Section 5.6.4). This powerful result confirms that the proposed approach is not a material-specific solution but a portable and generalizable methodology, further enhancing its practical value.

Furthermore, the NE-DCM inherently offers physical interpretability (Section 5.2). Its architecture, which integrates a physics-based dynamic solver (GDCM, Section 5.2.1) and a physically-informed neural material model (HDPI-NN, Section 5.2.2), directly aligns with the fundamental principles of electromagnetism and magnetization mechanisms (Chapter 2). This structural grounding contrasts with the black-box nature of many pure data-driven models, providing clearer insights into the model's behavior and offering potential for seamless integration with existing field simulation software/tools. As a natural extension, future work may explore incorporating field-distribution-related quantities, such as local magnetic flux density or spatial gradients—explicitly into the NE-DCM architecture. This could further

enhance spatial awareness and improve compatibility with multi-physics solvers that require detailed local field information.

In summary, the NE-DCM successfully leverages the NEP paradigm to overcome the fundamental trade-offs inherent in conventional core loss modeling approaches. By synergistically combining a scalable physics solver with a high-fidelity neural material model, the NE-DCM effectively delivers high accuracy, robust scalability, and broad generality for core loss prediction, all within a data-efficient workflow. These results position the NE-DCM as a comprehensive and highly applicable tool, representing a significant advancement towards efficient design and optimization of power magnetics. More broadly, this work provides a methodological blueprint for developing hybrid physics-AI models, demonstrating how principled decomposition can unlock solutions to complex engineering problems.

CHAPTER 6

Discussion and Analysis of the Developed Hybrid Modeling Strategies

---

This chapter provides a comprehensive discussion and analysis of the research findings presented in Chapter 3, 5, and 5. It synthesizes the performance of the developed hybrid models, demonstrating their individual strengths and how they collectively form a progressive, complementary solution to the grand challenge of accurate, scalable, and generalizable core loss modeling. This discussion aims to highlight the unique contributions of each model and their collective impact on advancing the state of the art by systematically addressing the inherent trade-offs in conventional modeling paradigms.

6.1 Synthesis of Developed Model Performance

This section summarizes the key performance highlights of each developed model (the MMINN, the HDPI-NN, and the NE-DCM), as presented in their respective validation chapters (Chapter 3, 5, and 5). The aim is to provide a concise overview of each model's specific focus and primary achievements before a more detailed comparative analysis.

- **The MMINN Performance Summary:**
  - The MMINN, introduced in Chapter 3, demonstrated satisfactory accuracy for core loss estimation and dynamic hysteresis loop prediction. For N87 ferrite under steady-state, high-frequency, symmetric waveforms, the average relative core loss error was 2.16%, with a 95% percentile error within (-3.7%, 4.6%) (Figure 3.5). Visually, predicted $\mathbf{B}$–$\mathbf{H}$ loops showed a good match with measurements across different frequencies and temperatures (Figure 3.4).
  - The MMINN exhibited particular strengths in data efficiency and memory requirements. It achieved comparable accuracy with significantly less training data and fewer model parameters than other complex neural network models, resulting in a much smaller memory footprint (e.g., memory reduced by over 26 times, file size 7kb vs 147kb, for N49 ferrite compared to Transformer-based model; Table 3.2).

- Its mechanism-inspired architecture, separating hysteresis and dynamic components, provided a degree of physical interpretability.

- **The HDPI-NN Performance Summary:**
  - The HDPI-NN, developed in Chapter 4, achieved high accuracy in modeling complex, history-dependent material behavior and core loss prediction. For silicon steel B35A270 and N87 ferrite under arbitrary quasi-static excitations, including DC bias and various harmonics, the HDPI-NN demonstrated excellent $\mathbf{B}$–$\mathbf{H}$ loop prediction (e.g., H prediction R^2 above 96%) and low core loss error (e.g., MAPE core loss error around 5-8% for silicon steel) (Chapter 4, Section 4.6.3, Table 4.5).
  - Its key strength was the successful integration of reversible magnetization and explicit memory mechanisms within a generalized operator framework, enabling superior generality for complex material responses (Figures 4.8, 4.9).
  - The HDPI-NN also showed data efficiency for its specific task of material characterization, achieving high accuracy with a relatively smaller dataset compared to purely data-driven models (Chapter 4, Section 4.6).
- **NE-DCM Performance Summary:**
  - The NE-DCM, presented in Chapter 5, demonstrated comprehensive capabilities in accuracy, robust scalability, and broad generality for core loss prediction across varying component dimensions and arbitrary high-frequency excitations. Validation on TDK N87 ferrite cores showed consistent high accuracy (e.g., current waveform R^2 above 96%, core loss error below 10%) across diverse waveforms and different core sizes (Chapter 5, Section 5.6, Figure 5.9, 5.10).
  - Its unique two-stage modeling workflow enabled data efficiency for new dimensions, requiring only minimal calibration after one-time material learning (Section 5.4.2).
  - The NE-DCM successfully implemented the Neural-Enhanced Physics paradigm, integrating a scalable physics solver with a high-fidelity neural material model, thus bridging the accuracy-scalability trade-off.

6.2 Comparative Analysis of Hybrid Models and Existing Approaches

This section provides a direct comparative analysis of the developed hybrid models against each other (where meaningful) and against the benchmark models (traditional model-driven and purely data-driven approaches) reviewed in Chapter 2. This comparison draws upon the detailed validation results from Chapter 3, 4, and 5 to highlight the specific advantages of the proposed strategies.

- **MMINN vs. Pure Data-Driven Models (Transformer-Based and LSTM-FNN):**
  - **Context:** Comparison for steady-state, high-frequency, symmetric excitations on N49 and 3C95 ferrite (Chapter 3, Section 3.5.3).
  - **MMINN vs Transformer-Based Specifics:** For N49 ferrite, the MMINN achieved an average absolute relative error of 13.88% with 200 data points, while the Transformer model required 5000 data points. Its memory footprint was over 26 times smaller than the Transformer model (Table 4.5). Figure 3.6 illustrates the MMINN's narrower error distribution for N49 ferrite compared to the Transformer model.
  - **MMINN vs. LSTM-FNN Specifics:** For 3C95 ferrite, the MMINN showed comparable accuracy (average absolute error 1.81% vs 1.61%) and prediction speed (0.2ms vs 0.13ms) to the LSTM-FNN model, but with substantially fewer parameters (1086 vs 90654) and lower memory (Table 3.3). The LSTM-FNN typically required a much larger base dataset for fine-tuning. Figure 3.7 further highlights the MMINN's comparable error distribution for 3C95 ferrite against the LSTM-FNN model. While the MMINN's prediction time is slightly slower due to its vector ($\mathbf{B}$–$\mathbf{H}$ loop sequence) prediction nature versus LSTM-FNN's scalar (core loss) output, the MMINN's ability to predict the full dynamic hysteresis loop provides wider application scenarios beyond scalar loss calculation, such as anomaly detection.
- **HDPI-NN vs. Baselines (MMINN, Traditional Physics Models):**

- **Context:** Comparison for complex, arbitrary quasi-static excitations (silicon steel B35A270 and N87 ferrite) (Chapter 4, Section 4.6).
- **Summary:** The HDPI-NN demonstrated superior accuracy and generality for modeling history-dependent behavior (DC bias, harmonics, minor loops) compared to simpler physics-guided neural networks like the MMINN. For silicon steel, the HDPI-NN achieved significantly higher H prediction R^2 (e.g., 96.0% vs 27.63%) and lower core loss MAPE (e.g., 5.58% vs 16.57%) under DC-biased conditions compared to the MMINN (Table 4.4). This underscores the importance of explicit memory mechanisms and improved reversible magnetization modeling. the HDPI-NN also surpassed traditional physics-based models that often struggle with arbitrary excitations and complex minor loops due to simplified assumptions (Section 2.2.3). Figures 4.8 and 4.9 visually demonstrate the HDPI-NN's ability to accurately capture intricate $\mathbf{B}$–$\mathbf{H}$ loops under DC bias and harmonic excitations, respectively, compared to the MMINN.

- **NE-DCM vs. Baselines (Traditional GDCM, Pure Data-Driven HARDCORE):**
  - **Context:** Comprehensive validation for accuracy, generality, and scalability across different core dimensions (TDK N87 ferrite: Core A, B, C) under arbitrary high-frequency excitations (Chapter 5, Section 5.6).
  - **Summary:** The NE-DCM consistently achieved high accuracy (low ϵ_{P_v}, high R^2) across all tested conditions and core sizes (Figure 5.9, Figure 5.10). It significantly outperformed the Traditional GDCM baseline (Chapter 5, Figure 5.8, 5.9) due to its high-fidelity neural material model, which addresses the fundamental limitation of simplified material laws in traditional dynamic models. Crucially, the NE-DCM demonstrated robust scalability to unseen core dimensions (Core B, C) with only minimal, dimension-specific calibration, a capability where the purely data-driven HARDCORE model failed to generalize effectively (Figure 5.11), despite HARDCORE being trained on extensive external data. This rigorous comparison highlights the NE-DCM's superior overall data efficiency for the design cycle and its success in bridging the accuracy-scalability trade-off.

6.3 Analysis of Physics-Neural Network Integration Strategies

This section delves deeper into the architectural and methodological choices made in developing the hybrid models, analyzing why each integration strategy was effective and how it contributed to addressing the research objectives. This analysis connects the empirical results from previous sections back to the theoretical underpinnings of the physics-neural network fusion.

- **Mechanism-Inspired Structure (the MMINN):**
  - **Strategy:** The MMINN (Chapter 3) adopted a strategy of directly mapping the conceptual decomposition of the magnetic field (H) into hysteresis (H_h) ande dynmaic (H_{dyn}) components (Equation 3.1) onto a neural network architecture with separate subnetworks. The Hysteresis Subnetwork was inspired by the PI model, and the Dynamic Subnetwork by the ladder network segmentation (Figure 3.2).
  - **Effectiveness Analysis:** This mechanism-inspired structure contributed significantly to the MMINN's data efficiency and memory requirements. By providing the neural network with a pre-structured understanding of the problem's components, the network had a reduced search space for parameters, leading to faster training and smaller model sizes. It also offered a degree of physical interpretability by aligning the subnetworks with distinct physical phenomena, such as domain wall motion and rotation—through embedded PI model. This alignment provides a meaningful abstraction of the underlying magnetization processes, offering a key advantage over purely black-box data-driven models.
  - **Limitations & Insights:** While effective for its intended scope (steady-state, symmetric excitations), the MMINN's performance for more complex, history-dependent waveforms revealed limitations, motivating the development of the HDPI-NN. This highlighted that while general physical inspiration is beneficial, deeper physical incorporation might be needed for intricate behaviors.

- **Physics-Informed Material Modeling (the HDPI-NN):**
  - **Strategy:** The HDPI-NN (Chapter 4) pursued a strategy of creating a high-fidelity, physically-informed neural material model. This involved enhancing the classical PI operator framework by explicitly integrating reversible magnetization (inspired by J-A concepts) and explicit memory mechanisms (Section 4.2), and then parameterizing this generalized operator with a neural network.
  - **Effectiveness Analysis:** This approach proved highly effective in achieving high accuracy and generality for modeling complex, history-dependent $\mathbf{B}$–$\mathbf{H}$ loops under arbitrary quasi-static excitations (DC bias, harmonics, minor loops) (Section 4.6.3). The physical grounding allowed the HDPI-NN to capture subtle magnetization dynamics (e.g., water-drop shapes under DC bias, intricate minor loops) more faithfully than models lacking such explicit mechanisms. The neural network's role was to learn the complex, data-dependent operator distributions, which would be challenging to define analytically. This combination contributed to its data efficiency for material characterization.
  - **Limitations & Insights:** While the HDPI-NN significantly advanced material modeling accuracy and generality for quasi-static conditions, it did not inherently incorporate dynamic effects (like eddy currents) or explicitly address the influence of component geometry. These phenomena become critical at higher operating frequencies and for component-level design, indicating a need for integration with a physics-based dynamic framework to achieve comprehensive and scalable modeling.
- **The NEP Paradigm (the NE-DCM):**
  - **Context:** The NE-DCM (Chapter 5) embodies the NEP paradigm, which proposes a principled decomposition of the core loss modeling problem. It assigns the task of handling scalable dynamic effects and component geometry to a physics-based solver (GDCM, Section 5.2.1) and the task of providing high-fidelity, non-linear, history-dependent material behavior to a neural network (the HDPI-NN, Section 5.2.2). This results in an embedded architecture where

the HDPI-NN serves as the core material law within the GDCM framework (Figure 5.1).

- **Effectiveness Analysis:** This paradigm successfully addresses the fundamental accuracy-scalability trade-off observed in traditional Model-Driven and Data-Driven approaches (Figure 1.4, Table 2.2). By leveraging GDCM's inherent scalability and the HDPI-NN's high accuracy for arbitrary material responses, the NE-DCM achieved simultaneous high accuracy, robust scalability to unseen dimensions, and broad generality (Section 5.6.3). The two-stage modeling workflow (Section 5.4.2) is critical to its overall data efficiency, as the complex material model is trained only once on quasi-static data, and dimension-specific adaptation requires minimal dynamic parameter calibration.

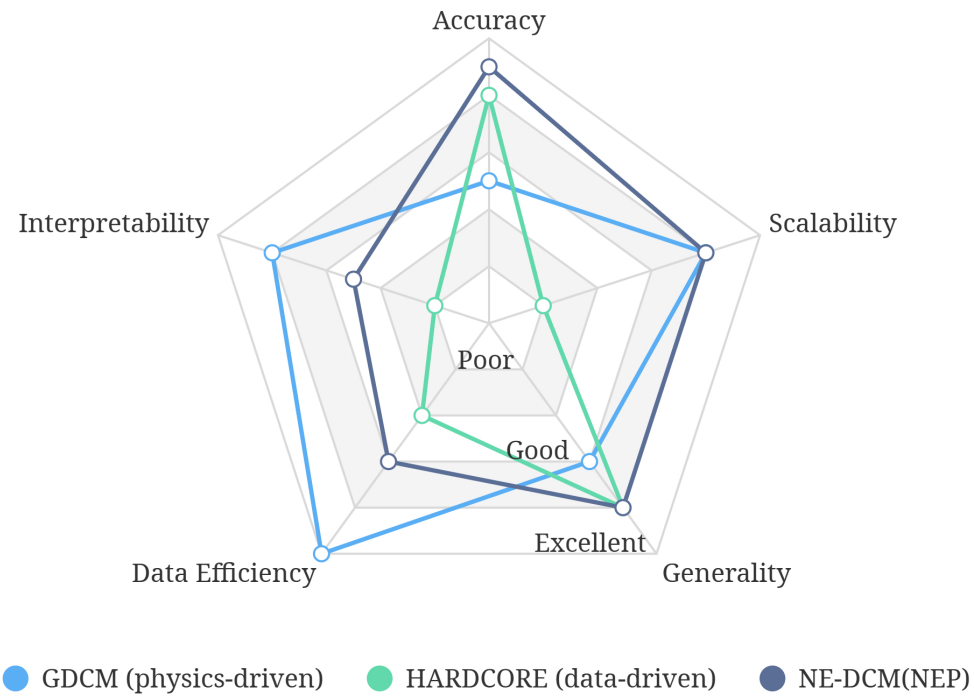

FIGURE 6.1: Performance comparison radar chart (NE-DCM vs. Baselines).

- **Illustrative Comparison:** Figure 6.1 visually illustrates how the NE-DCM, representing the NEP paradigm, pushes the "performance polygon" outward

compared to both traditional physics-based models and pure data-driven models across the dimensions of accuracy, scalability, generality, and data efficiency.

6.4 Complementarity and Overall Contribution

This section discusses how the three models (the MMINN, the HDPI-NN, and the NE-DCM), while distinct in their specific focus and application scenarios, represent a deliberate and progressive exploration of hybrid physics-neural network strategies. They collectively contribute to the overarching research objective by systematically overcoming the limitations identified at each stage of the problem decomposition, thereby offering a comprehensive solution to the multifaceted challenge of core loss modeling.

- **MMINN (Chapter 3):** *Core Application Focus: Rapid, data-light estimation for standard high-frequency steady-state scenarios.*

  The MMINN serves as a highly efficient solution for routine factory testing and fast design iterations where excitations are periodic and symmetric. By embedding loss separation principles into a compact architecture, it achieves competitive accuracy with minimal memory footprint. Its practical utility is demonstrated through its award-winning performance in the 2023 IEEE PELS-Google-Enphase MagNet Challenge [72], a global competition designed to foster innovation in magnetic component modeling. In this challenge, submitted models were evaluated not only on prediction accuracy but also on model size and computational efficiency. Our MMINN model's performance was notable for achieving a compelling balance between high accuracy and a compact model size. Figure 6.2, derived from the challenge's final results, visually illustrates the model accuracy and model size ranking of the participating teams. As highlighted in the figure, teams like "Sydney" position themselves favorably, achieving high accuracy with significantly smaller model sizes compared to many other high-performing entries. This underscores the MMINN's unique strength in striking a balance between performance and deployability.

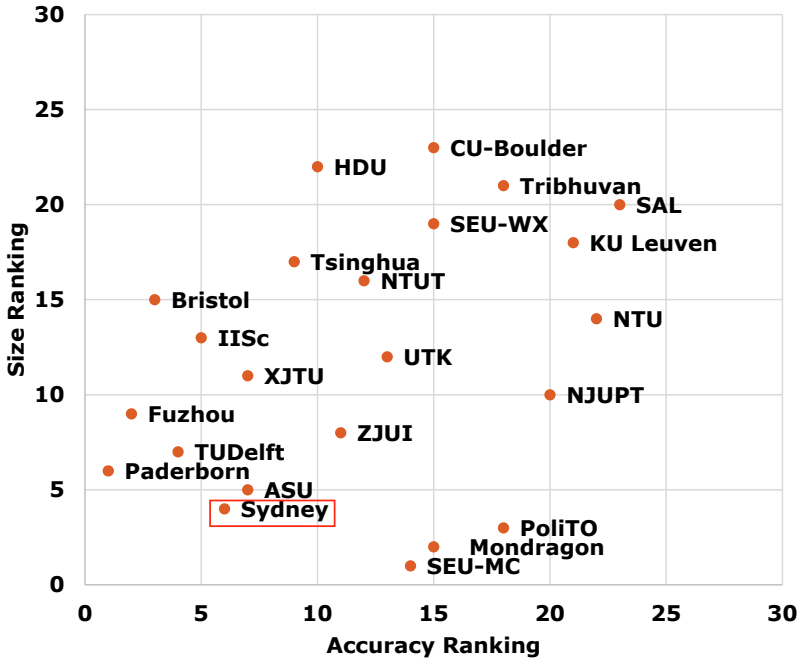

FIGURE 6.2: Model accuracy and model size ranking of the participating teams for Magnet Challenge 2023.

To facilitate broader adoption and encourage further research, the MMINN has been integrated into an open-source, web-based visualization tool called *MagNet Engine*, developed using the Streamlit framework. This platform allows users to interactively explore core loss modeling results in a user-friendly environment. The online demo is available at https://magnet-engine-app.sydney.edu.au/, and the underlying source code is openly accessible at https://github.com/moetomg/magnet-engine. The tool aims to bridge research and application by making advanced magnetic material modeling techniques easily accessible to both academic and industrial users. Figure 6.3 shows a snapshot of its intuitive interface.

- **HDPI-NN (Chapter 4):** *High-fidelity material characterization under arbitrary quasi-static excitations, including DC bias and complex harmonics.*

  Moving beyond the steady-state limitations of the MMINN, the HDPI-NN is the specialist tool for capturing intrinsic material physics. It is ideal for material science research and the design of components operating under non-standard conditions, such as low-frequency filters or transformers with significant DC-bias saturation. By

FIGURE 6.3: Screenshot of MagNet Engine web application.

integrating generalized hysteresis operators with explicit memory mechanisms, it provides the necessary material-level depth that conventional models lack, serving as the high-fidelity "physics engine" for complex transient analysis.

- **NE-DCM (Chapter 5):** *Comprehensive system-level simulation and dimensional scalability across different component dimensions.*

  As the pinnacle of this research, the NE-DCM is designed for full-scale power electronics design automation. It addresses the ultimate objective of scalability by embedding the HDPI-NN material law into a mesh-based dynamic circuit solver. This allows engineers to perform accurate time-domain simulations (Figures 6.4 and 6.5) for an entire series of magnetic components using the same material without the need for exhaustive re-characterization. It bridges the gap between microscopic magnetization behavior and macroscopic terminal characteristics, resolving the accuracy–scalability trade-off.

Furthermore, a dedicated desktop application for magnetic core modeling has been developed to support offline usage and enhanced model integration. This standalone tool is built using

FIGURE 6.4: User interface for single-cycle prediction, showing input waveform, B–H loop, and core loss results.

the Qt framework and QML for its front-end architecture, offering a robust, modular, and extensible user interface (UI). The application is designed with scalability in mind, enabling future integration of a wide range of neural and physics-based models for magnetic component simulation. At its current stage, the desktop tool primarily features the MMINN model, allowing users to carry out efficient and accurate core loss predictions under both single-cycle (see Figure 6.4) and multi-cycle (see Figure 6.5) high-frequency excitations. It supports real-time interaction, batch processing, and visual output of hysteresis loops and loss profiles, making it a practical solution for both research and industrial design workflows. The rich UI and offline capability make it particularly suitable for scenarios requiring local deployment, such as embedded system development, confidential industrial applications, or environments with limited internet connectivity.

FIGURE 6.5: User interface for multi-cycle prediction, illustrating cumulative average core loss under repeated excitations.

These different strategies collectively demonstrate the versatility and power of combining physical insights with neural networks. They show that such hybrid approaches are key to advancing magnetic component modeling, offering solutions that are not only accurate and scalable but also practical and impactful in real-world engineering contexts. The progression from mechanism-inspired exploration (the MMINN) to refined material modeling (the HDPI-NN) and finally to a comprehensive integrated paradigm (the NE-DCM) illustrates a systematic approach to tackle the multifaceted problem of core loss prediction.

6.5 Limitations of the Developed Models and Current Research

While the hybrid modeling strategies developed in this thesis (the MMINN, the HDPI-NN, and the NE-DCM) represent significant advancements in accurate, scalable, and generalizable core loss modeling, it is essential to acknowledge their current boundaries and limitations. This provides a realistic assessment of the work and sets the stage for future research directions.

- **Scope of Validation:** Although extensive experimental validation was performed across various excitation waveforms (sinusoidal, triangular, trapezoidal, harmonics, DC bias), frequencies (up to 312.5 kHz), and two primary soft magnetic materials (N87 ferrite, B35A270 silicon steel), certain extreme or niche operating conditions were not fully explored. For instance, the full range of temperatures (e.g., above 90°C or below 25°C) was not comprehensively tested across all models. More complex, highly transient waveforms with significant phase shifts beyond simple minor loops could also pose further challenges.
- **Coupled Physics and Environmental Factors:** The current NE-DCM primarily focuses on the electromagnetic behavior and its relation to core loss. While temperature is an input, the model does not fully implement a fully coupled electromagnetic-thermal simulation. Dynamic thermal effects, where core temperature changes significantly during operation due to self-heating, can influence material properties and subsequently core loss. Integrating a complete thermal model with the electromagnetic model remains a complex challenge.
- **Geometry Complexity beyond Toroidal Cores:** The scalability validation for the NE-DCM (Chapter 5) was primarily conducted on toroidal core geometries with varying dimensions. While the GDCM framework is conceptually extensible, applying the NE-DCM to highly complex core geometries (e.g., gapped cores, E-cores, or custom 3D shapes) would require a more sophisticated GDCM implementation (e.g., FEM-based GDCM) and more extensive validation, as the spatial distribution of fields becomes significantly more complex.

- **Very High-Frequency Phenomena (Resonance):** While the NE-DCM extends to high frequencies (up to 312.5 kHz), it does not explicitly model higher-order parasitic effects like winding self-capacitance or very high-frequency dimensional resonances (Section 2.1.3), which become dominant above this frequency range [107]. Extending the model's applicability into the megahertz range would require explicit incorporation of these phenomena into the physics-based solver.
- **Interpretability vs. First-Principles:** While the developed hybrid models offer improved physical interpretability compared to purely black-box neural networks, they do not provide the complete, direct physical insight of microscopic first-principles models derived entirely from fundamental physics (e.g., quantum mechanics or detailed domain dynamics simulations). The neural network components still learn complex relationships empirically, although guided by physical structures.

These limitations define the scope of the current research and highlight promising avenues for future work, which can build upon the foundational hybrid strategies developed in this thesis.

6.6 Chapter Summary

This chapter has provided a comprehensive discussion and analysis of the developed hybrid modeling strategies (the MMINN, the HDPI-NN, and the NE-DCM) and their performance. We synthesized the individual achievements of each model (Section 6.1), performed detailed comparative analyses against existing approaches (Section 6.2), and delved into the effectiveness of their underlying physics-neural network integration strategies (Section 6.3). We also discussed how the three models, through their complementary strengths, collectively contribute to the overarching thesis objective (Section 6.4) and their practical impact. Finally, the current limitations of the developed models and the scope of the research were outlined (Section 6.5).

In essence, the progression from mechanism-inspired exploration (the MMINN) to refined material modeling (the HDPI-NN) and finally to a comprehensive integrated paradigm (the NE-DCM) demonstrates a systematic and effective approach to tackle the multifaceted problem

of core loss prediction. The findings confirm that leveraging physical insights to guide neural network design is key to overcoming the inherent trade-offs in traditional core loss modeling. The developed models collectively offer solutions that are not only accurate and scalable but also practical, data-efficient, and impactful in real-world engineering contexts, setting a new benchmark for power magnetics design.

CHAPTER 7

Conclusion and Future Work

The relentless drive towards higher power density and efficiency in modern power electronics necessitates accurate, scalable, and generalizable core loss modeling. This thesis addressed the fundamental challenge inherent in this field: the long-standing trade-off between the scalability of physics-based models and the accuracy of data-driven methods. By systematically investigating hybrid physics-neural network strategies, this research has culminated in a comprehensive framework that is simultaneously accurate, scalable, and data-efficient.

7.1 Summary of the Research Journey

This thesis presented a systematic progression of research, where each stage was designed to overcome specific limitations of conventional modeling approaches:

- **Initial Exploration (MMINN):** The journey began with the Magnetization Mechanism-Inspired Neural Network, which established the proof-of-concept that physics-guided neural architectures can achieve significant data efficiency for steady-state modeling.
- **Material-Level Advance (HDPI-NN):** This led to the development of the History-Dependent Prandtl-Ishlinskii Neural Network, which conquered the challenge of material-level generality by integrating physical mechanisms of hysteresis and memory into a neural operator.
- **System-Level Synthesis (NE-DCM):** Finally, the Neural-Enhanced Dynamic Circuit Model synthesized these advancements by embedding the neural material law within a scalable physics-based solver, fully realizing the Neural-Enhanced Physics (NEP) paradigm.

7.2 Main Research and Experimental Conclusions

Through extensive experimental validation and comparative analysis, the following primary conclusions are drawn:

- **High-Fidelity Prediction under Arbitrary Conditions:** Experimental results confirm that the proposed hybrid models, particularly the NE-DCM, maintain high accuracy across a wide range of operating conditions. Specifically, the model achieves core loss prediction errors within $\pm 10\%$ even under highly non-linear, non-symmetric excitations (heavy DC bias and high-order harmonics), where traditional analytical models often fail to provide reliable results.
- **Successful Resolution of the Accuracy-Scalability Trade-off:** A definitive conclusion of this research is that the principled decomposition of the modeling task effectively resolves the conflict between accuracy and scalability. The NE-DCM demonstrated exceptional dimensional scalability, accurately predicting terminal current waveforms ($R^2 > 96\%$) and core losses for unseen core dimensions with only minimal dynamic calibration.
- **Superior Data and Memory Efficiency:** The experiments demonstrate that physics-guided architectures are significantly more efficient than pure black-box models. The developed models achieved comparable or superior accuracy while reducing the required training data and memory footprint by over 20 times compared to state-of-the-art Transformer-based or deep LSTM models.
- **Proven Portability and Extensibility:** The research confirms the robustness of the NEP paradigm across different material families. The successful cross-material validation on both TDK N87 and T65 ferrite materials proves that the methodology is a portable, generalizable blueprint for next-generation magnetic modeling.

7.3 Key Contributions

In summary, the key contributions of this thesis to the field of power electronics are formally stated as:

1. **The Proposal of the NEP Paradigm:** A novel hybrid modeling framework that resolves the fundamental accuracy-scalability trade-off through principled decomposition.

2. **The Development of the HDPI-NN Material Model:** A crucial enabling component that accurately models complex, history-dependent material behavior under arbitrary quasi-static conditions.
3. **The Establishment of a Data-Efficient Modeling Workflow:** A practical two-stage methodology (One-time Learning + Minimal Calibration) that significantly reduces the experimental burden for developing models for new components.
4. **The Creation of Open-Source Tools:** The development and release of interactive visualization tools and software to promote the practical adoption of advanced models by the broader scientific community.

7.4 Limitations and Future Work

While significant advancements have been made, the current work has certain boundaries that point towards promising avenues for future research:

- **Extended Model Applicability:**
  - **Thermal Integration:** Developing fully coupled electromagnetic-thermal models to predict core loss under dynamically changing temperatures.
  - **Very High-Frequency Phenomena:** Enhancing models to capture extremely rapid transients and resonances beyond 312.5 kHz.
  - **Geometry Complexity:** Extending scalability validation to more intricate 3D geometries, such as gapped cores or E-cores, potentially through FEM integration.
- **Broadening Material and Data Strategies:**
  - **New Material Families:** Adapting the NEP paradigm for amorphous metals, nanocrystalline materials, and powder cores.
  - **Uncertainty Quantification:** Incorporating probabilistic predictions to enhance robust design under material variations and noise.
- **Enhanced Tooling and Optimization:**

- **Full Model Integration:** Further developing the standalone desktop application to provide a unified platform for magnetic design.
- **Closed-Loop Optimization:** Integrating the models into automated frameworks that iterate through parameters to achieve optimal performance.

7.5 Closing Statement

In conclusion, by moving beyond the traditional separation of 'model-driven versus data-driven' approaches, this thesis has established a new and powerful paradigm for hybrid modeling in engineering. The Neural-Enhanced Physics framework provides not only a practical tool for power magnetics design but also a conceptual blueprint for integrating artificial intelligence with domain-specific knowledge. This work lays a robust foundation for a future where the design of high-performance power electronic systems is accelerated by intelligent, scalable, and physically-grounded modeling.

Bibliography

[1] G. V. Research, *Magnetic Materials Market Size, Share & Trends Analysis Report By Type (Hard/Permanent, Semi-hard, Soft), By Application (Automotive & Transportation, Electronics, Energy), By Region, And Segment Forecasts, 2025–2030*, 2024.

[2] C. P. Steinmetz, 'On the Law of Hysteresis,' *Transactions of the American Institute of Mining and Metallurgical Engineers*, vol. 9, no. 1, pp. 1–64, Jan. 1892.

[3] J. Reinert, A. Brockmeyer and R. W. A. A. D. Doncker, 'Calculation of Losses in Ferro- and Ferrimagnetic Materials Based on the Modified Steinmetz Equation,' *IEEE Transactions on Industry Applications*, vol. 37, no. 4, pp. 1055–1061, Jul. 2001.

[4] J. Li, T. Abdallah and C. R. Sullivan, 'Improved Calculation of Core Loss with Nonsinusoidal Waveforms,' in *Proceedings of the 2001 IEEE Industry Applications Conference (36th IAS Annual Meeting)*, Chicago, IL, USA, 2001, pp. 2203–2210.

[5] K. Venkatachalam, C. R. Sullivan, T. Abdallah and H. Tacca, 'Accurate Prediction of Ferrite Core Loss with Nonsinusoidal Waveforms Using Only Steinmetz Parameters,' in *Proceedings of the IEEE Workshop on Computers in Power Electronics (COMPEL)*, Jun. 2002, pp. 36–41.

[6] S. Yue, Q. Yang, Y. Li and C. Zhang, 'Core Loss Calculation for Magnetic Materials Employed in SMPS under Rectangular Voltage Excitations,' *AIP Advances*, vol. 8, no. 5, p. 056 121, May 2018.

[7] A. Krings and J. Soulard, 'Overview and Comparison of Iron Loss Models for Electrical Machines,' *Journal of Electrical Engineering*, vol. 10, no. 3, pp. 162–169, 2010.

[8] A. V. den Bossche, V. C. Valchev and G. B. Georgiev, 'Measurement and Loss Model of Ferrites with Non-Sinusoidal Waveforms,' in *Proceedings of the 2004 IEEE 35th Annual Power Electronics Specialists Conference (PESC)*, Aachen, Germany, 2004, pp. 4814–4818.

[9] C. R. Sullivan, J. H. Harris and E. Herbert, 'Core Loss Predictions for General PWM Waveforms from a Simplified Set of Measured Data,' in *Proceedings of the 2010 Twenty-Fifth Annual IEEE Applied Power Electronics Conference and Exposition (APEC)*, Palm Springs, CA, USA, 2010, pp. 1048–1055.

[10] J. Muhlethaler, J. Biela, J. W. Kolar and A. Ecklebe, 'Improved Core-Loss Calculation for Magnetic Components Employed in Power Electronic Systems,' *IEEE Transactions on Power Electronics*, vol. 27, no. 2, pp. 964–973, Feb. 2012.

[11] I. Mayergoyz, 'Mathematical Models of Hysteresis,' *IEEE Transactions on Magnetics*, vol. 22, no. 5, pp. 603–608, Sep. 1986.

[12] D. C. Jiles and D. L. Atherton, 'Theory of ferromagnetic hysteresis,' *Journal of Magnetism and Magnetic Materials*, vol. 61, no. 1, pp. 48–60, 1986.

[13] G. Mörée and M. Leijon, 'Review of Hysteresis Models for Magnetic Materials,' *Energies*, vol. 16, no. 9, p. 3908, 2023.

[14] T. Wang, M. Noori, W. A. Altabey *et al.*, 'From model-driven to data-driven: A review of hysteresis modeling in structural and mechanical systems,' *Mechanical Systems and Signal Processing*, vol. 204, p. 110 785, 2023.

[15] J. Brauer, 'Simple Equations for the Magnetization and Reluctivity Curves of Steel,' *IEEE Transactions on Magnetics*, vol. 11, no. 1, pp. 81–81, Jan. 1975.

[16] G. F. Dionne, J. A. Weiss and G. A. Allen, 'Hysteresis Loops Modelled from Coercivity, Anisotropy, and Microstructure Parameters,' *Journal of Applied Physics*, vol. 61, no. 8, pp. 3862–3864, Apr. 1987.

[17] J. R. Lucas and P. G. McLaren, 'B-H Loop Representation for Transient Studies,' *International Journal of Electrical Engineering Education*, vol. 28, pp. 261–270, 1991.

[18] C. E. Lin, J. B. Wei, C. L. Huang and C. J. Huang, 'A New Model for Transformer Saturation Characteristics by Including Hysteresis Loops,' *IEEE Transactions on Magnetics*, vol. 25, no. 3, pp. 2706–2712, May 1989.

[19] V. Pricop, E. Helerea and G. Scutaru, 'Fitting Magnetic Hysteresis Curves by Using Polynomials,' in *Proceedings of the 2014 International Symposium on Fundamentals of Electrical Engineering (ISFEE)*, Bucharest, Romania, 2014, pp. 1–6.

[20] M. Mirzaei, P. Ripka, J. Vyhnanek, A. Chirtsov and V. Grim, 'Modeling of Hysteresis Loops Using Rational and Power Functions,' *Journal of Magnetism and Magnetic Materials*, vol. 522, p. 167 563, 2021.

[21] S. H. Charap, 'Magnetic Hysteresis Model,' *IEEE Transactions on Magnetics*, vol. 10, no. 4, pp. 1091–1096, Dec. 1974.

[22] R. V. Lapshin, 'Analytical Model for the Approximation of Hysteresis Loop and Its Application to the Scanning Tunneling Microscope,' *Review of Scientific Instruments*, vol. 66, no. 9, pp. 4718–4730, 1995.

[23] G. Bertotti, *Hysteresis in Magnetism: For Physicists, Materials Scientists, and Engineers*. San Diego: Academic Press, 1998.

[24] D. Jiles, *Introduction to Magnetism and Magnetic Materials*, 3rd. CRC Press, 2015.

[25] B. D. Cullity and C. D. Graham, *Introduction to Magnetic Materials*, 2nd. John Wiley & Sons, 2011.

[26] D. C. Jiles and D. L. Atherton, 'Ferromagnetic hysteresis,' *IEEE Transactions on Magnetics*, vol. 19, no. 5, pp. 2183–2185, 1983.

[27] F. Preisach, 'Über die magnetische Nachwirkung,' German, *Zeitschrift für Physik*, vol. 94, pp. 277–302, 1935.

[28] L. Prandtl, 'Ein Gedankenmodell zur kinetischen Theorie der festen Körper,' *ZAMM - Zeitschrift für Angewandte Mathematik und Mechanik*, vol. 8, pp. 85–106, 1928.

[29] L. Chua and K. Stromsmoe, 'Lumped-Circuit Models for Nonlinear Inductors Exhibiting Hysteresis Loops,' *IEEE Transactions on Circuit Theory*, vol. 17, no. 4, pp. 564–574, 1970.

[30] L. Chua and S. Bass, 'A Generalized Hysteresis Model,' *IEEE Transactions on Circuit Theory*, vol. 19, no. 1, pp. 36–48, 1972.

[31] J. G. Zhu, S. Y. R. Hui and V. S. Ramsden, 'Discrete Modelling of Magnetic Cores Including Hysteresis, Eddy Current and Anomalous Losses,' *IEE Proceedings - Electric Power Applications*, vol. 140, no. 4, pp. 317–322, 1993.

[32] J. G. Zhu, S. Y. R. Hui and V. S. Ramsden, 'A Generalized Dynamic Circuit Model of Magnetic Cores for Low- and High-Frequency Applications. I. Theoretical Calculation of the Equivalent Core Loss Resistance,' *IEEE Transactions on Power Electronics*, vol. 11, no. 2, pp. 246–250, Mar. 1996.

[33] S. Y. R. Hui, J. G. Zhu and V. S. Ramsden, 'A Generalized Dynamic Circuit Model of Magnetic Cores for Low- and High-Frequency Applications. II. Circuit Model

Formulation and Implementation,' *IEEE Transactions on Power Electronics*, vol. 11, no. 2, pp. 251–259, Mar. 1996.

[34] D. Rodriguez-Sotelo, M. A. Rodriguez-Licea, I. Araujo-Vargas, J. Prado-Olivarez, A.-I. Barranco-Gutiérrez and F. J. Perez-Pinal, 'Power Losses Models for Magnetic Cores: A Review,' *Micromachines*, vol. 13, no. 3, p. 418, 2022.

[35] C. Nussbaum, H. Pfutzner, T. Booth, N. Baumgartinger, A. Ilo and M. Clabian, 'Neural Networks for the Prediction of Magnetic Transformer Core Characteristics,' *IEEE Transactions on Magnetics*, vol. 36, no. 1, pp. 313–329, Jan. 2000.

[36] D. Makaveev, L. Dupré, M. D. Wulf and J. Melkebeek, 'Dynamic Hysteresis Modelling Using Feed-Forward Neural Networks,' *Journal of Magnetism and Magnetic Materials*, vol. 254–255, pp. 256–258, 2003.

[37] I. Kucuk and N. Derebasi, 'Prediction of Power Losses in Transformer Cores Using Feed Forward Neural Network and Genetic Algorithm,' *Measurement*, vol. 39, no. 7, pp. 605–611, 2006.

[38] J. Deng, W. Wang, Z. Ning *et al.*, 'High-frequency Core Loss Modeling Based on Knowledge-Aware Artificial Neural Network,' *IEEE Transactions on Power Electronics*, vol. 39, no. 2, pp. 1968–1973, 2023.

[39] S. Kül, B. Yildiz, B. Tamyurek and I. Iskender, 'Coreloss Estimation via Long Short-Term Memory Model (LSTM) of Dry-Type Transformer based on FEA,' in *2021 10th International Conference on Renewable Energy Research and Applications (ICRERA)*, Istanbul, Turkey, 2021, pp. 357–361.

[40] H. Li, D. Serrano, S. Wang and M. Chen, 'MagNet-AI: Neural Network as Datasheet for Magnetics Modeling and Material Recommendation,' *IEEE Transactions on Power Electronics*, vol. 38, no. 12, pp. 15 854–15 869, Dec. 2023.

[41] H. Li, D. Serrano, S. Wang and M. Chen, 'How MagNet: Machine Learning Framework for Modeling Power Magnetic Material Characteristics,' *IEEE Transactions on Power Electronics*, vol. 38, no. 12, pp. 15 829–15 853, Dec. 2023.

[42] X. Liu, M. Wei, M. Qiu *et al.*, 'Convolutional Neural Network (CNN) Based Planar Inductor Evaluation and Optimization,' in *2022 IEEE Applied Power Electronics Conference and Exposition (APEC)*, Mar. 2022, pp. 1506–1511.

[43] W. Kirchgässner, N. Förster, T. Piepenbrock, O. Schweins and O. Wallscheid, 'HARD-CORE: H-Field and Power Loss Estimation for Arbitrary Waveforms With Residual, Dilated Convolutional Neural Networks in Ferrite Cores,' *IEEE Transactions on Power Electronics*, vol. 40, no. 2, pp. 3326–3335, Feb. 2025.

[44] A. Chandra, B. Daniels, M. Curti, K. Tiels and E. A. Lomonova, 'Magnetic hysteresis modeling with neural operators,' *IEEE Transactions on Magnetics*, 2024.

[45] D. Serrano, H. Li, S. Wang *et al.*, 'Why MagNet: Quantifying the Complexity of Modeling Power Magnetic Material Characteristics,' *IEEE Transactions on Power Electronics*, vol. 38, no. 11, pp. 14 292–14 316, 2023.

[46] G. Bertotti, 'Physical interpretation of eddy current losses in ferromagnetic materials. I. Theoretical considerations,' *Journal of Applied Physics*, vol. 57, no. 6, pp. 2110–2117, Mar. 1985.

[47] G. Bertotti, 'General properties of power losses in soft ferromagnetic materials,' *IEEE Transactions on Magnetics*, vol. 24, no. 1, pp. 621–630, 1988.

[48] C. D. Graham, 'Physical origin of losses in conducting ferromagnetic materials (invited),' *Journal of Applied Physics*, vol. 53, no. 11, pp. 8276–8280, Nov. 1982.

[49] P. Weiss, 'La variation du ferromagnétisme avec la température,' *Comptes Rendus*, vol. 143, pp. 1136–1139, 1906.

[50] P. Weiss, 'L'hypothèse du champ moléculaire et la propriété ferromagnétique,' *Journal de Physique*, vol. 6, pp. 667–690, 1907.

[51] H. J. Williams, R. M. Bozorth and W. Shockley, 'Magnetic Domain Patterns on Single Crystals of Silicon Iron,' *Physical Review*, vol. 75, no. 1, pp. 155–178, Jan. 1949.

[52] H. Barkhausen, 'Zwei mit Hilfe der neuen Verstärker entdeckte Erscheinungen,' *Physikalische Zeitschrift*, vol. 20, pp. 401–403, 1919.

[53] J. L. Snoek, 'Dispersion and absorption in magnetic ferrites at frequencies above one Mc/s,' *Physica*, vol. 14, pp. 207–217, 1948.

[54] H. Suhl, 'Theory of the magnetic damping constant,' *IEEE Transactions on Magnetics*, vol. 34, no. 4, pp. 1834–1838, 2002.

[55] C. Kittel, *Introduction to Solid State Physics*, 8th. John Wiley & Sons, 2005.

[56] R. W. Erickson and D. Maksimović, *Fundamentals of Power Electronics*, 3rd. Berlin/Heidelberg, Germany: Springer International Publishing, 2020.

[57] I. D. Mayergoyz, 'The Classical Preisach Model of Hysteresis,' in *Mathematical Models of Hysteresis*, Academic Press, 1991, pp. 1–63.

[58] D. C. Hughes and J. T. Wen, 'Preisach Modeling and Compensation for Smart Material Hysteresis,' in *Proceedings of SPIE: Active Materials and Smart Structures*, vol. 2427, SPIE, Feb. 1995, pp. 50–64.

[59] G. Kádár, 'On the Product Preisach Model of Hysteresis,' *Physica B: Condensed Matter*, vol. 275, no. 1–3, pp. 40–44, 2000.

[60] E. Kokornaczyk and M. W. Gutowski, 'Anhysteretic Functions for the Jiles–Atherton Model,' *IEEE Transactions on Magnetics*, vol. 51, no. 2, pp. 1–5, 2015.

[61] J. V. Leite, A. Benabou and N. Sadowski, 'Accurate Minor Loops Calculation with a Modified Jiles-Atherton Hysteresis Model,' *COMPEL - The International Journal for Computation and Mathematics in Electrical and Electronic Engineering*, vol. 28, no. 3, pp. 741–749, 2009.

[62] P. R. Wilson, J. N. Ross and A. D. Brown, 'Simulation of Magnetic Component Models in Electric Circuits Including Dynamic Thermal Effects,' *IEEE Transactions on Power Electronics*, vol. 17, no. 1, pp. 55–65, Jan. 2002.

[63] Z. Szabó, I. Tugyi, G. Kádár and J. Füzi, 'Identification Procedures for Scalar Preisach Model,' *Physica B: Condensed Matter*, vol. 343, no. 1–4, pp. 142–147, 2004.

[64] S. Hussain and D. A. Lowther, 'An Efficient Implementation of the Classical Preisach Model,' *IEEE Transactions on Magnetics*, vol. 54, no. 3, pp. 1–4, 2017.

[65] I. D. Mayergoyz, *Mathematical Models of Hysteresis and Their Applications*. Academic Press, 2003.

[66] G. Mörée and M. Leijon, 'Review of Play and Preisach Models for Hysteresis in Magnetic Materials,' *Materials*, vol. 16, no. 6, p. 2422, 2023.

[67] S. Bobbio, G. Milano, C. Serpico and C. Visone, 'Models of Magnetic Hysteresis Based on Play and Stop Hysterons,' *IEEE Transactions on Magnetics*, vol. 33, no. 6, pp. 4417–4426, 2002.

[68] H. Y. Lu, J. G. Zhu, S. Y. R. Hui and V. S. Ramsden, 'A Generalized Dynamic Transformer Circuit Model Including All Types of Core Losses,' in *Proceedings of the 1998 International Conference on Power Electronic Drives and Energy Systems for Industrial Growth*, vol. 2, IEEE, Dec. 1998, pp. 978–983.

[69] A. V. Radun, 'Development of Dynamic Magnetic Circuit Models Including Iron Saturation and Losses,' *IEEE Transactions on Magnetics*, vol. 50, no. 5, pp. 1–10, May 2014, Art. no. 7027010.

[70] M. Chen, M. Araghchini, K. K. Afridi, J. H. Lang, C. R. Sullivan and D. J. Perreault, 'A Systematic Approach to Modeling Impedances and Current Distribution in Planar Magnetics,' *IEEE Transactions on Power Electronics*, vol. 31, no. 1, pp. 560–580, Jan. 2015.

[71] X. Shen, Y. Zuo, J. Kong and W. Martinez, 'Artificial Intelligence Applications in High-Frequency Magnetic Components Design for Power Electronics Systems: An Overview,' *IEEE Transactions on Power Electronics*, vol. 39, no. 7, pp. 8478–8496, Jul. 2024.

[72] M. Chen *et al.*, 'MagNet Challenge for Data-Driven Power Magnetics Modeling,' *IEEE Open Journal of Power Electronics*, vol. 6, pp. 883–898, 2025.

[73] E. Dogariu, H. Li, D. S. López, S. Wang, M. Luo and M. Chen, 'Transfer Learning Methods for Magnetic Core Loss Modeling,' in *Proceedings of the 2021 IEEE 22nd Workshop on Control and Modelling of Power Electronics (COMPEL)*, IEEE, Nov. 2021, pp. 1–6.

[74] Y. Xu, S. Kohtz, J. Boakye, P. Gardoni and P. Wang, 'Physics-Informed Machine Learning for Reliability and Systems Safety Applications: State of the Art and Challenges,' *Reliability Engineering & System Safety*, vol. 230, p. 108 900, 2023.

[75] M. Raissi, P. Perdikaris and G. E. Karniadakis, 'Physics-Informed Neural Networks: A Deep Learning Framework for Solving Forward and Inverse Problems Involving Nonlinear Partial Differential Equations,' *Journal of Computational Physics*, vol. 378, pp. 686–707, 2019.

[76] J. Lim and D. Psaltis, 'MaxwellNet: Physics-Driven Deep Neural Network Training Based on Maxwell's Equations,' *APL Photonics*, vol. 7, no. 1, p. 011 301, Jan. 2022.

[77] A. Kovacs, L. Exl, A. Kornell *et al.*, 'Magnetostatics and Micromagnetics with Physics Informed Neural Networks,' *Journal of Magnetism and Magnetic Materials*, vol. 548, p. 168 951, 2022.

[78] Y. Yao *et al.*, 'PINN Based Data Driven Magnetics Loss Modeling,' in *Proceedings of the 2024 IEEE 10th International Power Electronics and Motion Control Conference (IPEMC-ECCE Asia)*, Chengdu, China, 2024, pp. 3505–3510.

[79] N. Rajput, H. B. Sandhibigraha, N. Agrawal and V. M. Iyer, 'An Empirical Model Informed Neural Network Core Loss Predictor for Soft Magnetic Materials,' *IEEE Transactions on Power Electronics*, vol. 40, no. 8, pp. 11 257–11 267, Aug. 2025.

[80] A. Salvini and F. R. Fulginei, 'Genetic algorithms and neural networks generalizing the Jiles-Atherton model of static hysteresis for dynamic loops,' *IEEE Transactions on Magnetics*, vol. 38, no. 2, pp. 873–876, Mar. 2002.

[81] A. A. Adly and S. K. Abd-El-Hafiz, 'Using neural networks in the identification of Preisach-type hysteresis models,' *IEEE Transactions on Magnetics*, vol. 34, no. 3, pp. 629–635, 2002.

[82] Y. Li, J. Zhu, Y. Li and L. Zhu, 'A hybrid Jiles–Atherton and Preisach model of dynamic magnetic hysteresis based on backpropagation neural networks,' *Journal of Magnetism and Magnetic Materials*, vol. 544, p. 168 655, 2022.

[83] C. Grech, M. Buzio, M. Pentella and N. Sammut, 'Dynamic Ferromagnetic Hysteresis Modelling Using a Preisach-Recurrent Neural Network Model,' *Materials*, vol. 13, no. 11, p. 2561, 2020.

[84] G. Chen, G. Chen and Y. Lou, 'Diagonal Recurrent Neural Network-Based Hysteresis Modeling,' *IEEE Transactions on Neural Networks and Learning Systems*, vol. 33, no. 12, pp. 7502–7512, Dec. 2022.

[85] H. Zhang, Q. Yang, C. Zhang, Y. Li and Y. Chen, 'Magnetic Properties Simulation of Electrical Steel Sheet Based on Recurrent Neural Network,' *IEEE Transactions on Magnetics*, vol. 60, no. 3, pp. 1–4, Mar. 2024, Art no. 7300304.

[86] W. Bradley, J. Kim, Z. Kilwein *et al.*, 'Perspectives on the integration between first-principles and data-driven modeling,' *Computers & Chemical Engineering*, vol. 166, p. 107 898, 2022.

[87] S. Licciardi, G. Ala, E. Francomano *et al.*, 'Neural Network Architectures and Magnetic Hysteresis: Overview and Comparisons,' *Mathematics*, vol. 12, no. 21, p. 3363, 2024.

[88] Q. Huang, Y. Li, J. Zhu and S. Li, 'Magnetization Mechanism-Inspired Neural Networks for Core Loss Estimation,' *IEEE Transactions on Power Electronics*, vol. 39, no. 12, pp. 16 382–16 390, 2024.

[89] Q. Huang, S. Li, Y. Li and J. Zhu, 'Magnetization Mechanism-Inspired Neural Network for Core Loss Estimation,' in *Proceedings of the 2024 IEEE Energy Conversion Congress and Exposition (ECCE)*, Phoenix, AZ, USA, 2024, pp. 7137–7144.

[90] K. Krikelis, K. van Berkel and M. Schoukens, 'Artificial Neural Network Hysteresis Operators for the Identification of Hammerstein Hysteretic Systems,' *IFAC-PapersOnLine*, vol. 54, no. 7, pp. 702–707, 2021.

[91] F. D. Tan, J. L. Vollin and S. M. Cuk, 'A Practical Approach for Magnetic Core-Loss Characterization,' *IEEE Transactions on Power Electronics*, vol. 10, no. 2, pp. 124–130, Mar. 1995.

[92] M. Mu, Q. Li, D. J. Gilham, F. C. Lee and K. D. Ngo, 'New Core Loss Measurement Method for High-Frequency Magnetic Materials,' *IEEE Transactions on Power Electronics*, vol. 29, no. 8, pp. 4374–4381, Aug. 2013.

[93] S. Wang, Y. Li, M. Chen, T. Guillod, T. Wu and H. Li, 'A Simplified Dc-Bias Injection Method with Mirror Transformer for Magnetic Material Characterization,' in *Proceedings of the IEEE Applied Power Electronics Conference and Exposition (APEC)*, Orlando, FL, USA, 2023, pp. 1565–1571.

[94] R. Delbourgo and J. A. Gregory, 'Shape Preserving Piecewise Rational Interpolation,' *SIAM Journal on Scientific and Statistical Computing*, vol. 6, no. 4, pp. 967–976, 1985.

[95] S. Liu, E. Johns and A. J. Davison, 'End-To-End Multi-Task Learning With Attention,' in *2019 IEEE/CVF Conference on Computer Vision and Pattern Recognition (CVPR)*, Long Beach, CA, USA, 2019, pp. 1871–1880.

[96] D. P. Kingma and J. Ba, *Adam: A Method for Stochastic Optimization*, arXiv preprint arXiv:1412.6980, 2014.

[97] L. Prechelt, 'Early Stopping—But When?' In *Neural Networks: Tricks of the Trade*, Berlin, Heidelberg: Springer Berlin Heidelberg, 2002, pp. 55–69.

[98] N. Rasekh, J. Wang and X. Yuan, 'Artificial Neural Network Aided Loss Maps for Inductors and Transformers,' *IEEE Open Journal of Power Electronics*, vol. 3, pp. 886–898, 2022.

[99] Q. Huang, Y. Li, Y. Dou, Y. Li, J. Zhu and S. Li, 'History-Dependent Prandtl–Ishlinskii Neural Network for Quasi-Static Core Loss Prediction Under Arbitrary Excitation Waveforms,' *IEEE Transactions on Power Electronics*, vol. 40, no. 7, pp. 9625–9637, 2025.

[100] P. Pruksanubal, A. Binner and K. H. Gonschorek, 'Determination of Distribution Functions and Parameters for the Preisach Hysteresis Model,' in *Proceedings of the 17th International Zurich Symposium on Electromagnetic Compatibility*, Singapore, 2006, pp. 258–261.

[101] Y. Li and Z. Luo, 'A Comparative Study of J–A and Preisach Improved Models for Core Loss Calculation under DC Bias,' *Scientific Reports*, vol. 14, no. 1, p. 9409, 2024.

[102] S. Wang, H. Li, D. Serrano *et al.*, 'A Simplified DC-Bias Injection Method for Characterizing Power Magnetics Using a Voltage Mirror Transformer,' *IEEE Transactions on Power Electronics*, vol. 39, no. 6, pp. 6608–6612, 2024.

[103] J. C. Maxwell, 'VIII. A Dynamical Theory of the Electromagnetic Field,' *Philosophical Transactions of the Royal Society of London*, no. 155, pp. 459–512, 1865.

[104] J. Smith, 'Advanced modeling of magnetic hysteresis in electrical machines,' Ph.D. dissertation, Massachusetts Institute of Technology, Cambridge, MA, USA, 2020.

[105] P. Pejovic and D. Maksimovic, 'A method for fast time-domain simulation of networks with switches,' *IEEE Transactions on Power Electronics*, vol. 9, no. 4, pp. 449–456, 1994.

[106] H. Pfutzner, P. Schonhuber, B. Erbil, G. Harasko and T. Klinger, 'Problems of loss separation for crystalline and consolidated amorphous soft magnetic materials,' *IEEE transactions on magnetics*, vol. 27, no. 3, pp. 3426–3432, 2002.

[107] S. Lin, T. Brinker, L. Fauth and J. Friebe, 'Review of dimensional resonance effect for high frequency magnetic components,' in *Proc. 21st European Conf. Power Electronics and Applications (EPE'19 ECCE Europe)*, 2019, P–1.

[108] T. Akiba, S. Sano, T. Yanase, T. Ohta and M. Koyama, 'Optuna: A next-generation hyperparameter optimization framework,' in *Proceedings of the 25th ACM SIGKDD international conference on knowledge discovery & data mining*, 2019, pp. 2623–2631.